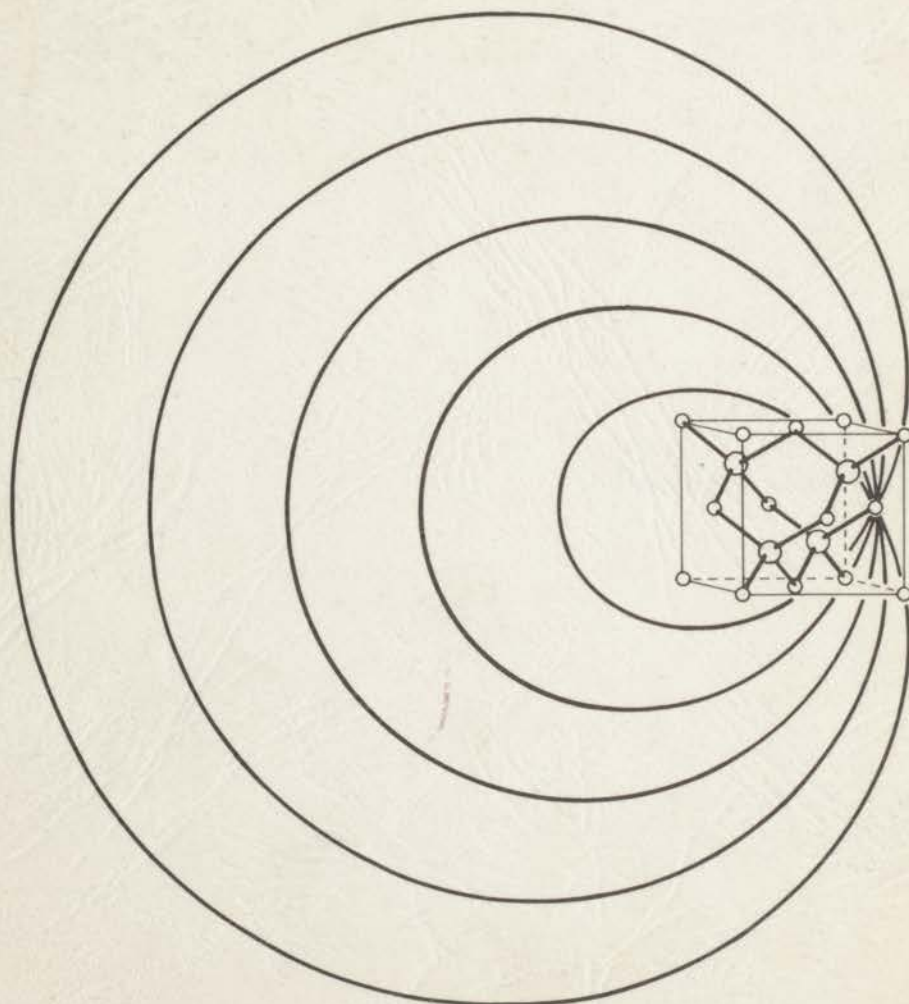


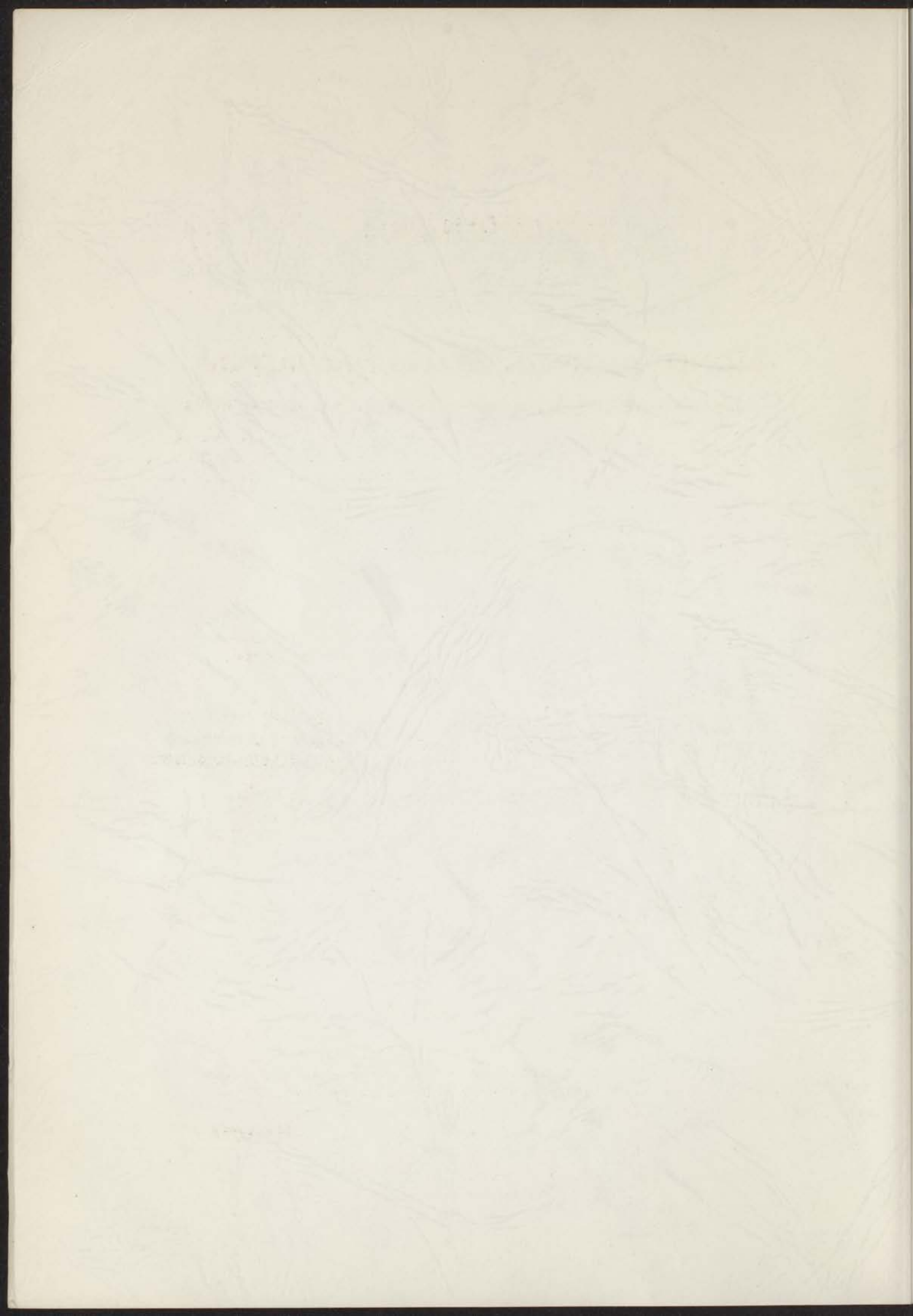
INSTITUUT-LORENTZ  
voor theoretische natuurkunde  
Nieuwsteeg 18-Leiden-Nederland

12 NOV 1970

LATTICE DYNAMICS  
OF  
MAGNESIUM STANNIDE AND ZINC BLENDE  
An experimental study by means of inelastic neutron scattering



J. BERGSMA



12 NOV. 1970

**LATTICE DYNAMICS**  
**OF**  
**MAGNESIUM STANNIDE AND ZINC BLENDE**  
An experimental study by means of inelastic neutron scattering

**INSTITUUT-LORENTZ**  
voor theoretische natuurkunde  
Nieuwsteeg 18-Leiden-Nederland

J. BERGSMA

kast dissertaties

LATTICE DYNAMICS

OF

MAGNESIUM STANNIDE AND ZINC BLENDE

An experimental study by means of inelastic neutron scattering

Author's name  
and address

AMSTERDAM

North-Holland

## STELLINGEN

### I

Zowel Rajagopal en Srinivasan als Banerjee en Varshni stellen ten onrechte dat de koppelingscoëfficiënten, door Smith gebruikt in de beschrijving van de kristaldynamica van diamant, onjuist zijn geformuleerd.

*H.M.J. Smith, Phil. Trans. Roy. Soc. London, A241 (1948), 105.*

*A.K. Rajagopal, R. Srinivasan, Z. Physik 158 (1960), 471.*

*R. Banerjee, Y.P. Varshni, Can. J. Phys. 47 (1969), 451.*

### II

Bij de interpretatie van infrarood- en Raman spectra van vaste stoffen verdient het aanbeveling, waar mogelijk, de resultaten van inelastische neutronenstrooiing in rekening te brengen.

*S.A. Solin, A.K. Ramdas, Phys. Rev. B1 (1970), 1687.*

*Dit proefschrift, hoofdstuk VII.*

*W.G. Nilsen, Phys. Rev. 182 (1969), 838.*

### III

Voor de bepaling van dispersierelaties in éénkristallen door middel van inelastische neutronenstrooiing kan de inverse beryllium-filter methode van groot belang zijn.

*Dit proefschrift, hoofdstuk V en VII.*

### IV

De aanname dat de spins in antiferromagnetisch CoO op één Bravais-rooster liggen, leidt tot een colineaire spinstructuur. Uit symmetriebeschouwingen volgt dat deze aanname geheel in overeenstemming is met de waargenomen monokliene deformatie van het rooster beneden de Néel temperatuur.

*B. van Laar, Phys. Rev. 138A (1965), 584.*

*S. Saito, K. Nakahigashi en Y. Shimomura,*

*J. Phys. Soc. Japan 21 (1966), 850.*

*J.H. Greiner, A.E. Berkowitz en J.E. Weidenborner,*

*J. Appl. Phys. 37 (1966), 2149.*

### V

Nog te weinig wordt ingezien dat de spectroscopie van gammastraling ontstaan bij vangst van thermische neutronen van veel belang kan zijn voor het ontwerpen van kernreactoren.

## VI

Het verschil tussen de frequenties van de gelocaliseerde vibraties in de  $\alpha$ - en  $\beta$ -fasen van palladiumhydride is slechts te verklaren met behulp van een correlatie tussen de protonen, welke afhangt van de waterstofconcentratie.

- A.J. Maeland, *Can. J. Phys.* 46 (1968), 121.  
K. Sköld, G. Nelin, *J. Phys. Chem. Solids* 28 (1967), 2369.  
J. Bergsma, J.A. Goedkoop, *Physica* 26 (1960), 744.  
W. Kley, J. Peretti, R. Rubin, G. Verdan, *Inelastic Scattering of Neutrons by Condensed Systems, Proc. Symp. Brookhaven* (1965), BNL 940 (C-45), 105.

## VII

Door MacCallum en Tanner worden bezwaren aangevoerd tegen de gangbare formulering voor de bepaling van reactie-kinetische grootheden volgens de thermogravimetrische methode. Deze zijn onjuist gefundeerd.

- W.W. Wendtlandt, *Thermal Methods of Analysis, Interscience Publishers, New York* (1964),  
C. Keattch, *Introduction of Thermogravimetry, Heyden and Sadtler* (1969).  
J.R. MacCallum, J. Tanner, *Nature* 225 (1970), 1127.

## VIII

Het valt te betreuren dat voor het implementeren van Algol als programmeertaal de standaardisatie van de in- en uitvoerfaciliteiten niet is doorgevoerd tegelijkertijd met het definiëren van de referentietaal.

## IX

De in het Voortgangsadvies 1970 van de Raad van Advies voor het Wetenschapsbeleid geformuleerde opvattingen ten aanzien van kern-energetisch onderzoek in nationaal en internationaal verband zijn in strijd met de daarin gegeven aanbeveling.

## X

In de zorg voor geestelijk gehandicapten dient meer dan tot nu toe rekening te worden gehouden met de normen en gevoelens ten aanzien van de verschillende leefmilieu's, welke zij vanuit hún identiteit inbrengen.

LATTICE DYNAMICS  
OF  
MAGNESIUM STANNIDE AND ZINC BLENDE

An experimental study by means of inelastic neutron scattering

PROEFSCHRIFT

TER VERKRIJGING VAN DE GRAAD VAN DOCTOR IN  
DE WISKUNDE EN NATUURWETENSCHAPPEN AAN  
DE RIJKSUNIVERSITEIT TE LEIDEN, OP GEZAG VAN  
DE RECTOR MAGNIFICUS DR. C. SOETEMAN,  
HOGLERAAR IN DE FACULTEIT DER LETTEREN,  
TEN OVERSTAAN VAN EEN COMMISSIE UIT DE SENAAT  
TE VERDEDIGEN OP WOENSDAG 14 OKTOBER 1970  
TE KLOKKE 14.15 UUR

DOOR

JITZE BERGSMA

GEBOREN TE WIJMBRITSERADEEL IN 1932

PROMOTOR: Prof. dr J.A. GOEDKOOP

Aan de nagedachtenis van mijn ouders

Aan Willy

## VOORWOORD

Het in dit proefschrift beschreven onderzoek is tot stand gekomen dankzij de medewerking welke ik van vele zijden heb mogen ontvangen en waarvoor ik mijn erkentelijkheid uitspreek.

Gedurende het gehele onderzoek heb ik veel steun en stimulerende belangstelling ondervonden van dr B.O. Loopstra. Ik ben hem veel dank verschuldigd voor de waardevolle wijze waarop hij tot het welslagen van het werk heeft bijgedragen.

Veel heb ik te danken aan de plezierige samenwerking en de vruchtbare discussies met drs C. van Dijk. De voortdurende uitwisseling van gedachten zijn voor mij van essentieel belang geweest.

De heer G.C.J. van den Bogaard heeft door zijn technische assistentie en de medewerking bij het schrijven van rekenprogramma's een gewaardeerde bijdrage geleverd.

Het ontwerp van de drie-kristalspectrometer is van de heer S. Slagter. De bouw en het onderhoud van de elektronische apparatuur werden verzorgd door de heren Th.H. Terwisscha van Scheltinga en A.Th.J.M. Overtoom. Ik ben hen allen zeer erkentelijk.

De medewerking van de reactorbedrijfsgroep is zeer belangrijk geweest voor de uitvoering van de experimenten.

Le cristal de blende a été mis à ma disposition gentiment par les Houillères du Bassin du Duphiné, Le Villaret de Susville, Isère, France. J'exprime à Monsieur Haudour ma gratitude pour son obligeance à cet effet et je remercie Messieurs Schweizer et Van Laar de leur intermédiaire pour réaliser le prêt.

De directie van het Reactor Centrum Nederland dank ik voor de mogelijkheid de tekst van dit werk tegelijkertijd als proefschrift en als extern rapport te laten verschijnen.

Ik dank mevrouw E.A.M. Endel-Kramer en mejuffrouw G.E. Möls voor de verzorging van het typewerk en de RCN reprografische dienst voor de uitvoering.

Voor de steun en stimulans, welke ik te allen tijde van mijn vrouw heb ontvangen, ben ik haar meer dan dankbaar.

## C O N T E N T S

	<u>page</u>
Chapter I INTRODUCTION	
References	4
Chapter II GENERAL HARMONIC THEORY OF LATTICE DYNAMICS	
2.1. Born-Von Karman formalism	5
2.2. Long-wavelength method	10
2.3. Group-theoretical treatment of the dynamical matrix	12
References	18
Chapter III LATTICE DYNAMICS OF IONIC AND COVALENT CRYSTALS	
3.1. Rigid ion model	19
3.2. Shell model	25
References	27
Chapter IV THEORY OF NEUTRON SCATTERING	
4.1. Introduction	28
4.2. Scattering cross section	31
References	37
Chapter V EXPERIMENTAL	
5.1. Introduction	38
5.2. Description of the spectrometer	38
5.3. Experimental methods	43
5.4. Resolution and focusing	46
5.5. Inverse beryllium-filter method	56
References	61
Chapter VI MAGNESIUM STANNIDE	
6.1. Introduction	62
6.2. Lattice dynamics	63
6.2.1. Short-range force constants and coupling coefficients	63
6.2.2. Group theory	65
6.2.3. Elastic constants and optic frequencies	74
6.3. Results and analysis	77
6.4. Discussion	85
References	89

	<u>page</u>
Chapter VII ZINC BLENDE	
7.1. Introduction	90
7.2. Lattice dynamics	91
7.2.1. Short-range force constants and coupling coefficients	91
7.2.2. Group theory	92
7.2.3. Elastic constants and optic frequencies	98
7.3. Results and analysis	100
7.4. Discussion	106
References	111
Chapter VIII CONCLUDING REMARKS	
References	114
APPENDIX	115
SUMMARY	116
SAMENVATTING	118

## Chapter I

### INTRODUCTION

Lattice vibrations are the collective motions of atoms in a solid oscillating about their equilibrium positions. The characteristics of these motions are mainly determined by the interatomic forces, *i.e.*, by the potential between the atoms composing a crystal. Therefore, the analysis of the lattice vibrations is important in investigations on interatomic potentials.

Quantum-mechanically the elementary excitations associated with the vibration of a crystal lattice are called phonons. The relation between the frequency and the wave vector of a normal vibration is generally known as the dispersion relation. In the study of lattice dynamics this dispersion relation is of fundamental interest for mainly two reasons. Firstly, it leads to a better insight in a number of physical phenomena of solids as thermal properties and electron transport properties and, secondly, the dispersion relation provides the experimental information required to compare with theoretical model calculations. It is particularly in this last context that the dispersion relation will play a major role in this investigation.

Lattice-dynamical investigations have gained increasing interest over the past ten years, in particular because of the development of the method of inelastic scattering of thermal neutrons. Before this method became available only integral quantities as specific heat and elastic constants or data from infra-red absorption, Raman scattering and diffuse X-ray scattering could provide some information on the dynamical behaviour of atoms in solids. In most cases this information concerned frequencies of vibrations of very long wavelengths. However, because of the characteristic relation between the energy and momentum of the neutron, the scattering of neutrons allows an experimental determination of the dispersion relation all through the Brillouin zone of a crystal. It is this specific and more complete information which provides a deeper understanding of many properties of condensed matter than was obtainable by the more conventional methods.

With this technique of inelastic neutron scattering (INS) available it seemed of interest to apply it in an investigation on crystalline

materials of which the degree of ionicity or covalency of its bonding is still uncertain and in which phonons may play a role in indirect electronic transitions. For this purpose magnesium stannide  $Mg_2Sn$  and zinc blende  $ZnS$  have been chosen as for these compounds sufficiently large single crystals could be obtained. Both crystals have a mixed bonding where the interatomic bonds are partly ionic and partly covalent.

Magnesium stannide is a semiconductor of the II-IV group and it crystallizes according to the antiferroite structure. It is closely related to the magnesium compounds of germanium and silicon which are semiconductors also. The elastic constants indicate a resemblance to covalently bonded semiconductors, but infra-red reflection measurements and the high- and low-frequency dielectric constants show evidence for ionic bonding. From velocity of sound data and long-wavelength optic frequencies Davis, Whitten and Danielson<sup>1)</sup> calculated dispersion relations in the main symmetry directions. From band theory calculations it has been found that phonons in the  $[001]$ -direction are involved in indirect electronic transitions. The investigation of the lattice dynamics of magnesium stannide and the knowledge of its dispersion relation are important for both the study of the bonding character and the interpretation of the semiconducting properties.

Zinc blende is the cubic phase of zinc sulphide. Lattice-dynamical calculations on a number of zinc blende structure crystals were carried out by Kaplan and Sullivan<sup>2)</sup>. They found that the parameters in their calculations could not be uniquely determined by fitting the calculations to the available data on elastic constants and long-wavelength optic frequencies. Recently Feldkamp *et al.*<sup>3)</sup> measured the acoustic branches of zinc blende and Vetelino *et al.*<sup>4)</sup> compared these data to a rigid ion model but this could not represent the results very satisfactorily.

It is the aim of this work to study the dynamics of these two crystals by determining the dispersion relation by inelastic neutron scattering using a triple-axis crystal spectrometer. The experimental results will be compared with calculations applying the rigid ion model and the shell model. In the first model only short-range repulsive and

electrostatic forces are taken into account whereas the shell model also accounts for polarization of the ions. Although this shell model has been successful for alkali halides and diamond type lattices its applicability for zinc blende structures has been questioned<sup>5,6)</sup>. Only a few zinc blende type compounds have been studied by means of neutron scattering so far.

The general theory of lattice dynamics is formulated in chapter II. The lattice-dynamical calculations are carried out according to the scheme given by Born and Von Karman<sup>7)</sup>. To simplify these calculations the symmetry properties of the crystal lattice can be taken advantage of through the use of group-theoretical techniques. A brief outline of this method will be given. In chapter III the dynamical models are discussed and calculations of the lattice sums for the Coulomb interactions are carried out. The characteristics of the neutron radiation and the theory of neutron scattering are briefly reviewed in chapter IV. A description of the instrument, methods of operation and further experimental details are given in chapter V. The results of the measurements and calculations on the two crystals are presented in the chapters VI and VII. In chapter VIII the merits and limitations of the dynamical models applied for the crystals in this investigation are discussed.

References

- 1) L.C. Davis, W.B. Whitten, G.C. Danielson, J. Phys. Chem. Solids, 28 (1967), 439.
- 2) H. Kaplan, J.J. Sullivan, Phys. Rev. 130 (1963), 120.
- 3) L.A. Feldkamp, G. Venkataraman, J.S. King, Sol. State Comm. 7 (1969), 1571.
- 4) J.F. Vetelino, S.S. Mitra, O. Brafman, T.C. Damen, Sol. State Comm. 7 (1969), 1809.
- 5) W. Cochran, Lattice Dynamics, Proc. Conf. Copenhagen, 1963, Ed. R.F. Wallis, Pergamon Press, London (1965), 75.
- 6) B.G. Dick, Lattice Dynamics, Proc. Conf. Copenhagen, 1963, Ed. R.F. Wallis, Pergamon Press, London (1965), 159.
- 7) M. Born, K. Huang, Dynamical Theory of Crystal Lattices, Oxford University Press, 1956.

Chapter II

GENERAL HARMONIC THEORY OF LATTICE DYNAMICS

2.1. Born-Von Karman formalism

Most lattice-dynamical calculations are carried out according to a scheme given by Born and Von Karman which is presented in great detail in textbooks and review articles<sup>1,2)</sup>. The theory is based on three general assumptions which are applied over a wide field of solid state physics: 1) the assumption of cyclic boundary conditions, 2) the adiabatic or Born-Oppenheimer approximation, 3) the harmonic approximation.

Cyclic Boundary Conditions In considering wave propagation through a lattice it is attractive to ignore surface effects. The assumption of an infinitely large crystal is unrealistic and leads to an infinite number of atoms and consequently to an infinite number of vibrational modes and a divergent crystal energy. In order to reach a proper normalization of the number of modes and of the crystal energy and yet neglecting surface effects, the infinite crystal is divided in macrocrystals each containing  $L_1 \times L_2 \times L_3$  unit cells. The cyclic boundary condition now requires that equivalent atoms on opposite faces of such a macrocrystal move in exactly the same way and that therefore the atomic displacements are periodic with the dimensions of the macrocrystal.  $\underline{u}(1+L, \kappa) = \underline{u}(1, \kappa)$  where 1 specifies a particular unit cell in the crystal and  $\kappa$  an atom in the unit cell;  $\underline{u}$  is the displacement vector. If  $\underline{q}$  is the propagation vector of a certain wave, the cyclic boundary condition requires that

$$e^{i\underline{q} \cdot L_1 \underline{a}_1} = e^{i\underline{q} \cdot L_2 \underline{a}_2} = e^{i\underline{q} \cdot L_3 \underline{a}_3} = 1 .$$

Here  $\underline{a}_1$ ,  $\underline{a}_2$  and  $\underline{a}_3$  are the primitive translational vectors of the lattice. From this it can be seen that only  $\underline{q}$  vectors given by

$$\underline{q} = 2\pi \left\{ \frac{h_1}{L_1} \underline{b}_1 + \frac{h_2}{L_2} \underline{b}_2 + \frac{h_3}{L_3} \underline{b}_3 \right\}$$

will satisfy the condition.  $\underline{b}_1$ ,  $\underline{b}_2$  and  $\underline{b}_3$  are the basis vectors of the reciprocal unit cell and  $h_1$ ,  $h_2$  and  $h_3$  are positive integers. These

could be given the values  $1, 2, \dots, L_{1,2,3}$  but it is customary to take an equivalent set of  $L_1 \times L_2 \times L_3$  points which are confined to the first Brillouin zone. The density of these points is seen to be  $V/(2\pi)^3$ , where  $V$  is the volume of the crystal. The assumption is certainly justified as long as the range of the interaction potential is small compared to the dimension of the real crystal.

Adiabatic Approximation A solid can be considered in terms of interacting nuclei and electrons. Assuming negligible mass for the electrons it is possible to consider the nuclear motion of the lattice independent of the electronic motion. Effectively this means that the electrons follow the nuclei instantaneously in their motions. The validity of such an approximation depends on whether the vibrational frequencies are well below the frequencies associated with electronic transitions.

Harmonic Approximation The potential energy  $\phi$  of a crystal can be written as a function of the positions of all atoms. If the atoms are executing small vibrations around their equilibrium positions it is justified to write this potential energy as a Taylor series in the displacements

$$\phi = \phi_0 + \phi_1 + \phi_2 + \dots \quad (2.1)$$

$\phi_0$  is the static potential energy for the atoms in the equilibrium positions.

$$\phi_1 = \sum_{1,\kappa,\alpha} \phi_\alpha(1\kappa) u_\alpha(1\kappa) \quad (2.2)$$

$$\text{with } \phi_\alpha(1\kappa) = \frac{\partial \phi}{\partial u_\alpha(1\kappa)}$$

$$\phi_2 = \frac{1}{2} \sum_{1,\kappa,\alpha} \sum_{1',\kappa',\beta} \phi_{\alpha\beta}(1\kappa;1'\kappa') u_\alpha(1\kappa) u_\beta(1'\kappa') \quad (2.3)$$

$$\text{with } \phi_{\alpha\beta}(1\kappa;1'\kappa') = \frac{\partial^2 \phi}{\partial u_\alpha(1\kappa) \partial u_\beta(1'\kappa')}$$

Section 2.1.

In the harmonic approximation all higher order terms beyond the second order are neglected.  $\phi_\alpha(1\kappa)$  is the negative of the force in the  $\alpha$ -direction on the atom of type  $\kappa$  in unit cell 1. It is evident that in the equilibrium configuration this force, and hence  $\phi_1$ , must vanish. Therefore, apart from the constant term  $\phi_0$ , the potential energy can be written as a quadratic expression in the atomic displacements. Because of this approximation the vibrations in the crystal can be treated as independent normal modes or quantum-mechanically as a set of non-interacting phonons. In a later chapter it will be shown that if the atoms also carry a dipole moment the potential energy can be written as a quadratic expression in the displacements and the dipole moments.

In expression (2.3)  $\phi_{\alpha\beta}(1\kappa;1'\kappa')$  is an interatomic force constant; it is the negative of the force on atom  $(1\kappa)$  in the direction  $\alpha$  if atom  $(1'\kappa')$  is moved unit distance in the direction  $\beta$ . Since this force constant has been defined as a derivative of a scalar function, the order of differentiation may be interchanged and

$$\phi_{\beta\alpha}(1'\kappa';1\kappa) = \phi_{\alpha\beta}(1\kappa;1'\kappa') \quad (2.4)$$

Further it follows from the translational invariance of the lattice that

$$\sum_{1'\kappa'} \phi_{\alpha\beta}(1\kappa;1'\kappa') = 0 \quad (2.5)$$

From expression (2.3) for the potential energy the equations of motion can be obtained

$$m_\kappa \ddot{u}_\alpha(1\kappa) = - \frac{\partial \phi_2}{\partial u_\alpha(1\kappa)} = - \sum_{1',\kappa',\beta} \phi_{\alpha\beta}(1\kappa;1'\kappa') u_\beta(1'\kappa') \quad (2.6)$$

$m_\kappa$  is the mass of the atom of type  $\kappa$ .

A solution for these equations is

$$\underline{u}(1\kappa) = \sum_{\underline{q}} (m_\kappa)^{-\frac{1}{2}} \underline{\xi}(\kappa,\underline{q}) e^{i[\underline{q}\cdot\underline{r}(1\kappa) - \omega(\underline{q})t]} \quad (2.7)$$

$\underline{r}(l\kappa)$  is the position of the atom of type  $\kappa$  in the unit cell with its origin at position  $\underline{r}(l)$ ;  $\underline{r}(l\kappa)$  can be written as the sum of  $\underline{r}(l)$  and  $\underline{r}(\kappa)$ . Expression (2.7) is a summation of plane waves each characterized by three quantities: the wave vector  $\underline{q}$ , the angular frequency  $\omega(\underline{q})$  and the polarization vector  $\underline{\xi}(\kappa, \underline{q})$ . According to this definition the polarization vector is equal to the amplitude  $\eta(\kappa, \underline{q})$  of the wave multiplied by  $m_{\kappa}^{\frac{1}{2}}$ . The summation in (2.7) is over all wave vectors in the first Brillouin zone. Substituting (2.7) into Eq. (2.6) a set of homogeneous linear equations in the components of the polarization vectors is obtained for each vector  $\underline{q}$ .

$$\omega^2(\underline{q}) \xi_{\alpha}(\kappa, \underline{q}) = \sum_{\kappa' \beta} D_{\alpha\beta}(\kappa\kappa'; \underline{q}) \xi_{\beta}(\kappa', \underline{q}) \quad (2.8)$$

where

$$D_{\alpha\beta}(\kappa\kappa'; \underline{q}) = (m_{\kappa} m_{\kappa'})^{-\frac{1}{2}} \sum_{l, l'} \phi_{\alpha\beta}(l\kappa; l'\kappa') e^{i\underline{q} \cdot [\underline{r}(l'\kappa') - \underline{r}(l\kappa)]} \quad (2.9)$$

The dynamical matrix contains as elements the coefficients  $D_{\alpha\beta}(\kappa\kappa'; \underline{q})$ , the so-called coupling coefficients\*. It is of the order  $3s$  if  $s$  is the number of atoms in the primitive unit cell i.e. if the crystal lattice can be described as  $s$  interpenetrating Bravais lattices.

Eq. (2.8) has the form of a matrix eigenvalue problem and the condition that this can be solved is, that the determinant of the coefficients vanishes.

$$\left| D_{\alpha\beta}(\kappa\kappa'; \underline{q}) - \delta_{\alpha\beta} \delta_{\kappa\kappa'} \omega^2(\underline{q}) \right| = 0 \quad (2.10)$$

Solving this determinant provides the  $3s$  eigenvalues  $\omega^2(\underline{q})$  and eigenvectors  $e(\underline{q})$ .  $\omega(\underline{q})$ , the dispersion relation, is thus seen to be a function with  $3s$  branches. Both the eigenvalues and the eigenvectors should be labelled by an index  $j$  in order to specify the branch they are associated with. For each  $j$  the  $s$  polarization vectors  $\underline{\xi}(\kappa, \underline{q}, j)$  are the components of the corresponding eigenvector. From the property (2.4)

\* In fact this is the Fourier-transformed dynamical matrix, while the force constant matrices form the dynamical matrix, but following the general convention this terminology will be used.

Section 2.1.

of the force constants and the definition (2.9) of the dynamical matrix elements it is easily seen that these satisfy the relation

$$D_{\beta\alpha}(\kappa'\kappa;\underline{q}) = D_{\alpha\beta}^*(\kappa\kappa';\underline{q}) \quad (2.11)$$

which means that in general the dynamical matrix is Hermitian. From this result it follows that the eigenvalues are real and that the eigenvectors can be chosen such that they satisfy the orthonormality and closure conditions

$$\sum_{\kappa\alpha} \xi_{\alpha}^*(\kappa,\underline{qj}) \xi_{\alpha}(\kappa,\underline{qj}') = \delta_{jj'} \quad (2.12)$$

$$\sum_j \xi_{\alpha}^*(\kappa,\underline{qj}) \xi_{\beta}(\kappa',\underline{qj}) = \delta_{\alpha\beta} \delta_{\kappa\kappa'}$$

In order to provide the polarization vectors  $\underline{\xi}(\kappa,\underline{q})$  with their proper relative phase factors, (2.7) will be written as

$$\underline{u}(1\kappa) = \sum_{\underline{q}} (m_{\kappa})^{-\frac{1}{2}} \left\{ \underline{\xi}(\kappa,\underline{q}) e^{i\underline{q}\cdot\underline{r}(\kappa)} \right\} e^{i[\underline{q}\cdot\underline{r}(1) - \omega(\underline{q})t]} \quad (2.13)$$

where the factor between braces should be considered as the polarization vector. The polarization vectors and eigenvectors, defined in this way, can easily be obtained from a dynamical matrix of which the elements, defined by (2.9), have been multiplied by a factor

$$\rho(\kappa\kappa';\underline{q}) = e^{-i\underline{q}\cdot[\underline{r}(\kappa') - \underline{r}(\kappa)]} \quad (2.14)$$

In calculations according to this theory the required force constants may be evaluated from elastic constants and other physical data or they may be obtained as parameters in a model, which is fitted to the measurements. The first procedure is usually a good starting point for the second.

2.2. Long-wavelength method

For very small wave vectors the theory of lattice dynamics should produce the same elastic sound waves as result from the theory of elasticity. In order to make the comparison between the dynamical equations for these long acoustic waves and the expressions for elastic waves, Born<sup>1)</sup> applied a perturbation method to the dynamical equations (2.8). In these equations the coupling coefficients as well as the angular frequencies and the polarization vectors can be expanded with respect to  $\underline{q}$ . They can be written as

$$D(\kappa\kappa';\underline{q}) = D^{(0)}(\kappa\kappa';\underline{q}) + D^{(1)}(\kappa\kappa';\underline{q}) + D^{(2)}(\kappa\kappa';\underline{q}) + \dots \quad (2.15)$$

where for the sake of convenience the subscripts  $\alpha$  and  $\beta$  have been omitted and

$$\begin{aligned} D^{(0)}(\kappa\kappa';\underline{q}) &= (m_{\kappa}m_{\kappa'})^{-\frac{1}{2}} \sum_{\underline{l}'} \phi(1\kappa;1'\kappa') \\ D^{(1)}(\kappa\kappa';\underline{q}) &= (m_{\kappa}m_{\kappa'})^{-\frac{1}{2}} i \sum_{\underline{l}'} \phi(1\kappa;1'\kappa') \left\{ \underline{q} \cdot [\underline{r}(1'\kappa') - \underline{r}(1\kappa)] \right\} \\ D^{(2)}(\kappa\kappa';\underline{q}) &= -\frac{1}{2} (m_{\kappa}m_{\kappa'})^{-\frac{1}{2}} \sum_{\underline{l}'} \phi(1\kappa;1'\kappa') \left\{ \underline{q} \cdot [\underline{r}(1'\kappa') - \underline{r}(1\kappa)] \right\}^2 \end{aligned} \quad (2.16)$$

$$\omega(\underline{qj}) = \omega^{(1)}(\underline{qj}) + \omega^{(2)}(\underline{qj}) + \dots \quad (2.17)$$

$$\underline{\xi}(\kappa,\underline{qj}) = \underline{\xi}^{(0)}(\kappa,\underline{qj}) + \underline{\xi}^{(1)}(\kappa,\underline{qj}) + \underline{\xi}^{(2)}(\kappa,\underline{qj}) + \dots \quad (2.18)$$

After substitution into Eq. (2.8) the terms of the same order in  $\underline{q}$  should be equal.

$$\text{Zero-th order } 0 = \sum_{\kappa'} D^{(0)}(\kappa\kappa';\underline{q}) \underline{\xi}^{(0)}(\kappa',\underline{qj}) \quad (2.19)$$

$$\text{First order } 0 = \sum_{\kappa'} \left\{ D^{(1)}(\kappa\kappa';\underline{q}) \underline{\xi}^{(0)}(\kappa',\underline{qj}) + D^{(0)}(\kappa\kappa';\underline{q}) \underline{\xi}^{(1)}(\kappa',\underline{qj}) \right\} \quad (2.20)$$

$$\begin{aligned} \text{Second order } \left\{ \omega^{(1)}(\underline{qj}) \right\}^2 \underline{\xi}^{(0)}(\kappa,\underline{qj}) &= \sum_{\kappa'} \left[ D^{(2)}(\kappa\kappa',\underline{q}) \underline{\xi}^{(0)}(\kappa',\underline{qj}) \right. \\ &\quad \left. + D^{(1)}(\kappa\kappa';\underline{q}) \underline{\xi}^{(1)}(\kappa',\underline{qj}) + D^{(0)}(\kappa\kappa';\underline{q}) \underline{\xi}^{(2)}(\kappa',\underline{qj}) \right] \end{aligned} \quad (2.21)$$

Section 2.2.

With condition (2.5) the zero order equation (2.19) is found to have as solutions  $\underline{\xi}^{(0)}(\kappa', \underline{qj}) = m_{\kappa}^{\frac{1}{2}} \underline{\eta}^{(0)}(\underline{qj})$ . This means that to zero-th order all atoms vibrate with the same amplitude  $\underline{\eta}^{(0)}(\underline{qj})$ . The  $\underline{q}$ -dependence will be discussed in connection with the second order equation. The first order equation is a set of inhomogeneous linear equations in  $\underline{\xi}^{(1)}(\kappa', \underline{qj})$  for a given amplitude  $\underline{\eta}(\underline{qj})$ . In matrix notation

$$D^{(0)} \underline{\xi}^{(1)} = f(\kappa, \underline{q}) \cdot \underline{\eta}^{(0)}(\underline{qj}) \quad (2.22)$$

where  $f(\kappa, \underline{q}) = - \sum_{\kappa'} m_{\kappa'}^{\frac{1}{2}} D^{(1)}(\kappa \kappa'; \underline{q})$

By inversion of  $D^{(0)}$  this can be solved and  $\underline{\xi}^{(1)}$  expressed in terms of  $\underline{\xi}^{(0)}$

$$\underline{\xi}^{(1)} = D^{(0)^{-1}} \cdot f(\kappa, \underline{q}) \underline{\eta}^{(0)}(\underline{qj}) \quad (2.23)$$

After multiplying (2.21) by  $m_{\kappa}^{\frac{1}{2}}$  and taking their sum the last term vanishes and

$$\sum_{\kappa} m_{\kappa}^{\frac{1}{2}} \left\{ \omega^{(1)}(\underline{qj}) \right\}^2 \underline{\xi}^{(0)}(\kappa, \underline{qj}) = \sum_{\kappa \kappa'} m_{\kappa}^{\frac{1}{2}} \left[ m_{\kappa'}^{\frac{1}{2}} D^{(2)}(\kappa \kappa'; \underline{q}) \underline{\eta}^{(0)}(\underline{qj}) + D^{(1)}(\kappa \kappa'; \underline{q}) \underline{\xi}^{(1)}(\kappa', \underline{qj}) \right] \quad (2.24)$$

With  $\frac{1}{v_a} \sum_{\kappa} m_{\kappa} = \rho$  and (2.23) this can simply be written as

$$\rho \omega^2(\underline{qj}) \underline{\eta}^{(0)}(\underline{qj}) = F(\underline{q}) \underline{\eta}^{(0)}(\underline{qj}) \quad (2.25)$$

$F(\underline{q})$  is a function of the wave vector with the force constants as parameters. From expressions (2.16) and (2.18) it can be seen that  $F(\underline{q})$  consists of only second order terms of  $\underline{q}$ . This equation must be equivalent to the vibrational equation from the macroscopic theory of elasticity.

$$\rho \omega^2 \underline{\eta} = K(\underline{q}) \underline{\eta} \quad (2.26)$$

with 
$$K_{\alpha\gamma}(\underline{q}) = \sum_{\beta\delta} a_{\alpha\beta,\gamma\delta} q_{\beta} \cdot q_{\delta}$$

where the coefficients  $a_{\alpha\beta,\gamma\delta}$  are related to Voigt's elastic constants  $c_{\lambda\lambda'}$  in the following manner.

$\alpha\beta$	11	22	33	23(32)	31(13)	12(21)
$\gamma\delta$						
$\lambda$	1	2	3	4	5	6
$\lambda'$						

Equating the coefficients of equal orders of  $q$  in  $F(\underline{q})$  and  $K(\underline{q})$  relations between elastic constants and force constants can be established.

Thus  $c_{11} = c_{11,11}$  is the coefficient of  $q_1^2$  in  $F_{11}(\underline{q})$

$c_{44} = c_{23,23}$  is the coefficient of  $q_3^2$  in  $F_{22}(\underline{q})$

$c_{12} + c_{66} = c_{11,22} + c_{12,21}$  is the coefficient of  $q_1q_2$  in  $F_{12}(\underline{q})$

For the crystal lattices discussed in this investigation  $c_{66} = c_{44}$  so that  $c_{11}$ ,  $c_{12}$  and  $c_{44}$  can be determined in this way.

### 2.3. Group-theoretical treatment of the dynamical matrix

The lattice-dynamical problem has been formulated generally in Eq. (2.8) together with its secular determinant (2.10). As long as the crystal is a simple Bravais lattice this determinant is of order three and can easily be solved. For crystal lattices with more atoms per unit cell the proportionally larger dynamical matrix requires a more general procedure for diagonalization. Besides that, there is a stronger need for the eigenvectors in such cases, since they determine the value of the differential cross-section for the neutron scattering process. For the solution of such a larger and generally formulated dynamical problem numerical procedures are available, but apart from being often time consuming they mostly fail to produce the correct eigenvectors in case of degeneracies. Moreover, they do not in general provide a proper insight in the symmetry of the eigenvectors. Since the investigations are almost always limited to planes and directions of

Section 2.3.

symmetry for the  $\underline{q}$ -vector, the symmetry relations of the system impose certain restrictions, which will simplify the general formulation of its dynamics. To work out the implications of the symmetry of the system group theory provides an excellent scheme. In recent years a number of publications<sup>3,4,5)</sup> appeared, in which the group-theoretical methods are treated in great detail. In what follows it will be shown that the power of this technique is found in the reduction and block-diagonalization of the dynamical matrix and the determination of the eigenvectors. The latter are found as the basis vectors of certain irreducible representations and the dispersion relations can be labelled according to these representations.

It has been shown<sup>3,4)</sup> that the dynamical matrix  $D(\underline{q})$  is invariant under those space-group operations of which the purely rotational part leaves the wave vector  $\underline{q}$  unchanged. Together such operations form a group  $G(\underline{q})$ , which is a subgroup of the crystal space group. This subgroup, usually called the group of the wave vector, plays a major role in the application of group theory in lattice dynamics. For the further treatment a set of matrices is required, which form a representation of this group. Chen<sup>3)</sup> and Maradudin and Vosko<sup>4)</sup> pointed out that such a representation can conveniently be obtained from the transformation law for the eigenvectors. If a space-group element  $\{R\} = \{R|\underline{t}\}$ , denoting a rotation  $R$  and a translation  $\underline{t}$ , operates on a crystal, it will take the crystal into itself and the eigenvector  $e(\underline{q},j)$  will be transformed into  $e'(R\underline{q},j)$  such that

$$e'(R\underline{q},j) = \Gamma(\underline{q},\{R\}) \cdot e(\underline{q},j) \quad (2.27)$$

The matrix elements in (2.27) have the form

$$\Gamma_{\alpha\beta}(\kappa\kappa';\underline{q}\{R\}) = R_{\alpha\beta} \delta(\kappa, F_0(\kappa',\{R\})) \cdot e^{i\underline{q}[\underline{r}(\kappa) - \{R\}\underline{r}(\kappa')]} \quad (2.28)$$

Here  $F_0(\kappa',\{R\})$  determines the kind of atom into which atom  $\kappa'$  is transformed under operation  $\{R\}$ . Maradudin and Vosko<sup>4)</sup> modified this transformation law such as to express it in terms of matrices  $T(\underline{q},R)$ .

$$\Gamma(\underline{q}, \{R\}) = e^{-i\underline{q} \cdot \underline{t}} T(\underline{q}, R) \quad (2.29)$$

with

$$T_{\alpha\beta}(\kappa\kappa'; \underline{q}, R) = R_{\alpha\beta} \delta(\kappa, F_0(\kappa'; \{R\})) e^{i\underline{q} \cdot [\underline{r}(\kappa) - R\underline{r}(\kappa')]} \quad (2.30)$$

With each element of the point group  $G_0(\underline{q})$  of the wave vector is now associated a matrix  $T$ . This one-to-one correspondence does not imply that  $T$  is a representation. In ref. 4 it is shown that the multiplication rules should be written as

$$T(\underline{q}, R_i) \cdot T(\underline{q}, R_j) = \phi(\underline{q}; R_i, R_j) \cdot T(\underline{q}, R_i R_j) \quad (2.31)$$

where

$$\phi(\underline{q}; R_i, R_j) = e^{2\pi i \underline{b}(\underline{q}, R_i^{-1}) \cdot \underline{v}(R_j)} \quad (2.32)$$

is the multiplier. Therefore,  $T$  is called a multiplier representation. In the multiplier  $\underline{b}(\underline{q}, R_i^{-1})$  is a reciprocal lattice vector such that  $R_i^{-1} \underline{q} = \underline{q} - 2\pi \underline{b}(\underline{q}, R_i^{-1})$  and  $\underline{v}(R_j)$  is that part of the translation  $\underline{t}$  of operator  $R$ , which represents a translation by less than a unit cell period such as a translation associated with a glide plane or a screw axis. If  $\underline{q}$  is a wave vector within the first Brillouin zone, then  $\underline{b}(\underline{q}, R) = 0$  and if the space group is symmorphic then  $\underline{v}(R) = 0$ . In both cases the multiplier becomes equal to one and consequently the matrices  $T$  form an ordinary representation of the group. Since the transformation matrices  $\Gamma$  are unitary matrices commuting with the dynamical matrix, this also holds for the matrices  $T$

$$T^{-1}(\underline{q}, R) \cdot D(\underline{q}) \cdot T(\underline{q}, R) = D(\underline{q}) \quad (2.33)$$

Because of this invariance condition the matrices  $T(\underline{q}, R)$  can be used to block-diagonalize the dynamical matrix. However, this set of matrices is much more important for the characterization and labelling of the branches of the dispersion relation, the determination of degeneracies and for finding the eigenvectors.

Section 2.3.

In general the representation  $T$  is a reducible one and by means of the decomposition formula it can be separated into its irreducible parts.

$$c_{\alpha} = h^{-1} \sum_i \chi^{\alpha*}(R_i) \chi_T(R_i) \quad (2.34)$$

Here  $\chi_T(R_i)$  is the trace of  $T(\underline{q}, R_i)$ ,  $\chi^{\alpha}(R_i)$  is the character of the  $\alpha$ -th irreducible representation,  $h$  is the number of elements of the group and the summation is over all these elements. The reducible representation  $T$  can now be written as

$$T = \sum_{\alpha} c_{\alpha} \tau^{\alpha} \quad (2.35)$$

where  $\tau^{\alpha}$  are the irreducible representations of the group. If the  $\alpha$ -th irreducible representation is of dimension  $n_{\alpha}$ , in the block-diagonalized dynamical matrix a submatrix of order  $c_{\alpha}$  will occur  $n_{\alpha}$  times degenerate. This information could be obtained from the knowledge of the character tables of the irreducible representation only, but without knowing the representations themselves.

For finding the eigenvectors of the dynamical matrix the projection-operator technique is applied and this requires the irreducible representations of  $G_0(\underline{q})$ . Therefore, it is only since a complete set of irreducible representations for the crystal space groups became available<sup>7)</sup>, that the application of this method has been stimulated. The projection-operator for the irreducible-matrix element  $\tau_{\lambda\mu}^{\alpha}(\underline{q}, R)$  and the matrix  $T(\underline{q}, R)$  is defined as

$$P_{\lambda\mu}(\underline{q}, \alpha) = \sum_i \tau_{\lambda\mu}^{\alpha*}(\underline{q}, R_i) \cdot T(\underline{q}, R_i) \quad (2.36)$$

Operating on an arbitrary 3s-dimensional vector it projects out the basis vector belonging to the  $\lambda$ -th row of  $\tau^{\alpha}$  *i.e.* it projects out that part of the vector, which transforms according to the  $\lambda$ -th row of the  $\alpha$ -th irreducible representation.

$$P_{\lambda\mu}(\underline{q}, \alpha) \cdot \psi = E(\underline{q}, \alpha\lambda) \quad (2.37)$$

These vectors are automatically orthogonal but not necessarily normalized. If  $\tau^\alpha$  occurs once in the decomposition (2.35), then  $E(\underline{q}, \alpha\lambda)$  is equal to the eigenvector  $e(\underline{q}, \alpha\lambda)$  of  $D(\underline{q})$ . If  $\tau^\alpha$  occurs more than once in (2.35), then  $E(\underline{q}, \alpha\lambda)$  is not a real eigenvector but a so-called symmetry adapted eigenvector with the property

$$D(\underline{q}) \cdot E(\underline{q}, \alpha\lambda) = \omega^2(\underline{q}, \alpha) \cdot E(\underline{q}, \alpha\lambda) \quad (2.38)$$

This symmetry adapted eigenvector is a linear combination of eigenvectors of  $D(\underline{q})$ . Eq. (2.38) comprises another matrix eigenvalue problem but of a much lower order than in the original dynamical matrix. The generally formulated problem of Eq. (2.8) has now been reduced to as many smaller problems of the type (2.38) as there are irreducible representations in the decomposition. The product of the secular determinants for each of the equations (2.38) forms the block-diagonalization of the dynamical matrix. The eigenvectors of (2.38) are the components of the eigenvectors of the dynamical matrix and they must be substituted into expression (2.37) for the symmetry adapted eigenvectors.

The block-diagonalization can also be achieved by a slightly different procedure. The symmetry adapted eigenvectors can usually be decomposed into a number of independent orthonormal vectors. From group theory it is known that all these vectors together form a unitary matrix  $U(\underline{q})$  which block-diagonalizes  $T(\underline{q})$  and since  $D(\underline{q})$  and  $T(\underline{q})$  commute (Eq. (2.33)),  $U(\underline{q})$  will also block-diagonalize  $D(\underline{q})$ .

$$U(\underline{q}) \cdot D(\underline{q}) \cdot U(\underline{q}) = D(\underline{q}) \quad (2.39)$$

However, the first procedure is simpler and allows a more direct determination of the eigenvectors.

Apart from accidental degeneracies in the dispersion relation and in addition to those due to the multidimensionality of some of the irreducible representations of the group of the wave vector time-reversal symmetry can be a third reason for degeneracies. Time-reversal implies the substitution of  $-t$  for  $t$  in the normal modes (2.7) and taking their complex conjugates. It has been pointed out by Herring<sup>8)</sup>

Section 2.3.

that the symmetry of this operation can produce extra degeneracies.

If the point group of the crystal contains an anti-unitary operation  $A_0$  which transforms  $\underline{q}$  into  $-\underline{q}$ , it forms with the group  $G_0(\underline{q})$  the coset  $A_0 G_0(\underline{q})$ . The group and the coset together form the group  $G_0(\underline{q}; -\underline{q})$  which consists of elements which either leave  $\underline{q}$  invariant or transform it into  $-\underline{q}$ . Herring showed that under the influence of such an anti-unitary operation the irreducible representations separate into three types. For the irreducible multiplier representations<sup>4)</sup> these three types can be distinguished according to the value of

$$w(\tau^\alpha) = \sum_A \phi(\underline{q}; A, A) \chi^{\tau^\alpha}(\underline{q}, A^2) \quad (2.40)$$

Here  $A = A_0 R$ ,  $R$  is an element of  $G_0(\underline{q})$  and  $A$  one of the coset.

- Type 1 :  $w(\tau^\alpha) = h$     no additional degeneracies
- Type 2 :  $w(\tau^\alpha) = -h$     time-reversal symmetry exists and the subspace of  $\tau^\alpha$  is degenerate with an equivalent subspace
- Type 3 :  $w(\tau^\alpha) = 0$     time-reversal symmetry exists and the subspace of  $\tau^\alpha$  is degenerate with an inequivalent subspace.

Since in symmorphic space groups the multiplier is equal to unity expression (2.40) can be written as

$$w(\tau^\alpha) = \sum_A \chi^{\tau^\alpha}(\underline{q}, A^2) \quad (2.41)$$

References

- 1) M. Born and K. Huang, Dynamical Theory of Crystal Lattices, Oxford University Press, 1956.
- 2) A.A. Maradudin, E.W. Montroll and G.H. Weiss, Solid State Physics, edited by F. Seitz and D. Turnbull (Academic Press, Inc., New York 1963), Suppl.3.
- 3) S.H. Chen, Phys. Rev. 163 (1967), 532.
- 4) A.A. Maradudin and S.H. Vosko, Rev. Mod. Phys. 40 (1968), 1.
- 5) J.L. Warren, Rev. Mod. Phys. 40 (1968), 38.
- 6) G. Ya. Lyubarskii, The Application of Group Theory in Physics, Pergamon Press, Inc., New York (1960).
- 7) O.V. Kovalev, Irreducible Representations of the Space Groups, (Academy of Sciences USSR Press, Kiev 1961; English translation: Gordon and Breach Science Publishers, New York 1965).
- 8) C. Herring, Phys. Rev. 52 (1937), 361.

Chapter III

LATTICE DYNAMICS OF IONIC AND COVALENT CRYSTALS

3.1. Rigid ion model

The energy of a non-metallic crystal is usually divided into two parts - one from the Coulomb interaction of point charges, dipoles and higher multipole moments, which are long-range interactions, and the other from an overlap or exchange potential which results in a short-range covalent bond or repulsive force. From the definitions (2.3) and (2.9) for the force constants and the coupling coefficients it is obvious that each element of the dynamical matrix may be divided into parts corresponding to the short-range and to the Coulomb potential, respectively.

$$D(\mathbf{q}) = D^R(\mathbf{q}) + D^C(\mathbf{q}) \quad (3.1)$$

For the short-range interactions the terms in summation (2.9) can be arranged into a few groups each of which corresponds to interactions of a central atom with a certain type of neighbouring atoms

$$D_{\alpha\beta}^R(\kappa\kappa';\mathbf{q}) = (m_{\kappa} m_{\kappa'})^{-\frac{1}{2}} \sum_t \sum_{l'_t} \phi_{\alpha\beta}^R(l\kappa; l'_t\kappa') e^{i\mathbf{q} \cdot [\mathbf{r}(l'_t\kappa') - \mathbf{r}(l\kappa)]} \quad (3.2)$$

Here the first summation is over the different sets of neighbours including, if  $\kappa = \kappa'$ , the central atom itself; the quantity  $\phi_{\alpha\beta}^R(l\kappa, l\kappa)$  can be obtained from Eq. (2.5). The second summation is over all atoms belonging to one such a set.  $\phi_{\alpha\beta}^R(l\kappa, l'_t\kappa')$  is the short-range part of the force constant in (2.9). For the first few sets of neighbours in a crystal of high symmetry such interactions can be described by means of a few force constants, because of the symmetry of the lattice. Therefore, if only first and second neighbours are taken into account, the contribution of the short-range interactions to the coupling coefficients can be formulated in terms of a small number of parameters.

The simplest model including electrostatic forces is the rigid ion model, which describes the Coulomb interaction as due to point charges. The potential energy for the interaction of point charges can be

obtained from classical electrostatics. If  $Z_{\kappa}$  and  $Z_{\kappa'}$  are the electrostatic charges of the atoms of type  $\kappa$  and  $\kappa'$ , respectively, both in units of the electron charge, then the Coulomb contribution to the potential energy is

$$\phi^C = \sum'_{\substack{1\kappa \\ 1'\kappa'}} \frac{Z_{\kappa} Z_{\kappa'} e^2}{|\underline{r}(1'\kappa') - \underline{r}(1\kappa)|} \quad (3.3)$$

The prime indicates that the divergent terms due to the Coulomb self-interaction of a point charge must be omitted. According to Eq. (2.9) the Coulomb contribution to the coupling coefficients is then given by

$$D^C(\kappa\kappa'; \underline{q}) = (m_{\kappa} m_{\kappa'})^{-\frac{1}{2}} Z_{\kappa} C(\kappa\kappa'; \underline{q}) Z_{\kappa'} \quad (3.4)$$

with

$$C(\kappa\kappa'; \underline{q}) = \sum_1 \frac{\partial^2}{\partial \underline{r}(\kappa) \partial \underline{r}(\kappa')} \left( \frac{e^2}{|\underline{r}(1\kappa') - \underline{r}(\kappa)|} \right) e^{i\underline{q} \cdot [\underline{r}(1\kappa') - \underline{r}(\kappa)]} \quad (3.5)$$

Because of the long-range nature of the Coulomb potential the evaluation of this contribution to the coupling coefficients is more difficult than for the short-range forces, since this series is only slowly convergent so that interactions with a large number of neighbouring atoms must be included. However, by substitution of the identity

$$\frac{1}{|\underline{r}(1\kappa') - \underline{r}(\kappa)|} = \frac{2}{\sqrt{\pi}} \int_0^{\infty} e^{-|\underline{r}(1\kappa') - \underline{r}(\kappa)|^2 \rho^2} d\rho \quad (3.6)$$

into (3.5) and interchanging integration and summation Ewald<sup>1,2)</sup> could write the coupling coefficients as an integral, of which the integrand is a periodic function of  $\underline{r}(\kappa)$ . This function can be represented by a Fourier series, which is a summation over points in the reciprocal lattice. By means of the Ewald parameter  $R_E$  the integral can be split into two parts. For  $\rho$  from 0 to  $R_E$  the summation in the reciprocal lattice is used and from  $R_E$  to  $\infty$  the summation in the crystal lattice. After integration the Coulomb coupling coefficients can be written as the sum of two series, each of which converges much more rapidly.

Section 3.1.

$$C_{\alpha\beta}(\kappa\kappa';\mathbf{q}) = \frac{e^2}{v_a} \left\{ 4\pi \cdot \frac{q_\alpha q_\beta}{|\mathbf{q}|^2} \cdot e^{-\frac{|\mathbf{q}|^2}{4R_E^2}} + \frac{\pi}{R_E^2} \sum_h' (\mathbf{b}_h + \mathbf{q})_\alpha (\mathbf{b}_h + \mathbf{q})_\beta G\left[\frac{|\mathbf{b}_h + \mathbf{q}|^2}{4R_E^2}\right] \cdot e^{i\mathbf{b}_h \cdot [\mathbf{r}(\kappa) - \mathbf{r}(\kappa')]} - v_a R_E^3 \sum_l H_{\alpha\beta}\left[R_E |\mathbf{r}(l\kappa') - \mathbf{r}(\kappa)|\right] \cdot e^{i\mathbf{q} \cdot [\mathbf{r}(l\kappa') - \mathbf{r}(\kappa)]} \right\} \quad (3.7)$$

Here

$$G(x) = \frac{e^{-x}}{x} \quad (3.8)$$

$$H_{\alpha\beta}(x) = \left\{ \frac{3}{x^5} [1-F(x)] + \frac{6}{\sqrt{\pi}} \cdot \frac{e^{-x^2}}{x^4} + \frac{4}{\sqrt{\pi}} \cdot \frac{e^{-x^2}}{x^2} \right\} x_\alpha x_\beta - \left\{ \frac{1}{x^3} [1-F(x)] + \frac{2}{\sqrt{\pi}} \cdot \frac{e^{-x^2}}{x^2} \right\} \delta_{\alpha\beta} \quad (3.9)$$

$$F(x) = \frac{2}{\sqrt{\pi}} \int_0^x e^{-t^2} dt \quad (3.10)$$

The second term in expression (3.7) is a summation over reciprocal lattice vectors  $\mathbf{b}_h$  defined by  $\mathbf{b}_h = \frac{2\pi}{a} (h_1, h_2, h_3)$  where for face-centred cubic lattices the integers  $h_1, h_2$  and  $h_3$  are all even or all odd;  $a$  is the edge of the crystal unit cell and  $v_a$  is the volume of the primitive unit cell. The first term in (3.7) is due to the origin of the reciprocal lattice, which has been left out from the summation over  $h$ . The third term is a summation in real space over vectors  $\mathbf{r}(l)$  given by  $\mathbf{r}(l) = \frac{1}{2}a(l_x, l_y, l_z)$ ;  $l_x, l_y$  and  $l_z$  are integers, which for a face-centred cubic lattice must satisfy the condition  $\sum_i l_i = \text{even}$ .

For  $\kappa = \kappa'$  and for  $l = 0$  in the summation over  $l$  is  $H_{\alpha\beta} = \frac{4}{3\sqrt{\pi}} \delta_{\alpha\beta}$

By means of the Philips-Electrologica X8 digital computer the Coulomb coupling coefficients have been evaluated for the zinc blende and fluorite structures in the three symmetry directions  $[00z]$ ,  $[z\zeta 0]$  and  $[z\zeta z]$ . For these structures the position of the atoms are given by  $\mathbf{r}(\kappa) = \frac{1}{4}a(\kappa-1)(1,1,1)$  where  $\kappa$  may have the values 1,2 and 4. For the Ewald parameter the value  $(1/v_a)^{1/3}\sqrt{\pi}$ , which is  $\sqrt{\pi}$  times the value used

by Kaplan and Sullivan<sup>3)</sup>, has been chosen, as this gave an almost equally rapid convergence of the summations in real and reciprocal spaces. For the presentation of the results Kaplan and Sullivan's<sup>3)</sup> notation has been used; this has been summarized in Table 3.1.

Table 3.1. Form of the matrices of the Coulomb coupling coefficients in the main symmetry directions for the zinc blende and fluorite structures. Atom positions are  $\underline{r}(\kappa) = \frac{1}{4}a(\kappa-1)(1,1,1)$  with  $\kappa = 1, 2$  and  $4$ .

$(\kappa\kappa')$	$[00\zeta]$	$[\zeta\zeta 0]$	$[\zeta\zeta\zeta]$
$(\kappa = \kappa')$	$\begin{vmatrix} -A & 0 & 0 \\ 0 & -A & 0 \\ 0 & 0 & 2A \end{vmatrix}$	$\begin{vmatrix} A & B & 0 \\ B & A & 0 \\ 0 & 0 & -2A \end{vmatrix}$	$\begin{vmatrix} 0 & A & A \\ A & 0 & A \\ A & A & 0 \end{vmatrix}$
(1 2)	$\begin{vmatrix} -B & -iC & 0 \\ -iC & -B & 0 \\ 0 & 0 & 2B \end{vmatrix}$	$\begin{vmatrix} C & D & iE \\ D & C & iE \\ iE & iE & -2C \end{vmatrix}$	$\begin{vmatrix} 0 & B+iC & B+iC \\ B+iC & 0 & B+iC \\ B+iC & B+iC & 0 \end{vmatrix}$
(2 4)	$\begin{vmatrix} -D & 0 & 0 \\ 0 & -D & 0 \\ 0 & 0 & 2D \end{vmatrix}$	$\begin{vmatrix} F & G & 0 \\ G & F & 0 \\ 0 & 0 & -2F \end{vmatrix}$	$\begin{vmatrix} 0 & D & D \\ D & 0 & D \\ D & D & 0 \end{vmatrix}$

The results of the computations for the three symmetry directions have been listed in Table 3.2; the uncertainty in these numbers is  $\pm 0.0005$ . The data have been plotted versus  $\frac{a}{2\pi} \cdot \underline{q}$  in Fig. 3.1. The coupling coefficients for the interaction (1 4) are the complex conjugate of those for (1 2). Further it is evident that the values for the interaction (1 3), which would be needed in a rocksalt structure, are equivalent to those for (2 4).

The equations of motion for a rigid ionic crystal can now be written as

$$m_{\kappa} \omega^2(\underline{qj}) \xi_{\alpha}(\kappa, \underline{qj}) = \sum_{\kappa' \beta} \left[ R_{\alpha\beta}(\kappa\kappa'; \underline{q}) + Z_{\kappa} C(\kappa\kappa'; \underline{q}) Z_{\kappa'} \right] \xi_{\beta}(\kappa', \underline{qj}) \quad (3.11)$$

Section 3.1.

Table 3.2. Coupling coefficients  $C(\kappa\kappa';q)$  in units of  $\frac{e^2}{v a}$  in the directions  $[00z]$ ,  $[z\zeta 0]$  and  $[z\zeta z]$ .

$[00z]$					$[z\zeta z]$				
$\frac{a}{2\pi} \cdot q$	A	B	C	D	$\frac{a}{2\pi} \cdot q$	A	B	C	D
0	+4.1887	+4.1887	+0	+4.1887	0	+4.1887	+4.1887	+0	+4.1887
0.05	+4.1771	+4.1756	+0.7894	+4.2086	0.05	+4.1840	+4.1954	-0.4553	+4.1726
0.10	+4.1423	+4.1360	+1.5754	+4.2675	0.10	+4.1699	+4.2150	-0.9062	+4.1240
0.15	+4.0851	+4.0704	+2.3548	+4.3644	0.15	+4.1469	+4.2471	-1.3483	+4.0433
0.20	+4.0066	+3.9793	+3.1239	+4.4969	0.20	+4.1157	+4.2908	-1.7774	+3.9307
0.25	+3.9084	+3.8632	+3.8792	+4.6621	0.25	+4.0777	+4.3448	-2.1894	+3.7868
0.30	+3.7927	+3.7231	+4.6168	+4.8563	0.30	+4.0338	+4.4075	-2.5809	+3.6122
0.35	+3.6620	+3.5600	+5.3327	+5.0750	0.35	+3.9856	+4.4770	-2.9484	+3.3911
0.40	+3.5190	+3.3749	+6.0226	+5.3131	0.40	+3.9346	+4.5511	-3.2891	+3.1553
0.45	+3.3671	+3.1693	+6.6819	+5.5651	0.45	+3.8827	+4.6273	-3.6007	+2.8929
0.50	+3.2099	+2.9444	+7.3061	+5.8249	0.50	+3.8314	+4.7029	-3.8812	+2.6060
0.55	+3.0511	+2.7018	+7.8904	+6.0861	0.55	+3.7824	+4.7750	-4.1293	+2.2966
0.60	+2.8946	+2.4430	+8.4300	+6.3423	0.60	+3.7374	+4.8405	-4.3444	+1.9888
0.65	+2.7446	+2.1698	+8.9199	+6.5870	0.65	+3.6978	+4.8963	-4.5261	+1.6401
0.70	+2.6049	+1.8838	+9.3556	+6.8140	0.70	+3.6648	+4.9388	-4.6749	+1.2760
0.75	+2.4793	+1.5868	+9.7328	+7.0174	0.75	+3.6399	+4.9653	-4.7917	+0.8998
0.80	+2.3712	+1.2806	+10.0473	+7.1919	0.80	+3.6232	+4.9726	-4.8778	+0.5150
0.85	+2.2838	+0.9669	+10.2958	+7.3327	0.85	+3.6156	+4.9576	-4.9350	+0.1253
0.90	+2.2195	+0.6477	+10.4755	+7.4361	0.866	+3.6151	+4.9477	-4.9477	-0.0000
0.95	+2.1801	+0.3247	+10.5841	+7.4993					
1.00	+2.1668	-0.0001	+10.6205	+7.5205					

$[z\zeta 0]$							
$\frac{a}{2\pi} \cdot q$	A	B	C	D	E	F	G
0	+2.0943	+6.2830	+2.0943	+6.2830	+0	+2.0943	+6.2830
0.05	+2.0885	+6.2760	+2.0878	+6.2931	-0.5578	+2.1043	+6.2589
0.10	+2.0709	+6.2542	+2.0681	+6.3229	-1.1109	+2.1341	+6.1865
0.15	+2.0410	+6.2170	+2.0355	+6.3724	-1.6546	+2.1839	+6.0672
0.20	+1.9985	+6.1632	+1.9904	+6.4417	-2.1843	+2.2540	+5.9030
0.25	+1.9426	+6.0912	+1.9336	+6.5305	-2.6954	+2.3444	+5.6969
0.30	+1.8724	+5.9989	+1.8656	+6.6386	-3.1831	+2.4557	+5.4523
0.35	+1.7871	+5.8844	+1.7874	+6.7657	-3.6428	+2.5879	+5.1734
0.40	+1.6857	+5.7454	+1.7001	+6.9112	-4.0699	+2.7414	+4.8650
0.45	+1.5672	+5.5799	+1.6046	+7.0745	-4.4598	+2.9162	+4.5323
0.50	+1.4310	+5.3862	+1.5024	+7.2546	-4.8077	+3.1123	+4.1809
0.55	+1.2762	+5.1627	+1.3945	+7.4504	-5.1091	+3.3294	+3.8166
0.60	+1.1027	+4.9091	+1.2826	+7.6604	-5.3591	+3.5671	+3.4455
0.65	+0.9106	+4.6251	+1.1678	+7.8828	-5.5534	+3.8242	+3.0736
0.70	+0.7005	+4.3117	+1.0517	+8.1155	-5.6871	+4.0993	+2.7066
0.75	+0.4735	+3.9712	+0.9357	+8.3560	-5.7561	+4.3905	+2.3501
0.80	+0.2316	+3.6068	+0.8212	+8.6013	-5.7561	+4.6950	+2.0092
0.85	-0.0225	+3.2230	+0.7096	+8.8484	-5.6835	+5.0094	+1.6885
0.90	-0.2853	+2.8256	+0.6022	+9.0937	-5.5353	+5.3295	+1.3917
0.95	-0.5524	+2.4218	+0.5005	+9.3334	-5.3095	+5.6504	+1.1219
1.00	-0.8187	+2.0198	+0.4054	+9.5637	-5.0050	+5.9663	+0.8812
1.05	-1.0782	+1.6288	+0.3183	+9.7805	-4.6225	+6.2709	+0.6708
1.10	-1.3244	+1.2587	+0.2401	+9.9798	-4.1643	+6.5572	+0.4909
1.15	-1.5506	+0.9194	+0.1717	+10.1579	-3.6346	+6.8181	+0.3413
1.20	-1.7500	+0.6212	+0.1139	+10.3110	-3.0399	+7.0467	+0.2207
1.25	-1.9162	+0.3731	+0.0674	+10.4360	-2.3889	+7.2362	+0.1278
1.30	-2.0435	+0.1834	+0.0328	+10.5303	-1.6924	+7.3808	+0.0611
1.35	-2.1275	+0.0585	+0.0104	+10.5918	-0.9628	+7.4759	+0.0192
1.40	-2.1650	+0.0027	+0.0005	+10.6191	-0.2142	+7.5183	+0.0009
1.414	-2.1669	-0.0002	+0.0000	+10.6205	+0.0001	+7.5205	-0.0000

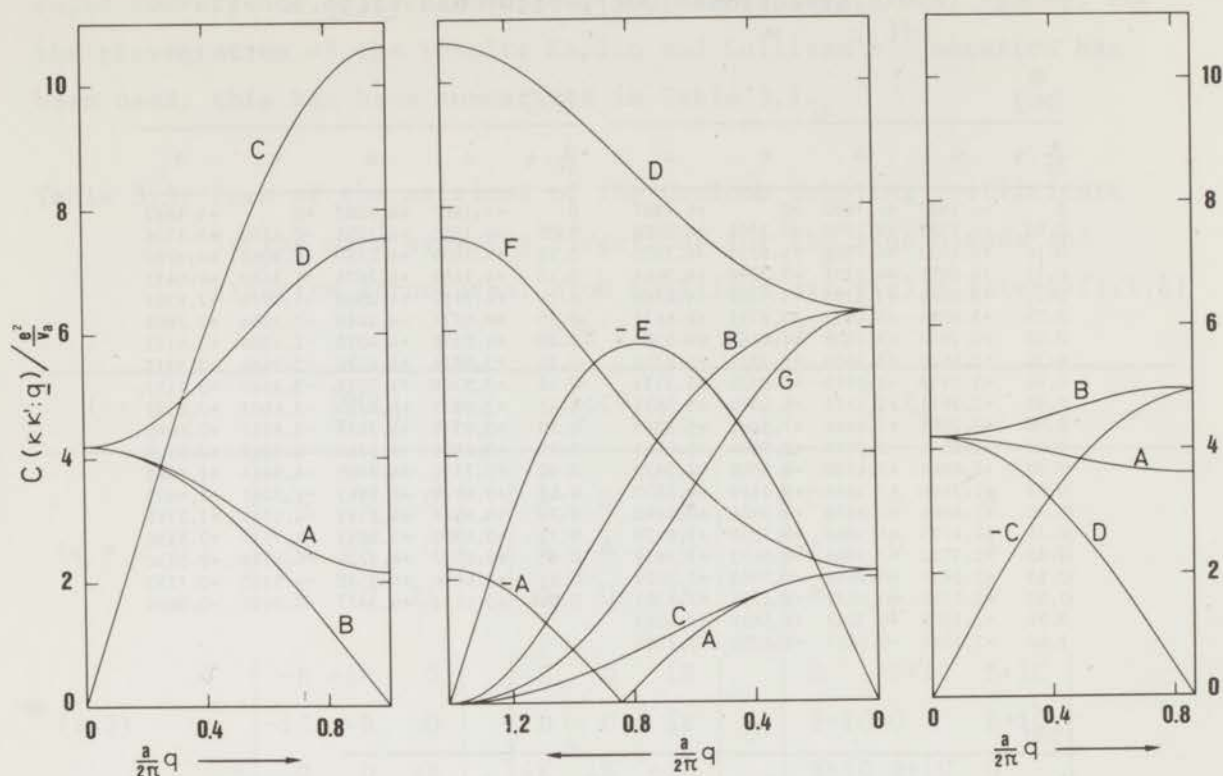


Fig. 3.1. Coupling coefficients  $C(\kappa\kappa';q)$  in units of  $\frac{e^2}{va}$  in the directions  $[00z]$ ,  $[z\zeta 0]$  and  $[z\zeta z\zeta]$ .

where

$$R_{\alpha\beta}(\kappa\kappa';q) = (m_{\kappa} m_{\kappa'})^{\frac{1}{2}} D_{\alpha\beta}^R(\kappa\kappa';q) \quad (3.12)$$

or in matrix notation

$$\omega^2 m e = (R + ZCZ) e \quad (3.13)$$

Here  $m$  and  $Z$  are diagonal matrices of the order  $3s$  containing the ionic masses and charges, respectively. This equation is the basic equation for all rigid ion model calculations. Kellerman<sup>4)</sup> applied it for the first time in calculations on the dynamics of sodium chloride. Comparisons between experimental dispersion relations and calculations based on this model usually show substantial differences for some of

Section 3.1.

the branches. Generally it is believed that this is mainly due to the too simplifying assumption of representing the electrostatic field by point charges only.

3.2. Shell model

Since the unsatisfactory description afforded by the rigid ion model is due in part to neglecting the distortions of the ions during the lattice vibrations, Dick and Overhauser<sup>5)</sup> proposed a simple model, which allowed for polarization of the ions. This model - later called the shell model - was generalized for application in lattice dynamics by Cochran<sup>6,7)</sup>. Each ion  $\kappa$  is assumed to consist of a core with charge  $X_\kappa e$  and a shell of outer electrons having a charge  $Y_\kappa e$ ; the total ionic charge is  $Z_\kappa e = (X_\kappa + Y_\kappa)e$ . The core and the shell are assumed to be bound together by an isotropic force constant  $k_\kappa$ . Without violating the adiabatic approximation the equations of motion for both cores and shells can be formulated. However, the relative motion of the shell and core of an ion, which is possible because of the finite binding force, implies the existence of a local dipole moment. It has been pointed out by Cochran<sup>7)</sup> that within the harmonic approximation the potential energy of the crystal can be expressed as a quadratic function of the nuclear displacements and the atomic dipole moments.

$$\begin{aligned} \Phi_2 = \frac{1}{2} \sum_{l\kappa\alpha} \left\{ \sum_{l'\kappa'\beta} \left[ \phi_{\alpha\beta}^R(l\kappa; l'\kappa') u_\alpha(l\kappa) u_\beta(l'\kappa') + Y_\kappa^{-1} \phi_{\alpha\beta}^T(l\kappa; l'\kappa') u_\alpha(l\kappa) p_\beta(l'\kappa') \right. \right. \\ \left. \left. + Y_\kappa^{-1} \phi_{\beta\alpha}^T(l'\kappa'; l\kappa) p_\alpha(l\kappa) u_\beta(l'\kappa') + Y_\kappa^{-1} Y_{\kappa'}^{-1} \phi_{\alpha\beta}^S(l\kappa; l'\kappa') p_\alpha(l\kappa) p_\beta(l'\kappa') \right] \right. \\ \left. + \Pi_\kappa^{-1} p_\alpha^2(l\kappa) - \left[ p_\alpha(l\kappa) + Z_\kappa u_\alpha(l\kappa) \right] E_\alpha(l\kappa) \right\} \quad (3.14) \end{aligned}$$

Here  $\underline{p}(l\kappa)$  is the dipole moment of the atom at position  $\underline{r}(l\kappa)$ ,  $\Pi_\kappa$  is its electronic polarizability and  $E(l\kappa)$  is the electric field at that position due to the remainder of the crystal. In the summation the first terms between square brackets are due to the short-range interactions.  $Y_\kappa^{-1} \underline{p}(l'\kappa')$  is the relative displacement of the shell and the core of atom  $\kappa'$  at  $\underline{r}(l'\kappa')$ .  $\phi^T(l\kappa; l'\kappa')$  is the force constant matrix for the interaction of the core at  $\underline{r}(l\kappa)$  and the shell at  $\underline{r}(l'\kappa')$  and

$\phi^S(1\kappa;1'\kappa')$  for the interaction of the two shells. The second term in the summation of (3.14) represents the electronic polarization energy and the last term is the electrostatic energy. By this formulation Cochran could retain the concept of the force constant allowing a formal treatment according to the Born-Von Karman theory. A quantum-mechanical justification of the shell model has been given by Cowley<sup>8)</sup>. Applying the procedure given in chapter II the following expressions for the equations of motion for the nuclear displacements  $\underline{U}$  and the relative displacements  $\underline{W}$  of shell and core can be obtained

$$\begin{aligned}
 m_{\kappa} \omega^2(\underline{q}) U_{\alpha}(\kappa, \underline{q}) &= \sum_{\kappa' \beta} \left[ R_{\alpha\beta}(\kappa\kappa'; \underline{q}) + Z_{\kappa} C_{\alpha\beta}(\kappa\kappa'; \underline{q}) Z_{\kappa'} \right] U_{\beta}(\kappa'; \underline{q}) \\
 &+ \sum_{\kappa' \beta} \left[ T_{\alpha\beta}(\kappa\kappa'; \underline{q}) + Z_{\kappa} C_{\alpha\beta}(\kappa\kappa'; \underline{q}) Y_{\kappa'} \right] W_{\beta}(\kappa'; \underline{q}) \\
 0 &= \sum_{\kappa' \beta} \left[ T_{\beta\alpha}^*(\kappa\kappa'; \underline{q}) + Y_{\kappa} C_{\alpha\beta}(\kappa\kappa'; \underline{q}) Z_{\kappa'} \right] U_{\beta}(\kappa'; \underline{q}) \\
 &+ \sum_{\kappa' \beta} \left[ S_{\alpha\beta}(\kappa\kappa'; \underline{q}) + \delta_{\alpha\beta} \delta_{\kappa\kappa'} \Pi_{\kappa}^{-1} Y_{\kappa}^2 + Y_{\kappa} C_{\alpha\beta}(\kappa\kappa'; \underline{q}) Y_{\kappa'} \right] W_{\beta}(\kappa'; \underline{q})
 \end{aligned} \tag{3.15}$$

The matrices T and S have been defined in an analogous manner as the matrix R by (2.9) and (3.12).  $\underline{Y}\underline{W}$  is the electric dipole moment of the ions. In accordance with the adiabatic approximation, which implies zero mass for the electron, the left-hand side of the second equation is taken to be zero. In matrix notation (3.15) can be written as

$$\begin{aligned}
 \omega^2 m \underline{U} &= (\underline{R} + \underline{Z}\underline{C}\underline{Z})\underline{U} + (\underline{T} + \underline{Z}\underline{C}\underline{Y})\underline{W} \\
 0 &= (\underline{T}^{\dagger} + \underline{Y}\underline{C}\underline{Z})\underline{U} + (\underline{S} + \underline{Y}\underline{C}\underline{Y})\underline{W}
 \end{aligned} \tag{3.16}$$

where  $\underline{S} = \underline{S} + \Pi^{-1} \underline{Y}^2 \underline{I}$ . Eliminating  $\underline{W}$  from these equations the characteristic equation for the shell model is obtained and from this the frequencies and polarization vectors can be evaluated.

$$\omega^2 m \underline{U} = \underline{M} \underline{U} \tag{3.17}$$

$$\text{with } \underline{M} = (\underline{R} + \underline{Z}\underline{C}\underline{Z}) - (\underline{T} + \underline{Z}\underline{C}\underline{Y})(\underline{S} + \underline{Y}\underline{C}\underline{Y})^{-1}(\underline{T}^{\dagger} + \underline{Y}\underline{C}\underline{Z}) \tag{3.18}$$

Section 3.2.

It is usually assumed that the short-range overlap forces act through the shells of neighbouring atoms only. Woods *et al.*<sup>9)</sup> showed that this implies that  $R = T = S$ . In this way a significant reduction of the number of parameters of the shell model has been achieved. Since  $k$  and  $Y$  are somewhat artificial model parameters, it is convenient to express them in physically more meaningful quantities as the electrical polarizability  $\Pi$  and the short-range polarizability  $d$

$$\Pi_{\kappa} = \frac{Y_{\kappa}^2 e^2}{k_{\kappa} + T(\kappa\kappa;0)} \quad \text{and} \quad d_{\kappa} = \frac{T(\kappa\kappa;0) Y_{\kappa} e}{k_{\kappa} + T(\kappa\kappa;0)} \quad (3.19)$$

This short-range polarizability is a parameter first introduced by Woods *et al.*<sup>9)</sup> and it can be considered as a measure for the polarizability of an ion under the action of short-range forces. Its contribution to the polarizability can be considered separately from the electrical polarizability.

References

- 1) P.P. Ewald, *Ann. Phys.* 64 (1921), 253.
- 2) M. Born, K. Huang, *Dynamical Theory of Crystal Lattices*, Oxford University Press, 1956, 248.
- 3) H. Kaplan, J.J. Sullivan, *Phys. Rev.* 130 (1963), 120.
- 4) E.W. Kellerman, *Phil Trans. Roy. Soc.* A238 (1940), 513.
- 5) B.G. Dick, A.W. Overhauser, *Phys. Rev.* 112 (1958), 90.
- 6) W. Cochran, *Adv. Phys.* 10 (1961), 401.
- 7) W. Cochran, *Proc. Roy. Soc.* A253 (1959), 260.
- 8) R.A. Cowley, *Proc. Roy. Soc.* A268 (1962), 109.
- 9) A.D.B. Woods, W. Cochran, B.N. Brockhouse, *Phys. Rev.* 119 (1960), 980.

## Chapter IV

## THEORY OF NEUTRON SCATTERING

4.1. Introduction

A propagating neutron can be described as a particle wave for which the relation between wavelength and velocity is determined by its mass through the de Broglie relation  $\lambda = h/m_n v$ . The neutron mass has such a value that for thermal neutrons the wavelength is of the same order of magnitude as the interatomic distances in solids and liquids *i.e.* the neutron wave vector  $\underline{k} = 2\pi/\lambda$  is of about the same size as the wave vectors of the standing density waves in a crystal. Therefore, in analogy with X-ray diffraction, a neutron beam can be used for the study of crystalline structures by means of diffraction.

Since the neutron has an energy of the same order of magnitude as the excitation energies of lattice vibrations and molecular vibrations, it can also be applied for similar purposes as infra-red absorption and Raman scattering. The main reason why the neutron is such a powerful probe in the study of condensed material is found in the combination of the two properties. The scattering of a neutron in a crystal can be considered as the result of an interaction between the neutron wave and a density wave in the crystal. If such a density wave is a plane wave which represents the vibration of the lattice, both the exchange of energy and of momentum between the two waves can be observed in the same scattering process. Therefore, the relation between the two quantities, which is the dispersion relation, can be determined. In this respect neutron scattering is essentially different from all scattering techniques using electromagnetic radiation, as this has an entirely different relation between energy and wavelength. This is illustrated in Fig. 4.1 where for neutrons and electromagnetic radiation this relation has been given. From this figure it can be seen that the energy of X-rays used in structure determinations is higher than the excitation energies by about a factor  $10^5$  and as a consequence the excitations are unobservable by means of X-rays. Conversely, the wavelength of infra-red radiation is so long that the observation of momentum transfer is impossible. In addition to these two properties it is important that the intensity of

Section 4.1.

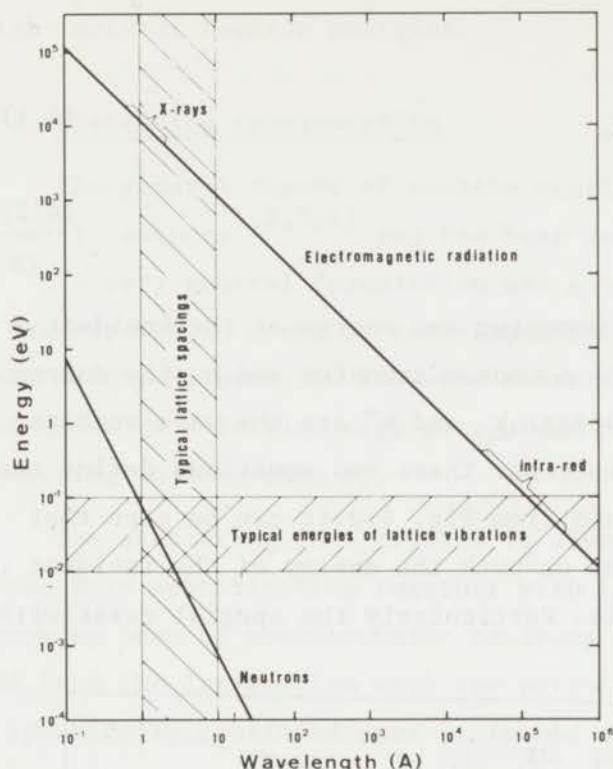


Fig. 4.1.

*Relation between energy and wavelength for electromagnetic radiation and thermal neutrons compared with the ranges of typical crystal-lattice spacings and excitation energies of lattice vibrations.*

energy and phase relations between the neutrons before and after scattering. The static structure of a solid gives rise to elastic scattering, while the dynamical behaviour causes inelastic scattering. Neutrons scattered by different atoms of a crystal will interfere coherently in the absence of irregularities such as differences in scattering lengths due to different isotopes or nuclear spins. In case such irregularities are present, part or all of the scattering will be incoherent. This investigation deals exclusively with coherent scattering since incoherent scattering provides no information about the momentum of the excitation.

scattering depends on atomic number in an entirely different way than for X-rays, because the scattering of neutrons is mainly by the nucleus, whereas X-rays are scattered by the electrons of an atom. Therefore, experiments on crystals composed of light and heavy atoms are often very well possible with neutrons.

The third characteristic property of the neutron is its magnetic moment, which offers the opportunity of studying both the static and dynamical magnetic structures of magnetic materials.

Neutron scattering processes can be distinguished according to

The neutron scattering processes are governed by the conservation laws for momentum and energy

$$\underline{Q} \equiv \underline{k}_0 - \underline{k}' = \underline{q} + 2\pi\underline{\tau} \quad (4.1)$$

$$h\nu = \frac{\hbar^2}{2m_n} (k_0^2 - k'^2) \quad (4.2)$$

Here  $\hbar k_0$  and  $\hbar^2/2m_n \cdot k_0^2$  are the momentum and energy of the incident neutrons, respectively;  $\hbar Q$  is the momentum transfer and  $h\nu$  the energy transfer during a scattering process;  $\underline{k}_0$  and  $\underline{k}'$  are the wave vectors of the incident and scattered neutrons. These two equations define the accessible region in  $\nu$ - $Q$  space and from Fig. 4.2 it can be seen that this region is strongly dependent on both the energy of the incident neutrons and the scattering angle. Particularly the special cases with

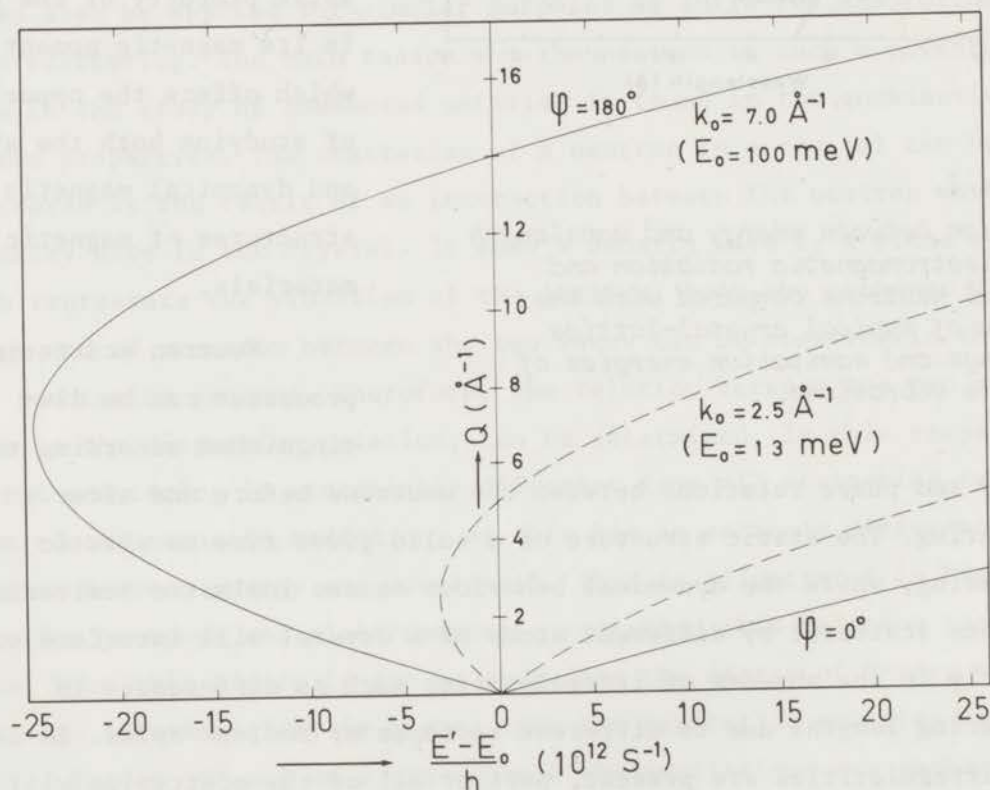


Fig. 4.2. Wave-vector transfer as a function of energy transfer for incident neutrons of wave vectors  $2.5 \text{ \AA}^{-1}$  (broken lines) and  $7.0 \text{ \AA}^{-1}$  (solid lines) and for scattering angle  $0^\circ$  and  $180^\circ$ .

Section 4.1.

large wave vector transfer and small  $v$  or small  $Q$  and large  $v$  require high incident neutron energies.

4.2. Scattering cross-section

The general theory of neutron scattering has been formulated by several authors<sup>1,2,3,4)</sup> and has been reviewed in a number of textbooks<sup>5,6)</sup>. A very general formulation was given by Van Hove<sup>7)</sup> who introduced a description in terms of time-dependent correlation functions. In this work mainly Nijboer and Kokkedee's treatment<sup>4)</sup> will be followed but the extension to a lattice with more atoms per primitive unit cell is more according to reference 6).

The scattering in a crystal is always treated according to the first Born approximation together with the Fermi pseudo-potential. An incoming beam of monochromatic neutrons is described as a plane wave and from the interaction with the potential of a fixed atomic nucleus a spherically scattered wave is formed such that at a long distance from the nucleus the total wave function can be expressed by

$$\psi = e^{i\mathbf{k}_0 \cdot \mathbf{z}} + \frac{f(\theta)}{r} \cdot e^{i\mathbf{k}' \cdot \mathbf{r}} \quad (4.3)$$

The differential cross-section per steradian for this interaction is  $\sigma(\theta) = f(\theta)^2$ . Since the wavelength of the neutron is very large compared with the range of interaction, the scattering amplitude  $f(\theta)$  is constant, equal to  $-b$  and consequently the total scattering cross-section is  $\sigma = 4\pi b^2$ . According to Born's approximation the scattering amplitude can be expressed as the Fourier transform of the scattering potential.

$$f(\theta) = -\frac{m_n}{2\pi\hbar^2} \int V(\mathbf{r}') \cdot e^{i(\mathbf{k}_0 - \mathbf{k}') \cdot \mathbf{r}'} d\mathbf{r}' \quad (4.4)$$

Fermi first suggested that this approximation can be applied very elegantly if the so-called pseudo-potential is used, a sum of delta-functions which is different from zero only at the positions of the nuclei.

$$V(\underline{r}, t) = \frac{2\pi\hbar^2}{m_n} \sum_l b_l \delta(\underline{r} - \underline{r}(l, t)) \quad (4.5)$$

Here  $\underline{r}(l, t)$  is the position vector of the  $l^{\text{th}}$  atom in the crystal at time  $t$ . Substitution in Eq. (4.4) for a single atom yields as before  $f(\theta) = -b$ . For an assembly of nuclei as in a crystal with more than one atom per primitive unit cell it leads to the time-dependent scattering operator  $F_Q = \sum_{l\kappa} b_{l\kappa} e^{i\mathbf{Q}\cdot\underline{r}(l\kappa, t)}$ . The double differential cross-section per unit cell  $l\kappa$  for a scattering process in which the crystal changes from state  $a$  into state  $b$  and the neutron energy changes from  $E_0$  to  $E'$  is expressed by

$$\frac{d^2\sigma}{d\Omega dE'} = \frac{1}{N_c} \frac{k'}{k_0} \sum_a p_a \sum_b |\langle b | F_Q | a \rangle|^2 \delta(E' - E_0 + E_b - E_a) \quad (4.6)$$

$\langle b | F_Q | a \rangle$  is the matrix element of the operator  $F_Q$  between the states  $a$  and  $b$ ; the square of this matrix element is the transition probability.  $E_a$  and  $E_b$  are the energies of the crystal states  $a$  and  $b$ , respectively, and  $p_a$  is the probability that the crystal is in the initial state  $a$ . Writing  $\underline{r}(l\kappa, t) = \underline{r}(l\kappa) + \underline{u}(l\kappa, t)$  where  $\underline{r}(l\kappa)$  is the position of atom  $\kappa$  in unit cell  $l$  and  $\underline{u}(l\kappa, t)$  its displacement at time  $t$ , the differential cross-section can be transformed and expressed in terms of correlations between displacements.

$$\begin{aligned} \frac{d^2\sigma}{d\Omega dE'} &= \frac{k'}{k_0} \sum_{l\kappa\kappa'} b_{l\kappa} b_{l\kappa'}^* e^{-(W_\kappa + W_{\kappa'})} \cdot e^{i\mathbf{Q}\cdot[\underline{r}(\kappa') - \underline{r}(\kappa)]} \cdot \sum_l e^{i\mathbf{Q}\cdot\underline{r}(l)} \times \\ &\times \frac{1}{2\pi\hbar} \int_{-\infty}^{+\infty} e^{i(\omega' - \omega_0)t} \cdot e^{\mathbf{Q}\cdot\underline{M}(l\kappa\kappa', t) \cdot \mathbf{Q}} dt \end{aligned} \quad (4.7)$$

Here  $W_\kappa = \frac{1}{2} \langle (\mathbf{Q}\cdot\underline{u}(l\kappa, 0))^2 \rangle_T$  is the exponent of the Debye-Waller factor for an atom of type  $\kappa$ ,  $\hbar(\omega' - \omega_0) = E' - E_0$  and the dyad

$$M(l\kappa\kappa', t) = \langle \underline{u}(0\kappa', 0) \underline{u}(l\kappa, t) \rangle_T \quad (4.8)$$

The brackets and the symbol  $T$  denote a statistical averaging at temperature  $T$ . In chapter II it has been shown that the displacements  $\underline{u}(l\kappa, t)$  can be regarded as a superposition of plane waves. Quantum-

Section 4.2.

mechanically these plane waves may be formulated in terms of the annihilation and creation operators  $a(\underline{qj})$  and  $a^*(\underline{qj})$ , respectively, for a harmonic oscillator

$$u(1\kappa, t) = \sum_{\underline{qj}} \left( \frac{\hbar}{2N_c \omega(\underline{qj})} \right)^{\frac{1}{2}} \cdot \frac{\xi(\kappa, \underline{qj})}{\sqrt{M_\kappa}} \left\{ a(\underline{qj}) e^{i[\underline{q} \cdot \underline{r}(1) - \omega(\underline{qj})t]} - a^*(\underline{qj}) e^{i[\underline{q} \cdot \underline{r}(1) + \omega(\underline{qj})t]} \right\} \quad (4.9)$$

Here  $N_c$  is the number of atoms in the crystal. The commutation relations for these operators are

$$[a(\underline{qj}), a(\underline{q'j'})] = [a^*(\underline{qj}), a^*(\underline{q'j'})] = 0 \text{ and } [a(\underline{qj}), a^*(\underline{q'j'})] = \delta_{\underline{q}\underline{q}'} \delta_{jj'}$$

It has been proved in 6) that by substitution of Eq. (4.9) into Eq. (4.8) and using the commutation relations  $M(1\kappa\kappa', t)$  takes the form

$$M(1\kappa\kappa', t) = \frac{\hbar}{4\pi N_c (M_\kappa M_{\kappa'})^{\frac{1}{2}}} \sum_{\underline{qj}} \frac{N+1}{v(\underline{qj})} e^{i\omega(\underline{qj})t} \cdot e^{-i\underline{q} \cdot \underline{r}(1)} \xi(\kappa, \underline{qj}) \xi^*(\kappa', \underline{qj}) + \frac{N}{v(\underline{qj})} e^{-i\omega(\underline{qj})t} \cdot e^{i\underline{q} \cdot \underline{r}(1)} \xi^*(\kappa, \underline{qj}) \xi(\kappa', \underline{qj}) \quad (4.10)$$

where  $N = \left( \exp \frac{h\nu(\underline{qj})}{k_B T} - 1 \right)^{-1}$ .

The first term in this expression corresponds to phonon creation and the second to phonon annihilation. Expanding  $\exp(\underline{Q} \cdot M(1\kappa\kappa', t) \cdot \underline{Q})$  in a power series, the so-called phonon expansion is obtained.

$$\begin{aligned} e^{\underline{Q} \cdot M(1\kappa\kappa', t) \cdot \underline{Q}} = & 1 + \frac{\hbar}{4\pi N_c (M_\kappa M_{\kappa'})^{\frac{1}{2}}} \sum_{\underline{qj}} \left\{ \frac{N+1}{v(\underline{qj})} e^{i\omega(\underline{qj})t} \cdot e^{-i\underline{q} \cdot \underline{r}(1)} \times \right. \\ & \times \left. \left( \underline{Q} \cdot \xi(\kappa, \underline{qj}) \right) \left( \underline{Q} \cdot \xi^*(\kappa', \underline{qj}) \right) + \frac{N}{v(\underline{qj})} e^{-i\omega(\underline{qj})t} \cdot e^{i\underline{q} \cdot \underline{r}(1)} \left( \underline{Q} \cdot \xi^*(\kappa, \underline{qj}) \right) \left( \underline{Q} \cdot \xi(\kappa', \underline{qj}) \right) \right\} \\ & + \dots \quad (4.11) \end{aligned}$$

Each successive term in this series is associated with a scattering process in which an increasing number of phonons is involved. For each of these terms the integration over  $t$  must be carried out in order to obtain the differential cross-section. Substituting the first and second terms of Eq. (4.11), respectively, into Eq. (4.7) the cross-sections for zero-phonon and single-phonon scattering are obtained. For zero-phonon or Bragg scattering it becomes

$$\begin{aligned} \frac{d^2\sigma^{(0)}}{d\Omega dE'} &= \frac{k'}{k_0} \sum_{\kappa\kappa'} b_{\kappa} b_{\kappa'}^* e^{-(W_{\kappa}+W_{\kappa'})} \cdot e^{i\mathbf{Q}\cdot[\mathbf{r}(\kappa')-\mathbf{r}(\kappa)]} \sum_1 e^{i\mathbf{Q}\cdot\mathbf{r}(1)} \times \\ &\times \frac{1}{2\pi\hbar} \int_{-\infty}^{+\infty} e^{i(\omega'-\omega_0)t} dt = \\ &= \frac{(2\pi)^3}{v_a} \left| \sum_{\kappa} b_{\kappa} e^{-W_{\kappa}} e^{-i\mathbf{Q}\cdot\mathbf{r}(\kappa)} \right|^2 \cdot \sum_{\underline{\tau}} \delta(\mathbf{Q}-2\pi\underline{\tau}) \delta(\omega'-\omega_0) \quad (4.12) \end{aligned}$$

where  $\underline{\tau}$  is a reciprocal lattice vector.

For single-phonon-creation scattering it is

$$\begin{aligned} \frac{d^2\sigma^{(1)cr.}}{d\Omega dE'} &= \frac{\hbar}{4\pi N_c} \frac{k'}{k_0} \sum_{\kappa\kappa'} \frac{b_{\kappa}}{\sqrt{M_{\kappa}}} \frac{b_{\kappa'}^*}{\sqrt{M_{\kappa'}}} e^{-(W_{\kappa}+W_{\kappa'})} \cdot e^{i\mathbf{Q}\cdot[\mathbf{r}(\kappa')-\mathbf{r}(\kappa)]} \sum_1 e^{i\mathbf{Q}\cdot\mathbf{r}(1)} \times \\ &\times \frac{1}{2\pi\hbar} \int_{-\infty}^{+\infty} dt e^{i(\omega'-\omega_0)t} \sum_{\underline{qj}} \frac{N+1}{v(\underline{qj})} e^{i\omega(\underline{qj})t} e^{-i\mathbf{q}\cdot\mathbf{r}(1)} (Q_{\underline{\xi}}(\kappa,\underline{qj})) (Q_{\underline{\xi}^*}(\kappa',\underline{qj})) \\ &= \frac{1}{4\pi} \frac{k'}{k_0} \int \frac{N+1}{v(\underline{qj})} \left| \sum_{\kappa} \frac{b_{\kappa}}{\sqrt{M_{\kappa}}} e^{-W_{\kappa}} Q_{\underline{\xi}}(\kappa,\underline{qj}) e^{-i\mathbf{Q}\cdot\mathbf{r}(\kappa)} \right|^2 \times \\ &\times \sum_{\underline{\tau}} \delta(\mathbf{Q}-\underline{q}-2\pi\underline{\tau}) \cdot \delta(\omega'-\omega_0+\omega(\underline{qj})) d\underline{q} \quad (4.13) \end{aligned}$$

and similarly the expression for single-phonon-annihilation scattering is

Section 4.2.

$$\frac{d^2\sigma^{(1)an.}}{d\Omega dE'} = \frac{1}{4\pi} \frac{k'}{k_0} \int \frac{N}{v(\underline{qj})} \left| \sum_{\kappa} \frac{b_{\kappa}}{\sqrt{M_{\kappa}}} e^{-i\mathbf{W}_{\kappa} \cdot \underline{Q} \cdot \underline{\xi}(\kappa, \underline{qj})} e^{i\mathbf{Q} \cdot \underline{r}(\kappa)} \right|^2 \times$$

$$\times \sum_{\underline{\tau}} \delta(\underline{Q} + \underline{q} - 2\pi\underline{\tau}) \cdot \delta(\omega' - \omega_0 - \omega(\underline{qj})) d\underline{q} \quad (4.14)$$

In (4.13) and (4.14) the summation over  $\underline{qj}$  has been replaced by integration over the first Brillouin zone, which introduces the factor  $N_c v_a / (2\pi)^3$  which is the density of states. The summation over  $\kappa$  is over all atoms in the primitive unit cell.

The differential cross-section for a phonon peak can be obtained by integration over  $E'$ . However, since there is a correlation between the two delta-functions, a transformation is required which was first carried out by Waller and Fröman<sup>8)</sup>. The single-phonon-creation cross-section per steradian per unit cell for the  $j^{\text{th}}$  branch can then be expressed by

$$\frac{d\sigma^{(1)cr.}(\underline{qj})}{d\Omega} = \frac{1}{4\pi} \frac{k'}{k_0} \frac{N+1}{v(\underline{qj})} \left| \sum_{\kappa} \frac{b_{\kappa}}{\sqrt{M_{\kappa}}} e^{-i\mathbf{W}_{\kappa} \cdot \underline{Q} \cdot \underline{\xi}(\kappa, \underline{qj})} e^{-i\mathbf{Q} \cdot \underline{r}(\kappa)} \right|^2 \cdot \frac{1}{J} \quad (4.15)$$

with  $J = 1 + \frac{\hbar}{2E} \underline{k}' \cdot \underline{\text{grad}} v(\underline{qj})$

Eq. (4.15) can also be written as

$$\frac{d\sigma^{(1)cr.}(\underline{qj})}{d\Omega} = \frac{1}{4\pi} \frac{k'}{k_0} \frac{N+1}{v(\underline{qj})} g^2(\underline{\tau}, \underline{qj}) \cdot \frac{1}{J} \quad (4.16)$$

Here the quantity

$$g^2(\underline{\tau}, \underline{qj}) = \left| \sum_{\kappa} \frac{b_{\kappa}}{\sqrt{M_{\kappa}}} e^{-i\mathbf{W}_{\kappa} \cdot \underline{Q} \cdot \underline{\xi}(\kappa, \underline{qj})} e^{-i\mathbf{Q} \cdot \underline{r}(\kappa)} \right|^2 \quad (4.17)$$

is the inelastic structure factor, which is the inelastic equivalent of the familiar structure factor in elastic scattering. From Eq. (4.17) it is seen that the inelastic structure factor depends on  $\underline{q}$  and on  $\underline{\tau}$  and, therefore, it does not have the periodicity of  $\underline{q}$ . Brockhouse and Iyengar<sup>9)</sup> pointed out that if a reduced inelastic structure factor is defined as

$$g^2(\underline{r}, \underline{qj})_{\text{red.}} = \frac{\left| \sum_{\kappa} \frac{b_{\kappa}}{\sqrt{M_{\kappa}}} e^{-W_{\kappa}} \underline{Q} \cdot \underline{\xi}(\kappa, \underline{qj}) e^{-i\underline{Q} \cdot \underline{r}(\kappa)} \right|^2}{\sum_{\kappa} \left| \frac{b_{\kappa}}{\sqrt{M_{\kappa}}} e^{-W_{\kappa}} \underline{Q} \cdot \underline{\xi}(\kappa, \underline{qj}) \right|^2} \quad (4.18)$$

this will be a periodic function in reciprocal space for those directions where the polarization vectors  $\underline{\xi}(\kappa, \underline{qj})$  for different  $\kappa$  are all parallel. These vectors can then be written as  $\xi(\kappa, \underline{qj}) \underline{x} \underline{\xi}(\underline{qj})$  where  $\underline{\xi}(\underline{qj})$  is a unit vector. Hence (4.18) is then

$$g^2(\underline{r}, \underline{qj})_{\text{red.}} = \frac{\left| \sum_{\kappa} \frac{b_{\kappa}}{\sqrt{M_{\kappa}}} e^{-W_{\kappa}} \xi(\kappa, \underline{qj}) e^{-i(2\pi\underline{r} + \underline{q}) \cdot \underline{r}(\kappa)} \right|^2}{\sum_{\kappa} \left| \frac{b_{\kappa}}{\sqrt{M_{\kappa}}} e^{-W_{\kappa}} \xi(\kappa, \underline{qj}) \right|^2} \quad (4.19)$$

This function is periodic in reciprocal space. Since this periodicity is limited to those special directions only, the repetition unit for the reduced inelastic structure factor has a different meaning as that of the extended Brillouin zone scheme.

In chapter VI it will be demonstrated that for branches where only polarization vectors of atoms, connected by a centre of symmetry contribute, the reduced inelastic structure factor is constant within a repetition unit. In some of these units it may be equal to zero.

References

- 1) R. Weinstock, Phys. Rev. 65 (1944), 1.
- 2) J.M. Cassels, Progr. Nucl. Phys. 1 (1950), 185.
- 3) A. Sjölander, Ark. Fys. 14 (1958), 315.
- 4) B.R.A. Nijboer, J.J.J. Kokkedee, AERE-Trans 1004 (1964).
- 5) P.A. Egelstaff, Thermal Neutron Scattering, London and New York, Academic Press, 1965.
- 6) I.I. Gurevich, L.V. Tarasov, Low-Energy Neutron Physics, Amsterdam, North-Holland Publishing Comp. 1968.
- 7) L. van Hove, Phys. Rev. 95 (1954), 249.
- 8) I. Waller, P.O. Fröman, Ark. Fys. 4 (1952), 183, 191.
- 9) B.N. Brockhouse, P.K. Iyengar, Phys. Rev. 111 (1958), 747.

Chapter V

EXPERIMENTAL

5.1. Introduction

In the field of neutron spectroscopy the triple-axis crystal spectrometer has found a wide application for INS experiments on single crystals. It was first used by Brockhouse<sup>1)</sup> who developed the experimental technique and demonstrated its powerful properties. Compared with experimental INS methods using time-of-flight techniques, the triple-axis crystal spectrometer is rather wasteful with the neutrons, but this is compensated for since it produces the information which is required. Recently, however, time-of-flight techniques have been strongly developed particularly in connection with pulsed reactors.

In all INS experiments observing excitations in single crystals the lengths and directions of the incident and scattered neutron wave vectors must be defined. In the triple-axis spectrometer this is done by two crystal spectrometers. The neutron paths through the spectrometer have been sketched in Fig. 5.1. From thermal neutrons, extracted

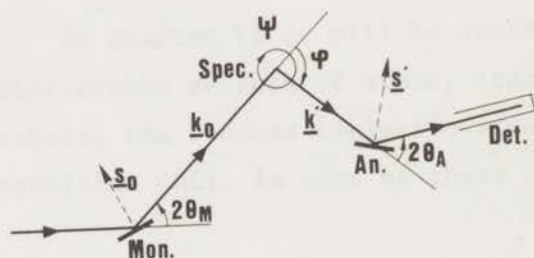


Fig. 5.1. Schematic diagram of a triple-axis crystal spectrometer.

from a reactor, a monochromator crystal selects a mono-energetic beam, which impinges upon a specimen. The energy of these neutrons is determined by Bragg's law and depends on the angle of reflection  $\theta_M$  and on the spacing  $d_M$  of the reflection planes. The neutrons, scattered by the specimen through a variable angle  $\phi$ , are then

analyzed by a second monochromator and finally they are detected in a  $\text{BF}_3$  counter. The direction of the incident neutrons relative to the specimen axes can be varied by the setting angle  $\psi$ .

5.2. Description of the spectrometer

The triple-axis crystal spectrometer has been installed in front of one of the radial beamholes of the Petten High Flux Reactor. Its

*Section 5.2.*

major components are the in-pile section consisting of a collimator plug and a beam shutter, the monochromator unit with the movable platform, the specimen spectrometer and the analyzer with the detector arm. The arrangement of these components is illustrated by the photograph of the instrument in Fig. 5.2 and by Fig. 5.3.

The in-pile collimator is a plug with a 9 cm diameter evacuated channel. In this plug an additional collimating cylinder of aluminium, 75 cm long, has been inserted having an inner diameter tapering from 6.4 to 5.6 cm. The shutter is a 50 cm long cylinder rotating around an axis parallel to the neutron beam and consisting of alternating layers of iron and pertinax; it has an excentric hole of 7.2 cm diameter. The transition from the in-pile section to the outside equipment is realized by a 25 cm thick cast iron baffle shield. The space between this baffle shield and the monochromator shield has been filled with heavy concrete blocks. At the level of the beam there is a cavity, which provides the possibility to insert the first Soller slit collimator. It can be brought into position through an opening from the top and can be adjusted through a plug, which fits this opening. The monochromator unit consists of a base frame carrying both the rotating shielding drum and a halfangling cylinder. A gear-wheel system between these components provides a 2:1 gearing ratio. The shielding drum contains a central hole of 36 cm, shielded by 15 cm iron, 30 cm paraffin wax and 10 cm lead. Inside this shielding the halfangling cylinder goes to the top where it carries the monochromator plug, which can be rotated around a vertical axis. From the monochromator plug consisting of iron, pertinax and lead a ring has been suspended in which the monochromator crystal can be mounted and which can be rotated around a horizontal axis. By means of adjusting screws the axes of the halfangling cylinder and the monochromator plug can be made to coincide. Openings in the shielding and in the halfangling cylinder allow the neutron beams to pass through. In order to avoid leakage of radiation a movable piece of shielding partially fills the open wedge in the drum at one side or the other depending on the value of  $2\theta_M$ .

The spectrometer platform is rigidly connected to the shielding

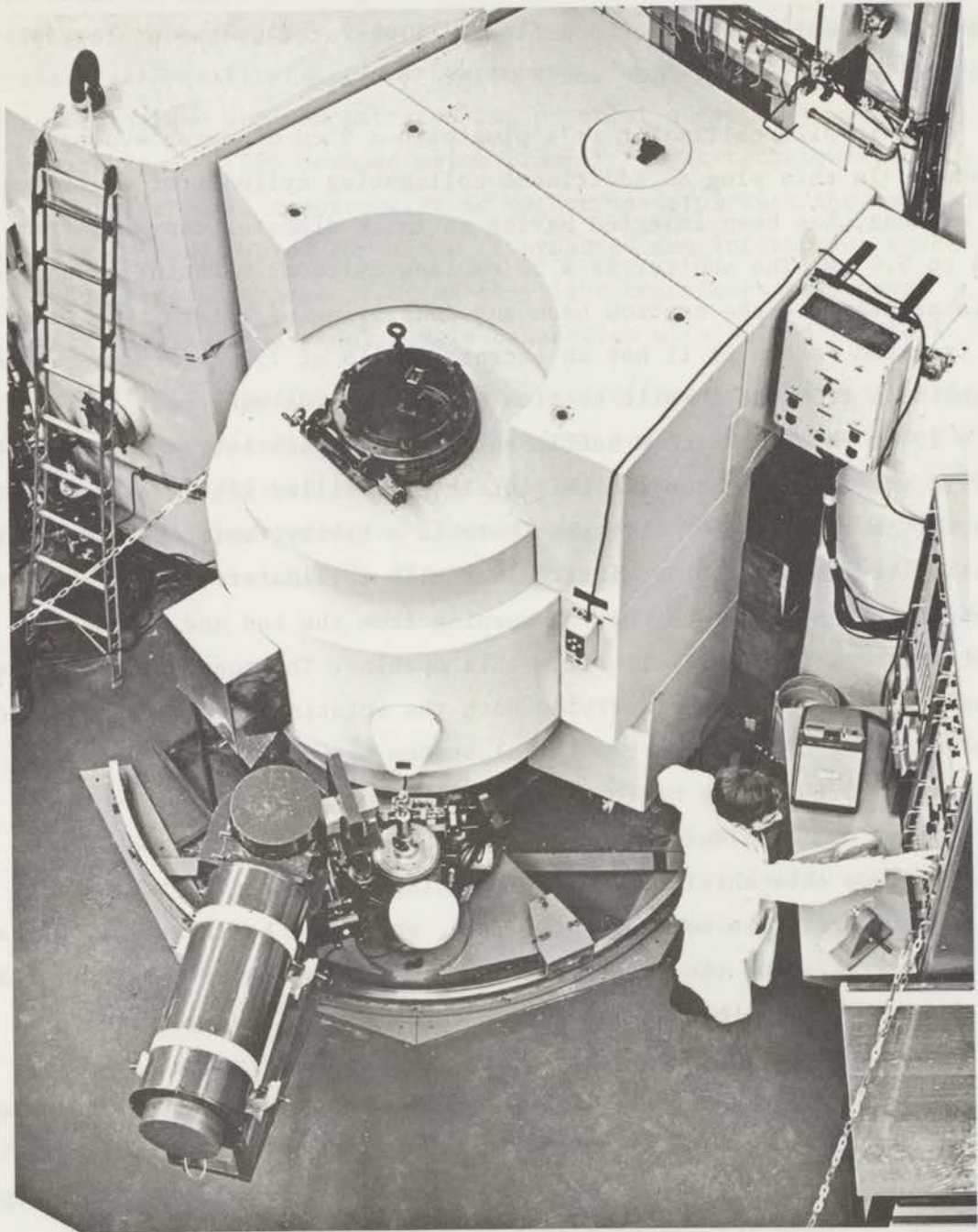


*Fig. 5.2. Photograph of the triple-axis crystal spectrometer.*

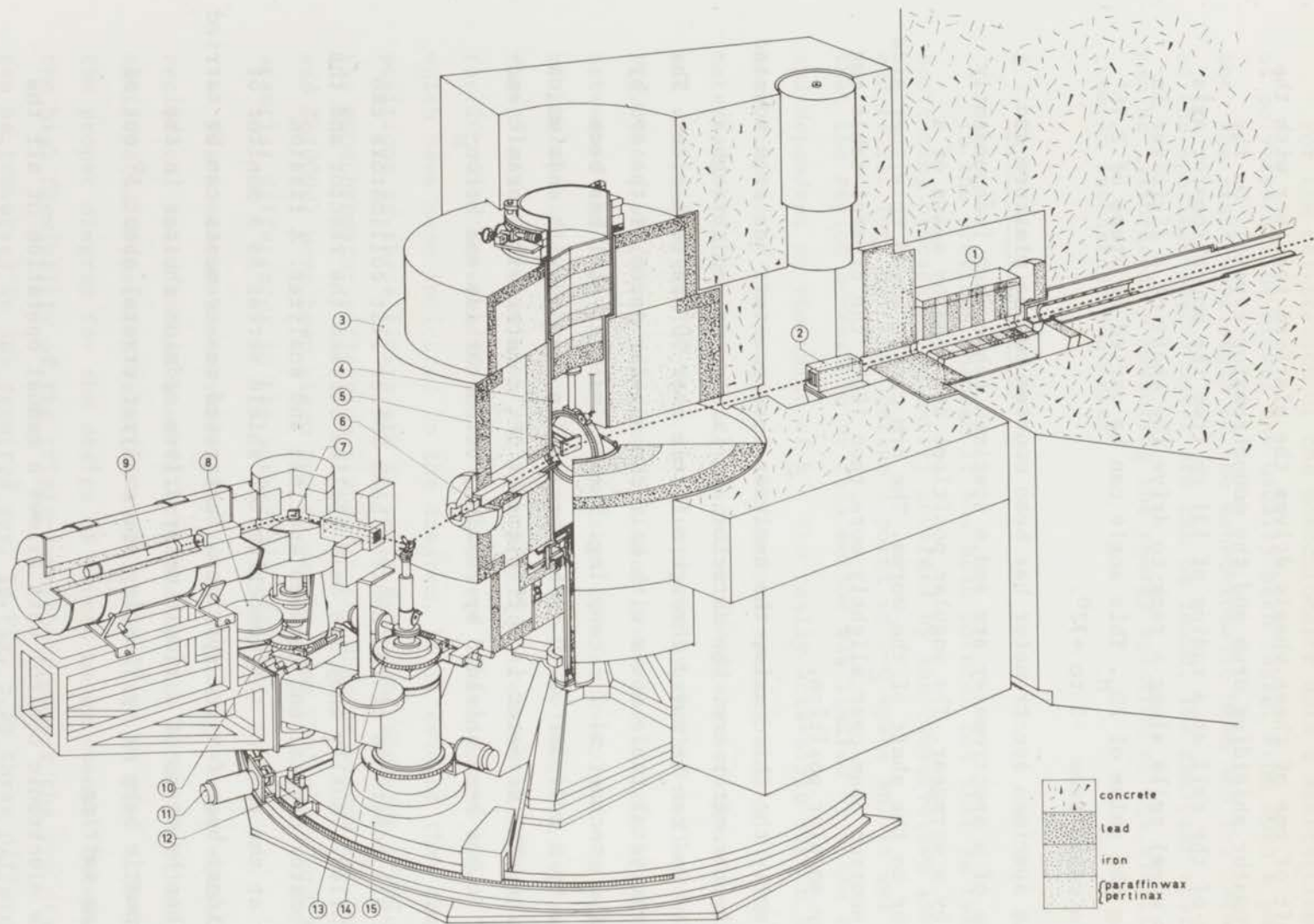


Fig. 5.3. View of the triple-axis spectrometer; 1: beam shutter, 2: Soller slit collimator, 3: rotating monochromator shield, 4: half-angling cylinder, 5: monochromator crystal, 6: monitor counter, 7: analyzer crystal, 8: analyzer half-angling gear box, 9: neutron counter, 10: gear for  $2\theta_A$ -motion, 11: driving motor  $2\theta_A$ , 12: digitizer, 13: gear for  $\psi$ -motion, 14: gear for  $\phi$ -motion, 15: platform.

drum and moves on two wheels over a circular rail. A motor mounted on the shaft of one of these wheels drives the platform together with the monochromator shielding drum and the monochromator crystal. On the outside of the rail at a radius of 131 cm from the monochromator axis a tooth wheel rolls along a rack to drive the shaft of a digitizer indicating the value of  $2\theta_M$ . This angle can be varied in steps of  $2.16'$  within a range from  $-5$  to  $+77^\circ$ .

The specimen spectrometer has been mounted on the platform and consists of a spectrometer arm and a specimen table each independently driven by a wormgear. The angular positions are read by means of a digitizer on the shaft of the worms. The arm can be moved to either side of the neutron beam over slightly more than  $100^\circ$ ; the crystal table can take any angular position.

Finally the third axis, the analyzer spectrometer, has been mounted on the spectrometer arm. The detector arm is also driven through a wormgear and can be moved through a little over  $90^\circ$  on both sides. The analyzer-crystal table moves with half the angular speed of the arm by means of a mechanical 2:1 coupling. The analyzer crystal has been shielded by a cylinder of 10 cm boron-paraffin clad with cadmium on the inside. The detector is a 2" diameter  $\text{BF}_3$  counter with ceramic end-window. It has been shielded by cadmium, boron carbide and boron-paraffin.

At all positions of the neutron beam Soller slit collimators can be installed. Usually they are only applied between the reactor and the monochromator crystal and between specimen and analyzer. A fission counter at the exit of the monochromator shield serves as a monitor of the incident beam for the specimen. Background measurements can be carried out either by means of a simple motor-driven cadmium shutter in the monochromatic beam or by flipping the analyzer crystal about  $5^\circ$  out of its Bragg setting.

The electronic control unit allows a manual operation of all the variable angles, experiments with automatic stepwise variation of one of the angles, or fully programmed experiments where operational instructions are read from punched tape.

Section 5.2.

For the calibration of the monochromator unit a diffraction pattern of polycrystalline nickel has usually been taken. From such a pattern both the exact wavelength of the monochromatic beam and the zero position of the specimen-spectrometer arm can be found. The analyzer spectrometer can be calibrated by measuring the energy spectrum of the elastic peak from an incoherent scatterer.

5.3. Experimental methods

In the previous chapter it has been pointed out that an inelastic scattering process is primarily governed by the conservation laws (4.1) and (4.2). Together they define a point in  $\nu$ - $Q$  space and it was indicated that the region accessible by this method was limited by these relations and dependent on the value of  $k'$ . The really accessible region is still more limited by the ranges of the various setting angles of the spectrometer and by the spacings of the reflection planes of the monochromator and analyzer crystals. This is illustrated by the  $k$ - $Q$ - $\nu$  diagram in Fig. 5.4., where  $\nu$ - $Q$  diagrams have been given for various  $k'$  values between 0 and  $7 \text{ \AA}^{-1}$ . It has been taken into account that the angle  $\phi$  of the spectrometer arm can be varied from 0 to  $100^\circ$ . The two surfaces for  $0^\circ$  and  $100^\circ$  meet at  $k' = 0$ . For practical reasons the range accessible for  $2\theta_M$  lies between 20 and  $77^\circ$ . This sets limits on the range of  $\nu$ , which have been indicated in the diagram. It is evident that the positions of these limits are strongly dependent upon the  $d$ -value of the monochromator reflection plane. In the diagram values for Cu(111) and Zn(0002) have been given and it can be seen that there are substantial differences in the accessible regions.

The momentum conservation law (4.1) defines a vector equation in reciprocal space as has been illustrated in Fig. 5.5a. Together with an anticipated dispersion relation as has been drawn in Fig. 5.5b it is the proper diagram for the design of phonon measurements. Because of the high flexibility of the triple-axis spectrometer the  $\nu$ - $q$  diagram can be traversed in any required way. In Fig. 5.5b three different modes have been indicated. I is the so-called "constant- $Q$ " mode of operation, in which  $q$  and consequently also  $Q$  is kept constant and  $\nu$  is varied in equal increments. From Fig. 5.5a it is seen that, when  $k'$  is kept constant

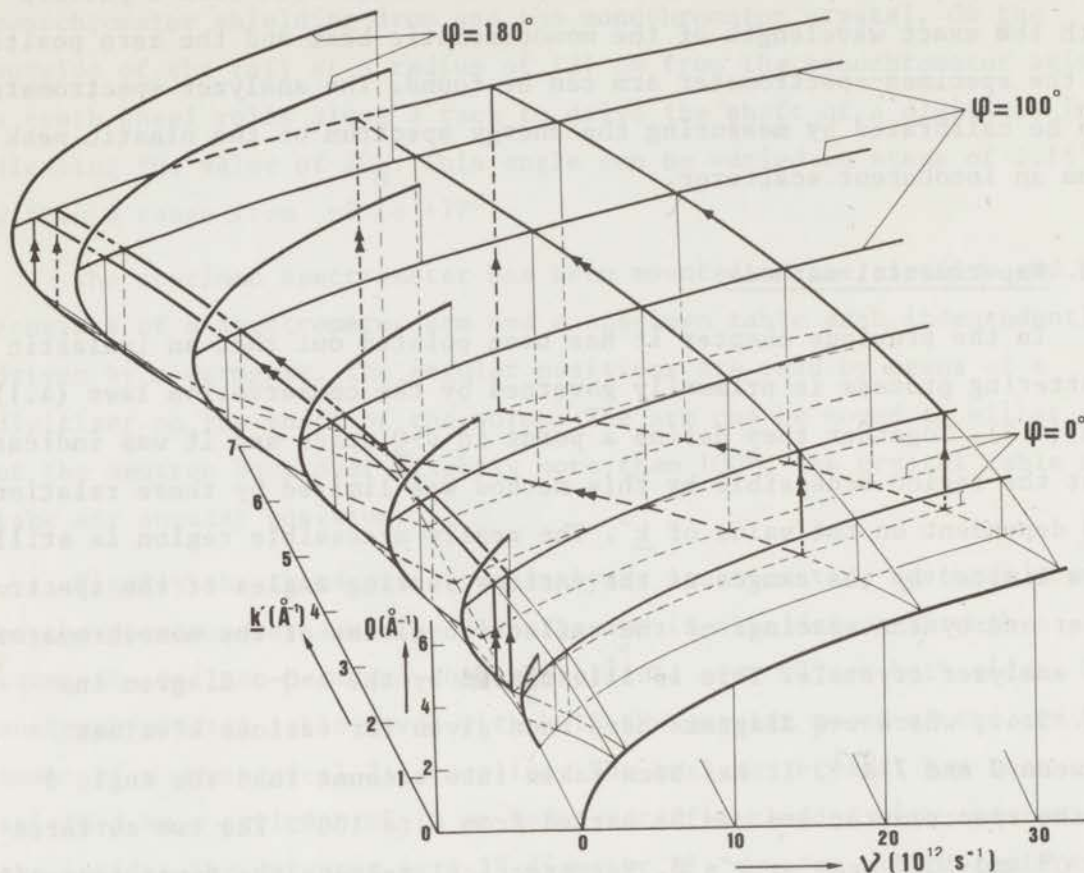


Fig. 5.4.  $k$ - $Q$ - $v$  diagram which shows the wave-vector transfer  $Q$  as a function of the energy transfer  $h\nu$  for neutrons with  $k$  between 0 and  $7 \text{ \AA}^{-1}$ . The limitations on the ranges of  $\phi$  and  $2\theta_M$  determine the experimentally accessible regions in the diagram. These regions have been indicated for two monochromator reflections; the line with single arrow for  $\text{Cu}(111)$  and the line with double arrow for  $\text{Zn}(0002)$ . The heavy lines for  $180^\circ$  scattering have been drawn for negative  $v$ -values only.

so that P moves along a circle around R, this means that  $2\theta_M$ ,  $\phi$ , and  $\psi$  vary from point to point. It should be noted that this mode of operation allows still one instrumental degree of freedom. Alternatively,  $k_0$  may be kept constant instead of  $k^-$ . Operation II is the "constant energy" mode, which has special advantage if the dispersion relation is very steep. Here both  $k_0$  and  $k^-$  are kept constant and only  $\phi$  and  $\psi$  are varied. In the third mode of operation called "normal to the gradient" neither

Section 5.3.

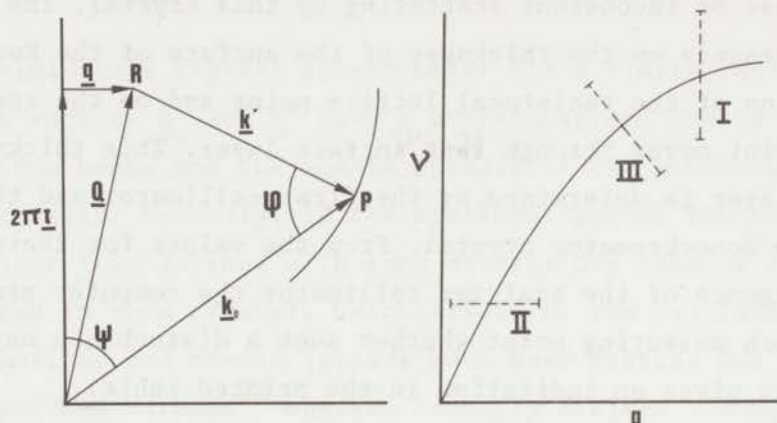


Fig. 5.5. a Vector diagram of the momentum conservation law.

- b Dispersion relation to be measured by INS. The trajectories for three modes of operation have been indicated; I: constant- $Q$ , II: constant energy, III: normal to the gradient.

$q$  nor  $v$  is kept constant, but the  $v$ - $q$  diagram is traversed perpendicular to the local gradient of the dispersion relation. This mode may be of value for the observation of line widths of phonons. In the experiments described in this investigation only modes I and II have been applied. Having defined an experiment in the diagrams of Fig. 5.5a and b according to one of the three modes it was transformed into terms of instrumental parameters by means of a computer programme. This programme produces a punched tape with all spectrometer settings for each measuring point. In addition it gives a printed table with both the spectrometer angles and the values of all relevant quantities occurring in the diagrams of fig. 5.5a and b.

During the course of the experiment it may happen that the Ewald sphere associated with the vector  $\mathbf{k}_0$  hits a reciprocal lattice point. This causes elastic scattering of the incident neutrons, which then propagate through the specimen crystal in an entirely different direction. In practice it has been found that this parasitic Bragg scattering will particularly interfere with the experiment if the position of that reciprocal lattice point is such that the incident neutrons are scattered elastically in the direction of  $\mathbf{k}'$  and consequently hit the analyzer

crystal. This will then give a strong intensity in the detector due to thermal diffuse or incoherent scattering by this crystal. The width of such a peak depends on the thickness of the surface of the Ewald sphere at the position of the reciprocal lattice point and on the speed at which this point moves through that surface layer. This thickness of the surface layer is determined by the first collimator and the mosaic spread of the monochromator crystal. From the values for these quantities and the divergence of the analyzer collimator the computer programme checks for each measuring point whether such a disturbance may occur and, if so, it gives an indication in the printed table.

The accidental incident beam may also lead to the observation of a phonon, which has the same  $\underline{q}$  as the one the original beam was planned for, because of the symmetry of the lattice. It is unlikely that the two phonons are identical, since in general the configuration of  $\underline{Q}$  and the polarization vector is different in the two cases. If a phonon is observed, it will, therefore, most probably belong to a different branch.

The instruction tape may contain information concerning monitor setting, background measurements by means of either the analyzer flipper of the cadmium shutter and further details about the conditions of the experiment. After each measuring point all angular settings, the monitor scaler and the detector scaler are read out and their values punched together with the measuring time and some further details concerning the particular experiment. Heading a series of such observations are a number of data specifying the particular experiment, copied from the instruction tape. The information contained in the output tape allows a reduction of the data to a diagram of the intensity versus frequency or versus wave vector. This reduction is carried out by means of a second computer programme, which provides a table of the reduced data and in addition plots the diagram on a line printer.

#### 5.4. Resolution and focusing

The phonon lines observed by inelastic scattering of neutrons will be broadened by the resolution function of the spectrometer. Apart from this resolution function the width of an observed line is strongly determined by the way  $\nu$ - $\underline{Q}$  space is traversed during an experiment.

Section 5.4.

Finding the conditions to optimize this is generally described as focusing.

The triple-axis crystal spectrometer has a finite resolution first because the vectors  $\underline{k}_0$  and  $\underline{k}'$  have a certain spread due to the divergences in the neutron beams and the mosaic spreads of the monochromator and analyzer crystals. Secondly, in the specimen crystal the reciprocal lattice vector  $\underline{\tau}$  is defined with some uncertainty because of the mosaic spread in this crystal. Calculations of the resolution function from collimations and mosaic spreads have been carried out by Collins<sup>2)</sup> and by Cooper and Nathans<sup>3)</sup> whereas recently Nielsen and Bjerrum Møller<sup>4)</sup> determined the resolution function by experiment and calculation without prior knowledge of collimations and mosaic spreads. The last mentioned authors pointed out that for Bragg scattering in the specimen the resolution function can be determined with great accuracy from the experiment. The intensity of a phonon line is a convolution of the resolution function and the natural line shape. For Bragg scattering the latter is a product of the two delta functions  $\delta(\underline{q})$  and  $\delta(\nu)$  so that the observed Bragg peaks provide the resolution function in a direct way.

Such measurements have been carried out on the (220) reflection of a germanium crystal for which the spread in  $\underline{\tau}$  may be neglected. Constant energy scans were made for a number of values of the energy transfer with both  $\underline{q}$  parallel with and perpendicular to  $\underline{Q}$ . The applied collimations in front of the monochromator and analyzer crystals were 20°/30° and 40°/60°. In Figures 5.6 and 5.7 the results have been given for two different neutron energies as contour lines in a  $\nu$ - $Q$  diagram which connect points at which the intensity has dropped to half of the maximum value. They demonstrate the strong correlation existing between  $\underline{q}$  and  $\nu$ , in particular for  $\underline{q}$  perpendicular to  $\underline{Q}$ . Since in the measurement of a phonon line the incident and scattered neutrons are not of equal energies, these ellipsoids do not provide the exact line widths to be expected. However, it is clear that the line width is strongly dependent on the relative orientation in  $\nu$ - $Q$  space of this ellipsoid and the dispersion curve at the point where it is traversed, the minimum being obtained of the main axis is parallel to it. This emphasizes the

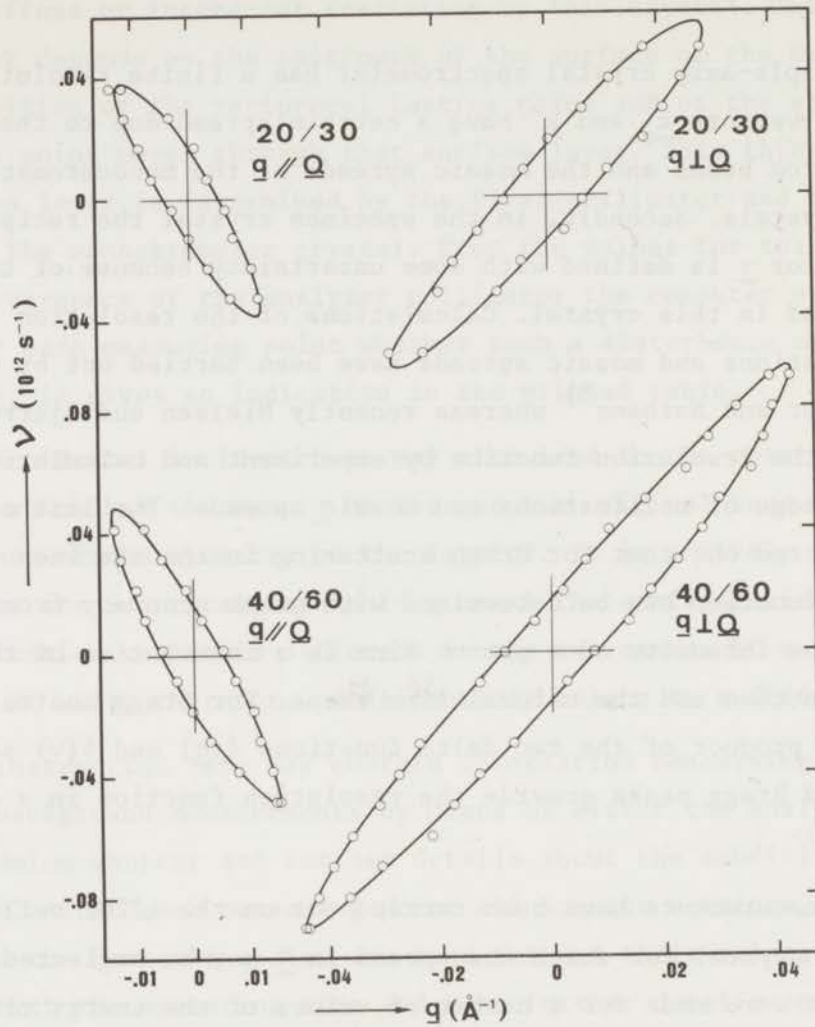


Fig. 5.6. Resolution ellipsoids at the (220) reflection of germanium with neutron energy of 12.5 meV. The figure shows patterns for  $q//Q$  and for  $q\perp Q$ ; the collimations before monochromator and analyzer have been given in minutes of arc.

importance of applying focusing and finding the optimum experimental conditions.

The effect of focusing has been treated analytically by Collins<sup>2)</sup> and by Cooper and Nathans<sup>3)</sup> whereas graphical methods were given by Bergsma and Van Dijk<sup>5)</sup> and by Peckham *et al.*<sup>6)</sup>. In the present investigations the graphical method has been applied for finding focusing conditions whenever that was possible.

Section 5.4.

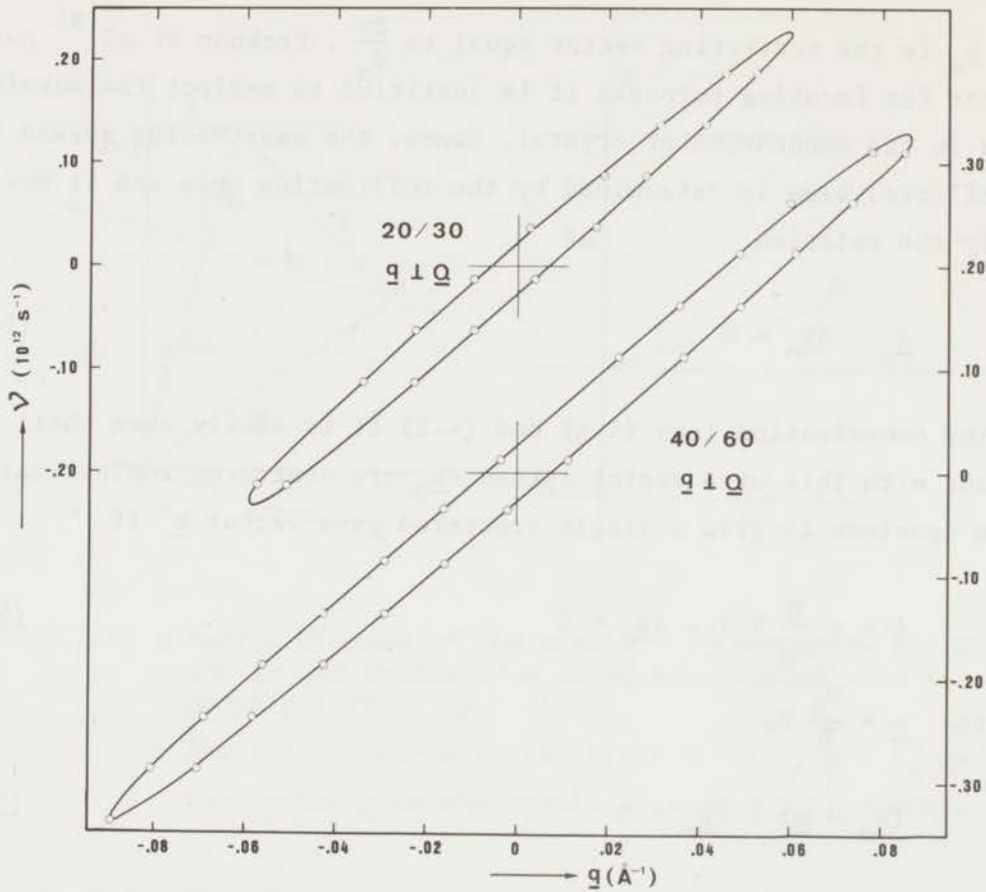


Fig. 5.7. Resolution ellipsoids at the (220) reflection of germanium with neutron energy of 34 meV. The figure shows patterns for  $q \perp Q$ ; the collimations before monochromator and analyzer have been given in minutes of arc.

As regards the monochromator section of a triple-axis spectrometer focusing conditions in a phonon measurement are obtained if the wave-vector spread in the monochromatic beam is such that the inelastic scattering of a maximum number of incident neutrons leads to the same scattered neutron wave vector. Conversely, the focusing of the analyzer implies that a maximum number of scattered neutrons arising from one incident wave vector is acceptable for reflection by the analyzer crystal. For the monochromator the condition for Bragg scattering may be written as

$$\underline{k}_0 \cdot \underline{s}_0 = \frac{1}{2} s_0^2 = \text{constant} \quad (5.1)$$

where  $\underline{s}_0$  is the scattering vector equal to  $\frac{2\pi}{d_M}$ . Peckham *et al.*<sup>6)</sup> pointed out that for focusing purposes it is justified to neglect the mosaic spread in the monochromator crystal. Hence, the wave vector spread in the reflected beam is determined by the collimation only and it must satisfy the relation

$$\underline{s}_0 \cdot \delta \underline{k}_0 = 0 \quad (5.2)$$

From the conservation laws (4.1) and (4.2) it is easily seen that neutrons with this wave vector spread  $\delta \underline{k}_0$  are scattered inelastically by the specimen to give a single scattered wave vector  $\underline{k}'$  if

$$(\nabla \omega - \frac{\hbar}{m_n} \underline{k}_0) \cdot \delta \underline{k}_0 = 0 \quad (5.3)$$

or with  $\underline{m} = \frac{m_n}{\hbar} \nabla \omega$

$$(\underline{k}_0 - \underline{m}) \cdot \delta \underline{k}_0 = 0 \quad (5.4)$$

Here  $\nabla \omega$  represents the group velocity of the phonon. From Eqs. (5.2) and (5.4) it is obvious that the focusing condition for the monochromator implies that  $\underline{k}_0 - \underline{m}$  should be either parallel or antiparallel with  $\underline{s}_0$ . In the same way it is found that focusing of the analyzer requires  $\underline{k}' - \underline{m}$  to be parallel or antiparallel with  $\underline{s}_1$ , the scattering vector of the analyzer reflection plane. From these considerations it is evident that the vector  $\underline{m}$ , the gradient of the dispersion relation, is of crucial importance for the possibility of applying focusing. From Fig. 5.8a, which again shows the momentum conservation law, it is obvious that in a phonon measurement with given values for  $\omega$  and  $\underline{Q}$  the point P may be moved freely along a line perpendicular to  $\underline{Q}$ , since this line is the locus of points where  $k_0^2 - k'^2$  is constant.

Adopting a new coordinate system with the X-axis along  $\underline{Q}$  and the Y-axis parallel with the line representing the locus of points P, the two conservation laws can be written as

Section 5.4.

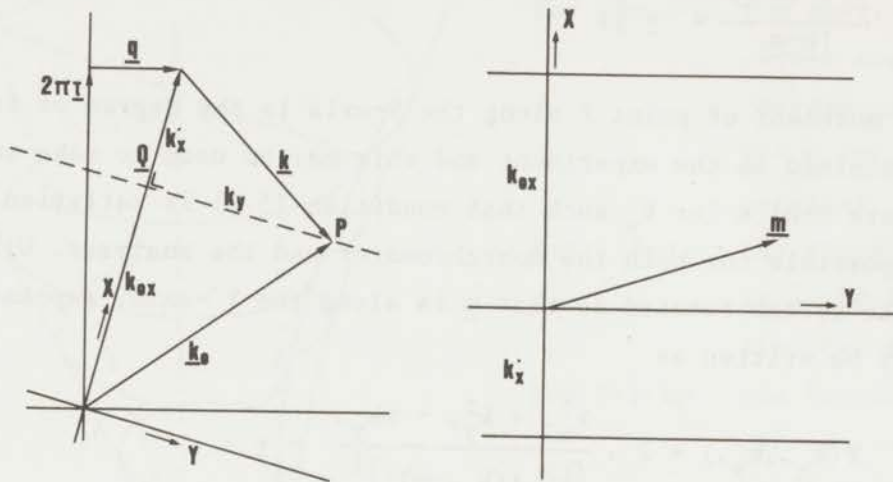


Fig. 5.8. a Vector diagram of the momentum conservation law with the X- and Y-axes of a coordinate system used in graphical focusing.

b The X-Y diagram with the lines  $x = k_{ox}$ ,  $x = k'_x$  and the vector  $\underline{m}$  in the graphical method of focusing.

$$k_{ox} - k'_x = Q \quad (5.5)$$

$$k_o^2 - k'^2 = k_{ox}^2 - k_x'^2 = \frac{2m_n}{\hbar} \omega \quad (5.6)$$

The Y-components of the neutron wave vectors have been eliminated and the X-components can easily be calculated.

$$k_{ox} = \frac{m_n \omega}{\hbar Q} + \frac{1}{2}Q \quad (5.7)$$

$$k'_x = \frac{m_n \omega}{\hbar Q} - \frac{1}{2}Q$$

In Fig. 5.8b the lines  $x = k_{ox}$  and  $x = k'_x$  have been drawn together with the vector  $\underline{m}$  of the phonon.

From the Bragg condition, written as  $(\underline{k} \cdot \underline{s})/|\underline{s}| = \frac{1}{2}s$ , and the fact that  $\underline{k} - \underline{m}$  and  $\underline{s}$  should be parallel or antiparallel the focusing

condition can be expressed by

$$\frac{\underline{k} \cdot (\underline{k}-\underline{m})}{|\underline{k}-\underline{m}|} = \pm \frac{1}{2}s \quad (5.8)$$

The free movement of point P along the Y-axis is the degree of freedom still contained in the experiment and this may be used to make an appropriate choice for  $k_y$  such that condition (5.8) is satisfied as well as possible for both the monochromator and the analyzer. With the coordinate system rotated so that  $\underline{m}$  is along the Y'-axis, expression (5.8) may be written as

$$F(k_{x'}, k_{y'}) = 2 \cdot \frac{k_{x'}^2 + k_{y'}^2 - mk_{y'}}{[k_{x'}^2 + (k_{y'} - m)^2]^{\frac{1}{2}}} = \pm s \quad (5.9)$$

where the prime indicates that the values are taken in the new coordinate system. This is a function symmetric in  $k_{x'}$  and discontinuous in  $k_{y'}$  at the point (0,m). A display of the function has been sketched in Fig. 5.9. Only discrete values for the spacings of reflection planes are available and consequently only cross-sections through this function by the planes  $z = \pm s$  are of real interest. For a particular value of m a set of such cross-section curves has been plotted in Fig. 5.10. Each of these curves corresponds with a reflection plane of the monochromator or analyzer crystal. With +s the outer curves are obtained and with -s the smaller inner curves. With  $k_{x'} = y$  and  $m - k_{y'} = x$  the function is transformed into

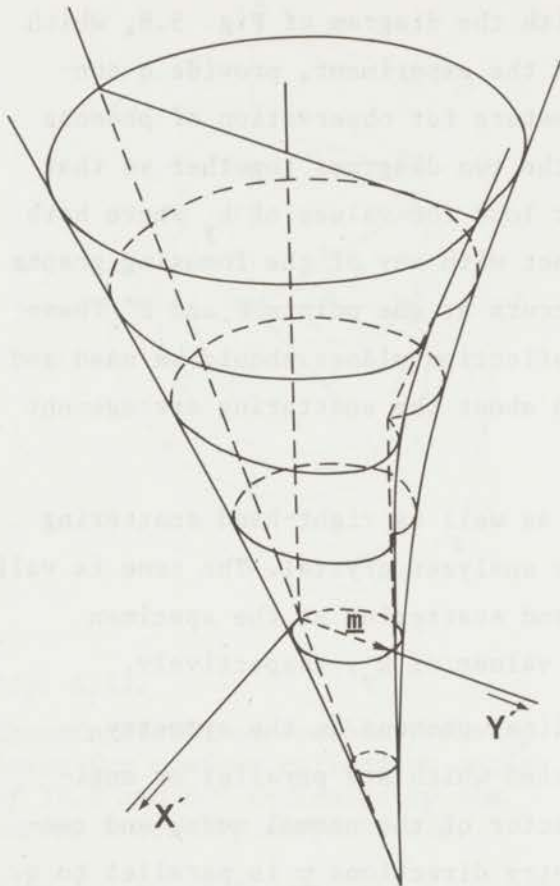
$$(x^2 + y^2 - ax)^2 - b^2(x^2 + y^2) = 0 \quad (5.10)$$

where  $a = m$  and  $b = \frac{1}{2}s$ . In this form the function is known as Pascal's limaçon. In polar coordinate it is written as

$$\begin{aligned} r_1 &= a \cos \eta + b \\ r_2 &= a \cos \eta - b \end{aligned} \quad (5.11)$$

where  $\eta$  is varied between  $-\frac{1}{2}\pi$  and  $+\frac{1}{2}\pi$ .

Section 5.4.



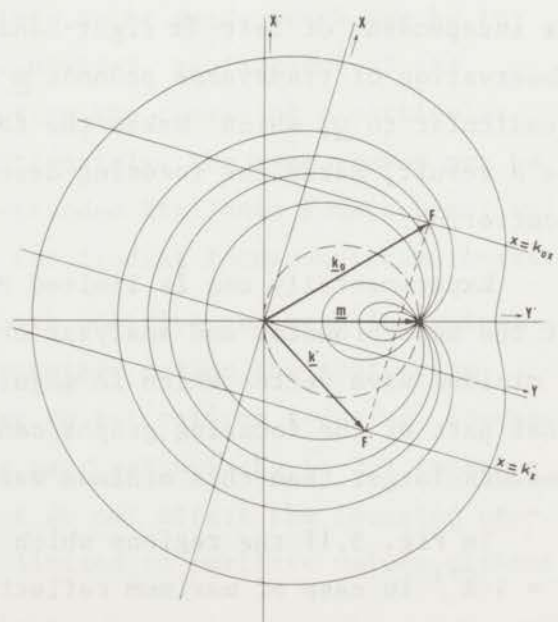
For  $z < -2m$  there are no solutions  
 For  $-2m < z < 0$  the smaller inner curves are obtained, corresponding with  $\underline{k} - \underline{m}$  and  $\underline{s}$  anti-parallel  
 For  $z = 0$  the cross-section is a circle of diameter  $m$   
 For  $0 < z < 2m$  the larger outer curves are obtained still going through the point  $(0, m)$ ; they correspond with  $\underline{k} - \underline{m}$  parallel with  $\underline{s}$

Fig. 5.9.  
 Focusing function  $F(k_x, k_y)$ .

For  $2m < z$  the function is continuous and encloses the point  $(0, m)$ .

The cross-sections of vertical planes through the point  $(0, m)$  are formed by

Fig. 5.10.  
 Focusing graphs which are sections of the planes  $z = \pm s$  through the focusing function  $F(k_x, k_y)$  for a particular value of  $m$ . A construction of the focusing parameters is shown for the measurement of a phonon with  $k_{ox}, k'_x$  and  $m$ .



straight lines having slopes with the horizontal plane equal to two.

The focusing graphs together with the diagram of Fig. 5.8, which contains the relevant information of the experiment, provide a convenient way of determining the parameters for observation of phonons under focused conditions. Bringing the two diagrams together so that the two vectors  $\underline{m}$  coincide, one must look for values of  $k_y$  where both the lines  $x = k_{ox}$  and  $x = k_x^-$  intersect with any of the focusing graphs simultaneously. In Fig. 5.10 this occurs at the points F and F'. These points indicate immediately which reflection planes should be used and in addition they provide information about the scattering arrangement of the spectrometer.

Focusing may involve left-hand as well as right-hand scattering both at the monochromator and at the analyzer crystal. The same is valid for the specimen; left- and right-hand scattering at the specimen correspond to negative and positive values of  $k_y$ , respectively.

For the measurement of longitudinal phonons in the symmetry directions those  $\underline{Q}$ -vectors are selected which are parallel or anti-parallel with  $\underline{\xi}$ , the polarization vector of the normal mode, and consequently with  $\underline{m}$ , since in the symmetry directions  $\underline{m}$  is parallel to  $\underline{q}$ . In the focusing graph this means that  $\underline{m}$  coincides with the X-axis. In that way the diagram becomes symmetric in  $k_y$ , which means that focusing is independent of left- or right-hand scattering at the sample. For the observation of transverse phonons  $\underline{m}$  is preferably approximately perpendicular to  $\underline{Q}$ , which makes the focusing graph asymmetric in  $k_y$  and as a result, makes the focusing dependent on left- or right-hand scattering.

Experimentally one is limited by the range of reflection angles of the monochromator and analyzer crystals. This angular range defines a minimum wave vector which in magnitude will be  $> \frac{1}{2}s$ . Therefore, only that part of the focusing graphs can be used which corresponds to wave vectors larger than this minimum wave vector.

In Fig. 5.11 the regions which are experimentally accessible for  $m = 4 \text{ \AA}^{-1}$  in case of maximum reflection angles of  $38.5^\circ$  and  $60^\circ$ , respectively, are indicated by the closed dashed curves I and II.

Section 5.4.

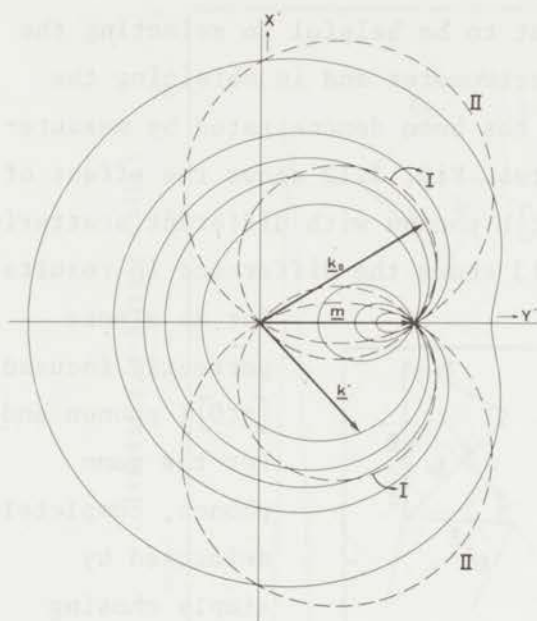


Fig. 5.11.

Experimentally accessible focusing areas for maximum reflection angles of  $38.5^\circ$  and  $60^\circ$  indicated by the curves I and II, respectively.

drastically limited by the range of the reflection angles  $\theta_M$  and  $\theta_A$ .

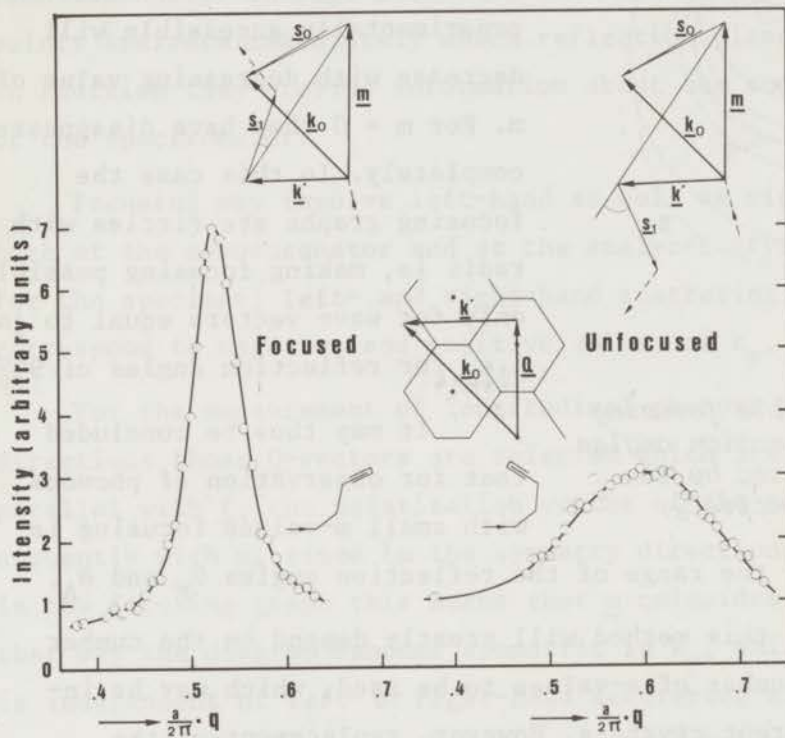
The usefulness of this method will greatly depend on the number of graphs, i.e., the number of  $s$ -values to be used, which may be increased by using different crystals. However, replacement of the monochromator or analyzer crystal during the course of a particular experiment has obvious drawbacks. Fortunately, the same phonon may be observed in different zones of the extended Brillouin zone scheme, which greatly increases the possibilities for finding focused circumstances.

It has been demonstrated that both positive and negative values of the angles  $\theta_M$ ,  $\phi$ , and  $\theta_A$ , which together define the scattering arrangement, may be required in order to get optimum focusing. However, as rotation of the sample around its vertical axis by  $(\pi - 2\psi)$  together with reversal of sign of  $\theta_M$ ,  $\theta_A$  and  $\phi$  do not affect the focusing properties, one of these angles may be limited to positive values without losing the generality of the method.

These curves, which are close to circles, intersect the focusing graphs at positions which have distances to the origin just equal to the minimum wave vectors corresponding to those maximum reflection angles. One can easily verify that the regions which are experimentally accessible will decrease with decreasing value of  $m$ . For  $m = 0$  they have disappeared completely. In this case the focusing graphs are circles with radii  $\frac{1}{2}s$ , making focusing possible only for wave vectors equal to  $\frac{1}{2}s$ , i.e. for reflection angles of  $90^\circ$ .

It may thus be concluded that for observation of phonons with small  $m$ -values focusing is

Due to experimental limitations perfect focusing cannot always be attained, but the method has turned out to be helpful in selecting the most favourable arrangement of the spectrometer and in obtaining the optimum experimental parameters. This has been demonstrated by measurements of phonons in an aluminium crystal. Fig. 5.12 shows the effect of focusing for the measurement of a  $[00\zeta]$ L phonon with different scattering arrangements at the analyzer. Fig. 5.13 shows the difference in results



for an almost perfectly focused  $[\zeta\zeta 0]$ T phonon and for the same phonon, completely defocused by simply choosing different positions in reciprocal space. The arrangements of the neutron beams at the spectrometer were the same in these two experiments.

Fig. 5.12.

Observed INS peaks with the corresponding scattering arrangements and focusing diagrams for a  $[00\zeta]$ L phonon in aluminium with scattering at the analyzer in different directions.

### 5.5. Inverse beryllium-filter method

In the case of zinc blende the observation of the optic branches turned out to be difficult and for many branches impossible when the measurements were carried out according to the constant-Q technique. This technique was the only applicable one because optic branches usually have a relatively small slope. Since Haywood, Collins and Lowde<sup>7)</sup>

Section 5.5.

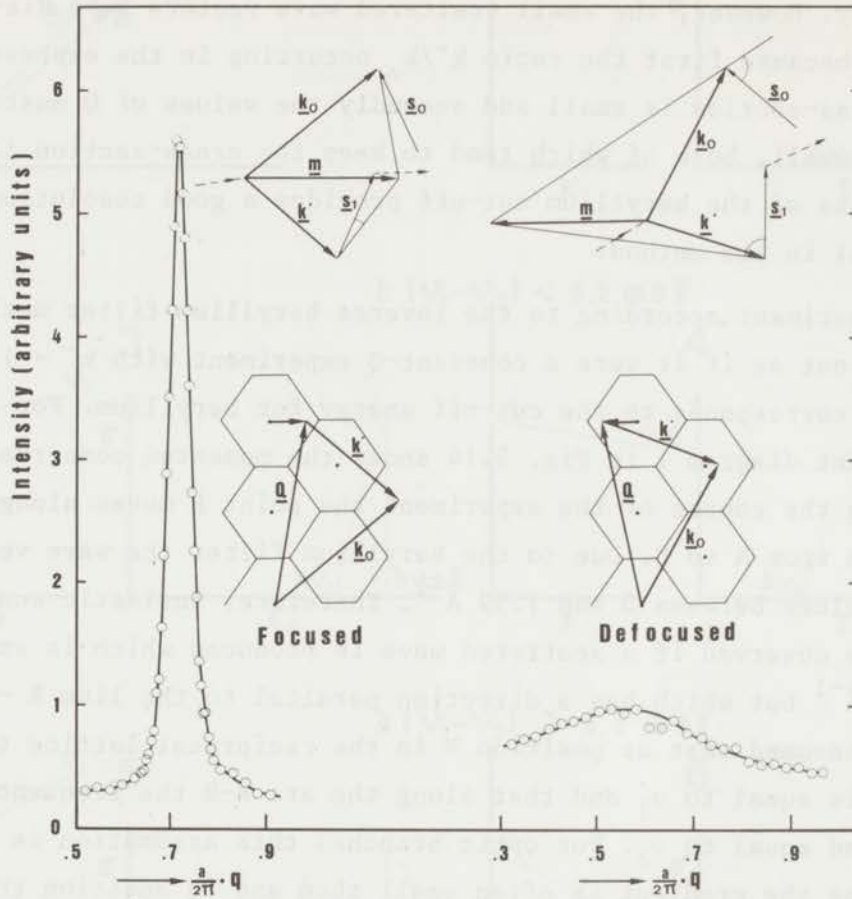


Fig. 5.13. Observed INS peaks with the corresponding scattering arrangements and focusing diagrams for a  $[\bar{z}z0]_T$  phonon in aluminium measured at opposite sides of a Brillouin zone centre.

applied the inverse beryllium-filter method successfully in an investigation of optic phonons in manganese oxide, this method has been used for experiments on zinc blende. The method was first used by Stiller and Danner<sup>8)</sup> and by Woods *et al.*<sup>9)</sup> for inelastic scattering in mainly polycrystals and liquids. A polycrystalline beryllium filter is used in front of the detector and the analyzer crystal is removed. The filter allows the transmission of neutrons with energies between zero and the cut-off energy; for beryllium this cut-off energy is at 5.2 meV. The wave vectors of the scattered neutrons must be small and consequently the collimation of the scattered neutrons can be relaxed without losing too much resolution. Besides that, it is an advantage that the

transmission of the beryllium filter is larger than the analyzer reflectivity. However, the small scattered wave vectors have disadvantages because first the ratio  $k'/k_0$  occurring in the expression for the cross-section is small and secondly the values of  $Q$  must be moderately small, both of which tend to keep the cross-section low. The sharpness of the beryllium cut-off provides a good resolution and is essential in the method.

An experiment according to the inverse beryllium-filter method is carried out as if it were a constant- $Q$  experiment with  $k' = 1.59 \text{ \AA}^{-1}$ ; this value corresponds to the cut-off energy for beryllium. For such an experiment diagram 1 in Fig. 5.14 shows the momentum conservation law. During the course of the experiment the point  $P$  moves along an arc of a circle from  $A$  to  $B$ . Due to the beryllium filter the wave vector  $k'$  can have values between 0 and  $1.59 \text{ \AA}^{-1}$ . Therefore, inelastic scattering may also be observed if a scattered wave is produced which is smaller than  $1.59 \text{ \AA}^{-1}$  but which has a direction parallel to the line  $R - P$ . It is now assumed that at position  $R$  in the reciprocal lattice the frequency is equal to  $\nu_1$  and that along the arc  $A-B$  the frequency is constant and equal to  $\nu_2$ . For optic branches this assumption is mostly justified as the gradient is often small then and in addition the length of the arc  $A-B$  is rather short in most experiments. Depending on the relative values of  $\nu_1$  and  $\nu_2$ , *i.e.* the course of  $\nu$  along  $\underline{k}'$  as this vector was defined in the constant- $Q$  experiment, a number of scattering patterns may be distinguished. For  $\nu_1 = \nu_2 = \nu$  diagram 2 gives  $\nu$  as a function of  $k'$  and the shape of the cross-section as a function of the incident neutron energy. For  $E_0 < h\nu$  the conservation laws cannot be satisfied; if  $E_0 = h\nu$  scattering starts to become possible but with  $k' = 0$  and, therefore, the cross-section is equal to zero. With growing  $E_0$  the cross-section increases until  $E_0 = h\nu + 5.2 \text{ meV}$  where the scattered neutron energy reaches the beryllium cut-off energy. At this point the intensity decreases sharply to zero. In the other diagram of Fig. 5.14 the dispersion relation along  $\underline{k}'$  and the shape of the cross-section versus  $E_0$  have been sketched for  $h|\nu_1 - \nu_2|$  smaller than, larger than or equal to  $5.2 \text{ meV}$ , and for both increasing or decreasing  $\nu$  along  $\underline{k}'$ . In all diagrams the cut-off value of  $E_0$  provides

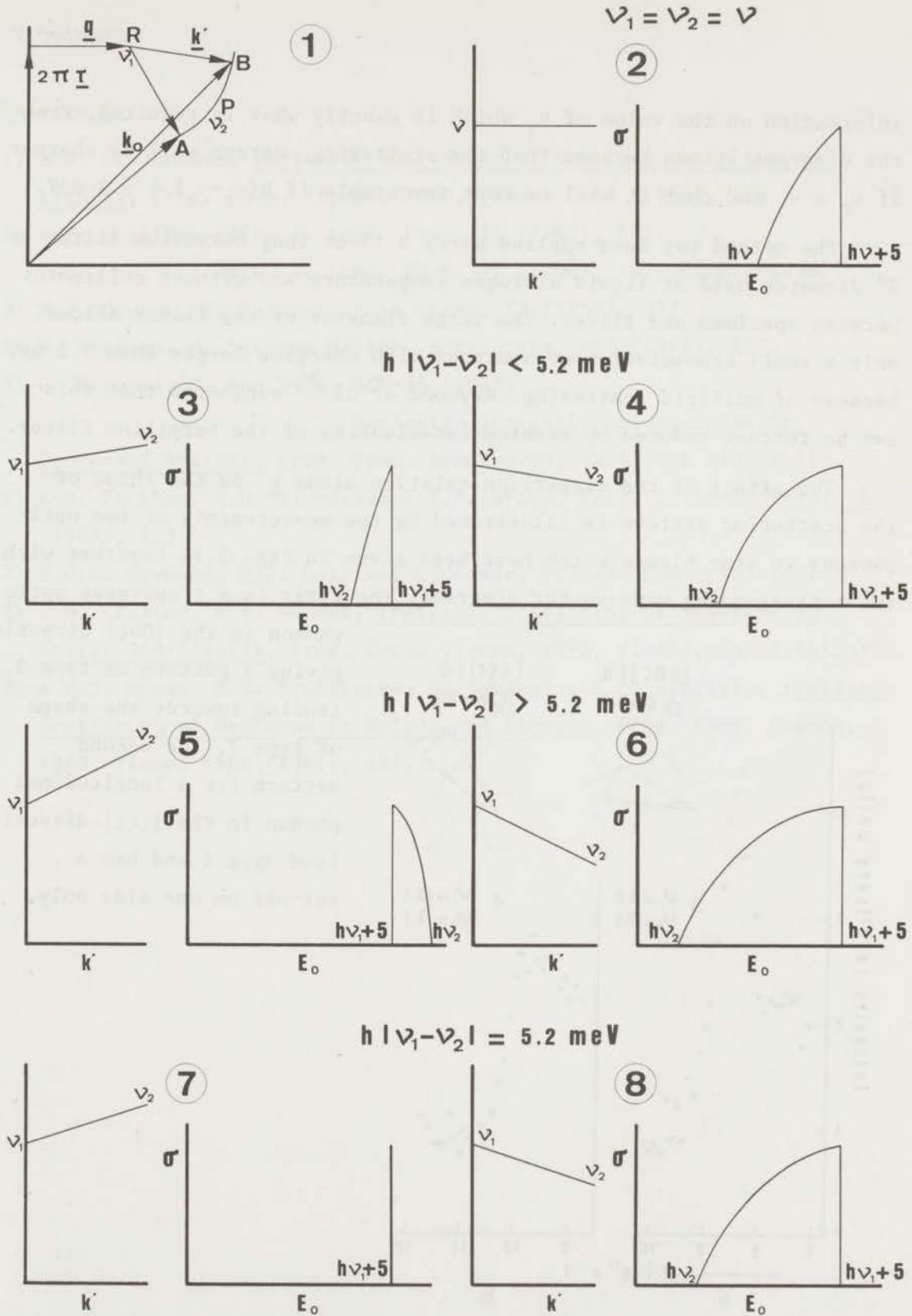


Fig. 5.14. The inverse beryllium-filter technique applied to phonon scattering in single crystals. Diagrams demonstrate the way in which the shape of the scattering pattern as a function of the incident neutron energy is determined by the dispersion relation along  $k'$ .

information on the value of  $\nu_1$  which is exactly what is required. From the diagrams it can be seen that the scattering pattern will be sharper if  $\nu_2 > \nu_1$  and that it will be most favourable if  $h(\nu_2 - \nu_1) = 5.2$  meV.

The method has been applied using a 15 cm long beryllium filter of 2" diameter held at liquid nitrogen temperature and without collimator between specimen and filter. The large diameter of the filter allows only a small transmission of neutrons with energies larger than 5.2 meV because of multiple scattering. Haywood *et al.*<sup>7)</sup> suggested that this can be further reduced by cadmium interleaving of the beryllium filter.

The effect of the dispersion relation along  $\underline{k}$  on the shape of the scattering pattern is illustrated by the measurements of two optic phonons in zinc blende which have been given in Fig. 5.15 together with the corresponding wave-vector diagrams. The first is a transverse optic phonon in the  $[00\zeta]$ -direction giving a pattern of type 3, tending towards the shape of type 7. The second pattern for a longitudinal phonon in the  $[\zeta\zeta\zeta]$ -direction is of type 4 and has a cut-off on one side only.

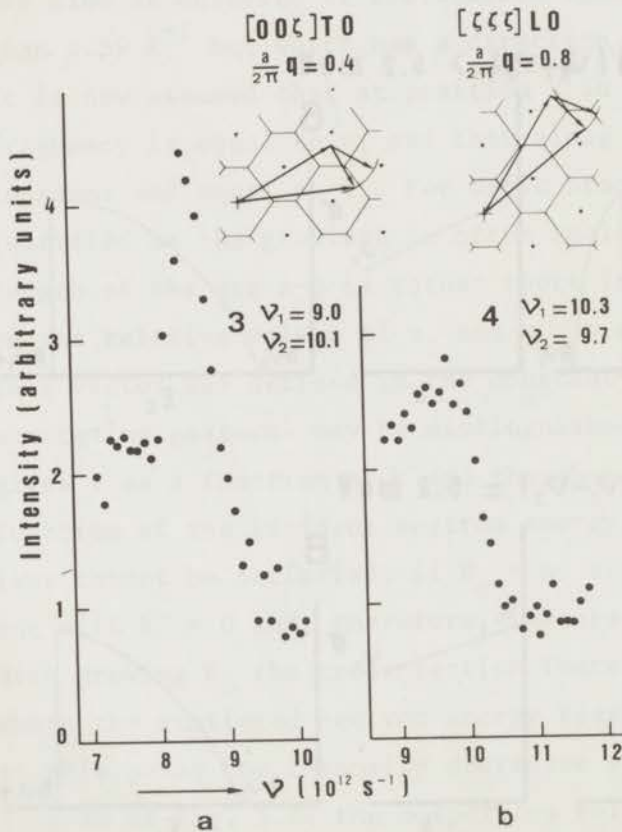


Fig. 5.15.

INS patterns, observed by means of the inverse beryllium-filter technique for optic phonons in zinc blende; the dispersion relations along  $\underline{k}$  had opposite gradients. a:  $[00\zeta]$  TO phonon, b:  $[\zeta\zeta\zeta]$  LO phonon.

References

- 1) B.N. Brockhouse, Inelastic Scattering of Neutrons in Solids and Liquids, Proc. Symp. Vienna, 1960, Vienna IAEA (1961), 113.
- 2) M.F. Collins, Brit. J. Appl. Phys. 14 (1963), 805.  
Brit. J. Appl. Phys. 17 (1966), 147, corrigendum.
- 3) M.J. Cooper, R. Nathans, Acta Cryst. 23 (1967), 357.
- 4) M. Nielsen, H. Bjerrum Møller, Acta Cryst. A25 (1968), 547.
- 5) J. Bergsma, C. van Dijk, RCN-36 (1965).  
Inelastic Scattering of Neutrons by Condensed Systems, Proc. Symp. Brookhaven, 1965, BNL 940 (C-45)
- 6) G.E. Peckham, D.H. Saunderson, R.I. Sharp, Brit. J. Appl. Phys. 18 (1967), 473.
- 7) B.C.G. Haywood, M.F. Collins, R.D. Lowde, Private Communication.
- 8) H.H. Stiller, H.R. Danner, Inelastic Scattering of Neutrons in Solids and Liquids, Proc. Symp. Vienna, 1960, Vienna, IAEA(1961), 363.
- 9) A.D.B. Woods, B.N. Brockhouse, M. Sakamoto, R.N. Sinclair, Inelastic Scattering of Neutrons in Solids and Liquids, Proc. Symp. Vienna, 1960, Vienna IAEA (1961), 487.

## Chapter VI

## MAGNESIUM STANNIDE

6.1. Introduction

The compounds formed by the elements of group IV with magnesium crystallize according to the antiferroite structure and are all semiconductors, apart from  $Mg_2Pb$ , which is a conductor. From optical and electrical measurements it has been found that they are indirect-gap semiconductors; the energy gap for  $Mg_2Sn$  is  $0.32 \text{ eV}^{1,2,3)}$ , which is small compared to  $0.74 \text{ eV}$  for  $Mg_2Si^{3,4)}$  and  $0.72 \text{ eV}$  for  $Mg_2Ge^{3,4,5)}$ . Most semiconductors have diamond or zinc blende structure and, therefore, these magnesium compounds having a different crystal structure are interesting for the application of band theory calculations. Such calculations have been carried out for  $Mg_2Si$  and  $Mg_2Ge$  by Lee<sup>6)</sup> and for  $Mg_2Si$  by Folland<sup>7)</sup> and recently for these compounds and for  $Mg_2Sn$  by Au-Yang and Cohen<sup>3)</sup>. In all these calculations a maximum in the valence band has been found at the centre of the Brillouin zone while a minimum in the conduction band was found along the  $[001]$ -direction or at the zone-boundary point (001). Consequently, phonons of wave vectors along the  $[001]$ -direction are involved in the indirect transitions between the valence band and the conduction band. According to the calculations by Au-Yang and Cohen<sup>3)</sup> the conduction-band minimum in magnesium stannide is at (001). The direct transitions with lowest energy occur at the zone centre. For the energy of these direct transitions the value  $1.06 \text{ eV}$  has been obtained and for the indirect transitions  $0.64 \text{ eV}$ . The discrepancy of the last value with the experimental result has been attributed to spin-orbit interactions which have been neglected in the calculation. For a better understanding of the semiconducting properties the knowledge of the phonon dispersion relation is evidently of importance.

Closely related to the semiconducting properties is the type of interatomic bonding in the crystal. Although these magnesium compounds have several properties in common with germanium and silicon suggesting a predominantly covalent bonding, some evidence for partly ionic bonding has been obtained from infra-red reflection measurements<sup>2,8)</sup>. For

### Section 6.1.

magnesium stannide the elastic constants have been calculated from velocity-of-sound measurements by Davis *et al.*<sup>9)</sup>;  $c_{11} = 8.24 \times 10^{11}$ ,  $c_{12} = 2.08 \times 10^{11}$  and  $c_{44} = 3.66 \times 10^{11}$  dyn.cm<sup>-2</sup>. From the value of the isotropy coefficient  $(c_{11} - c_{12})/2c_{44}$  equal to 0.84 and from the relative magnitudes of the elastic constants these authors concluded to a strong resemblance to covalent semiconductors. They point out that on the other hand the difference in the high- and low-frequency dielectric constants is characteristic for an ionic compound. These dielectric constants have been obtained from infra-red reflection by Kahan *et al.*<sup>10)</sup>;  $\epsilon_{\infty} = 15.5$ ,  $\epsilon_0 = 23.75$  and the transverse optic frequency at the zone centre  $\nu_{TO}$  is equal to  $5.57 \times 10^{12}$  s<sup>-1</sup>. Therefore, the bonding in magnesium stannide is considered to be partly covalent and partly ionic. As an aid in the study of a crystal with such a mixed bonding the analysis of the phonon dispersion relation was undertaken.

### 6.2. Lattice dynamics

#### 6.2.1. Short-range force constants and coupling coefficients

The fluorite lattice consists of three interpenetrating face-centred cubic sublattices. In the case of magnesium stannide these are occupied by one tin and two magnesium atoms. As a primitive unit cell a rhombohedron is defined by the translation vectors  $\underline{a}_1 = \frac{1}{2}a(0,1,1)$ ,  $\underline{a}_2 = \frac{1}{2}a(1,0,1)$  and  $\underline{a}_3 = \frac{1}{2}a(1,1,0)$  where  $a$  is the lattice constant of the cubic unit cell, equal to 6.7625 Å. The positions of the three atoms in the primitive cell are given by  $r(\kappa) = \frac{1}{4}a(\kappa-1)(1,1,1)$  where  $\kappa=1$  for tin and  $\kappa=2$  and 4 for the two magnesium atoms. Here and in the following the vector notation  $(x,y,z)$  refers to Cartesian coordinates. The lattice dynamics of the fluorite structure has been discussed by Srinivasan<sup>11)</sup> and by Ganesan and Srinivasan<sup>12)</sup> and for the particular case of uranium dioxide by Dolling *et al.*<sup>13)</sup>.

The short-range interactions to be taken into account, with the interatomic vectors and the force constant matrices according to (2.3) and subject to the symmetry requirements, are the following

$$\text{Sn - Mg: } (\kappa\kappa') = (12)$$

$$\underline{r}(1'_t\kappa') - \underline{r}(0\kappa) = \frac{1}{4}a(1,1,1) \text{ and equivalent vectors}$$

$$\phi(0\kappa; 1'_t\kappa') = \begin{vmatrix} \alpha_1 & \beta_1 & \beta_1 \\ \beta_1 & \alpha_1 & \beta_1 \\ \beta_1 & \beta_1 & \alpha_1 \end{vmatrix} \quad (6.1)$$

$$\text{Sn - Sn: } (\kappa\kappa') = (11)$$

$$\underline{r}(1'_t\kappa') - \underline{r}(0\kappa) = \frac{1}{2}a(1,1,0) \text{ and equivalent vectors}$$

$$\phi(0\kappa; 1'_t\kappa') = \begin{vmatrix} \alpha_2 & \gamma_2 & 0 \\ \gamma_2 & \alpha_2 & 0 \\ 0 & 0 & \beta_2 \end{vmatrix} \quad (6.2)$$

$$\text{Mg - Mg: } (\kappa\kappa') = (24)$$

$$\underline{r}(1'_t\kappa') - \underline{r}(0\kappa) = \frac{1}{2}a(1,0,0) \text{ and equivalent vectors}$$

$$\phi(0\kappa; 1'_t\kappa') = \begin{vmatrix} \alpha_3 & 0 & 0 \\ 0 & \beta_3 & 0 \\ 0 & 0 & \beta_3 \end{vmatrix} \quad (6.3)$$

The short-range coupling coefficients defined by (3.2) and (3.12) can now be expressed in terms of the seven force constants introduced above and the reduced wave-vector components  $q'_\alpha$ ,  $q'_\beta$  and  $q'_\gamma$  defined by  $\underline{q} = \frac{2\pi}{a}(q'_\alpha, q'_\beta, q'_\gamma)$ .

With

$$\begin{aligned} C_\alpha &= \cos(\frac{1}{2}\pi q'_\alpha), & S_\alpha &= \sin(\frac{1}{2}\pi q'_\alpha) \\ C_{2\alpha} &= \cos(\pi q'_\alpha), & S_{2\alpha} &= \sin(\pi q'_\alpha) \end{aligned}$$

the expressions for the coupling coefficients are as follows

Tin - Tin:

$$R_{\alpha\alpha}(11; \underline{q}) = 8\alpha_1 + 8\alpha_2 + 4\beta_2 - 4\alpha_2 C_{2\alpha} (C_{2\beta} + C_{2\gamma}) - 4\beta_2 C_{2\beta} \cdot C_{2\gamma} \quad (6.4)$$

$$R_{\alpha\beta}(11; \underline{q}) = 4\gamma_2 S_{2\alpha} \cdot S_{2\beta}$$

Section 6.2.

Tin - Magnesium(2), Tin - Magnesium(4):

$$\begin{aligned} R_{\alpha\alpha}(12;\underline{q}) &= R_{\alpha\alpha}^*(14;\underline{q}) = -4\alpha_1(C_\alpha \cdot C_\beta \cdot C_\gamma - iS_\alpha \cdot S_\beta \cdot S_\gamma) \\ R_{\alpha\beta}(12;\underline{q}) &= R_{\alpha\beta}^*(14;\underline{q}) = 4\beta_1(S_\alpha \cdot S_\beta \cdot C_\gamma - iC_\alpha \cdot C_\beta \cdot S_\gamma) \end{aligned} \quad (6.5)$$

Magnesium(2) - Magnesium(2), Magnesium(4) - Magnesium(4):

$$\begin{aligned} R_{\alpha\alpha}(22;\underline{q}) &= R_{\alpha\alpha}(44;\underline{q}) = 4\alpha_1 + 2\alpha_3 + 4\beta_3 \\ R_{\alpha\beta}(22;\underline{q}) &= R_{\alpha\beta}(44;\underline{q}) = 0 \end{aligned} \quad \left. \vphantom{\begin{aligned} R_{\alpha\alpha}(22;\underline{q}) \\ R_{\alpha\beta}(22;\underline{q}) \end{aligned}} \right\} (6.6)$$

Magnesium(2) - Magnesium(4):

$$\begin{aligned} R_{\alpha\alpha}(24;\underline{q}) &= -2\alpha_3 C_{2\alpha} - 2\beta_3(C_{2\beta} + C_{2\gamma}) \\ R_{\alpha\beta}(24;\underline{q}) &= 0 \end{aligned} \quad \left. \vphantom{\begin{aligned} R_{\alpha\alpha}(24;\underline{q}) \\ R_{\alpha\beta}(24;\underline{q}) \end{aligned}} \right\} (6.6)$$

6.2.2. Group theory

The space group of the fluorite structure is  $O_h^5$ , Fm3m, which is symmorphic. In the discussion of the symmetry properties according to group theory mainly Maradudin and Vosko's<sup>14)</sup> notation will be used; this is the same notation as Kovalev's<sup>15)</sup> except that the symmetry elements are denoted by R instead of h. Wave vectors will be denoted by  $\underline{q}$  instead of  $\underline{k}$ , but Kovalev's classification by means of numbers according to the directions of the wave vectors will be maintained. The discussions will be limited to the three directions of highest symmetry  $[001]$ ,  $[110]$  and  $[111]$  which in a face-centred cubic lattice correspond to Kovalev's vectors  $\underline{k}_6$ ,  $\underline{k}_4$  and  $\underline{k}_5$ , respectively. The irreducible representations and characters of the point groups of these wave vectors have been taken from the tables given by Kovalev for the space group of the crystal.

In the character tables the relations with the Bouckaert-Smoluchowski-Wigner notation<sup>16)</sup> will be given too as this is also widely used. The labelling of the branches of the dispersion relation and of the special points and directions in the Brillouin zone will be according to this BSW notation. These special points and directions with their labels are shown in Fig. 6.1. The symmetry elements R used in this and the next chapter have been presented in matrix form in the Appendix.

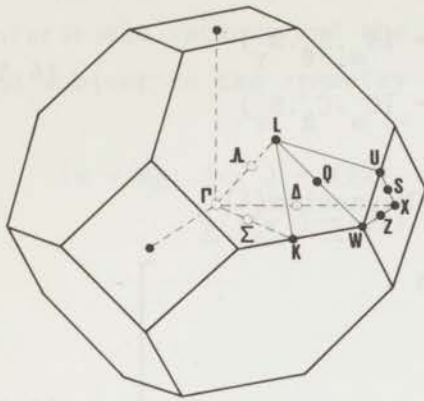


Fig. 6.1.

Brillouin zone for the face-centred cubic lattice showing special points and directions and their labels according to the BSW notation 16).

$[001], \underline{q} = \underline{q}_6$

The point group of the wave vector  $\underline{q}_6$  is  $C_{4v}$ , which has eight symmetry elements distributed over five classes and consequently it has five irreducible representations. Four of these are one-dimensional and one is two-dimensional. These irreducible representations and their characters have been given in Table 6.1.

Table 6.1. Irreducible representations and characters of the group  $C_{4v}(\underline{q}_6)$ ; these representations have been denoted according to Kovalev's and the BSW notation. The characters of reducible representation  $T(\underline{q}_6)$  have been given in the last line.

Kovalev	$R_1$	$R_4$	$R_{14}$	$R_{15}$	$R_{26}$	$R_{27}$	$R_{37}$	$R_{40}$	BSW
$\tau_1$	1	1	1	1	1	1	1	1	$\Delta_1$
$\tau_2$	1	1	1	1	-1	-1	-1	-1	$\Delta'_1$
$\tau_3$	1	1	-1	-1	1	1	-1	-1	$\Delta_2$
$\tau_4$	1	1	-1	-1	-1	-1	1	1	$\Delta'_2$
$\tau_5$	$\begin{vmatrix} 1 & 0 \\ 0 & 1 \end{vmatrix}$	$\begin{vmatrix} -1 & 0 \\ 0 & -1 \end{vmatrix}$	$\begin{vmatrix} 0 & -1 \\ 1 & 0 \end{vmatrix}$	$\begin{vmatrix} 0 & 1 \\ -1 & 0 \end{vmatrix}$	$\begin{vmatrix} 0 & 1 \\ 1 & 0 \end{vmatrix}$	$\begin{vmatrix} 0 & -1 \\ -1 & 0 \end{vmatrix}$	$\begin{vmatrix} 1 & 0 \\ 0 & -1 \end{vmatrix}$	$\begin{vmatrix} -1 & 0 \\ 0 & 1 \end{vmatrix}$	$\Delta_5$
$\chi^{\tau_5}$	2	-2	0	0	0	0	0	0	
$\chi^T$	9	-3	1	1	1	1	3	3	

Section 6.2.

The representation  $\tau_5$  given by Kovalev has been transformed by means of a similarity transformation<sup>14)</sup>.

The reducible representation  $T(\underline{q}_6)$ , defined by (2.30) now takes the form

$$\begin{aligned}
 T(\underline{q}_6, R_1) &= \begin{vmatrix} R_1 & 0 & 0 \\ 0 & R_1 & 0 \\ 0 & 0 & R_1 \end{vmatrix} & T(\underline{q}_6, R_4) &= \begin{vmatrix} R_4 & 0 & 0 \\ 0 & R_4 & 0 \\ 0 & 0 & R_4 \end{vmatrix} \\
 T(\underline{q}_6, R_{14}) &= \begin{vmatrix} R_{14} & 0 & 0 \\ 0 & 0 & \rho_2 R_{14} \\ 0 & \rho_2^* R_{14} & 0 \end{vmatrix} & T(\underline{q}_6, R_{15}) &= \begin{vmatrix} R_{15} & 0 & 0 \\ 0 & 0 & \rho_2 R_{15} \\ 0 & \rho_2^* R_{15} & 0 \end{vmatrix} \\
 T(\underline{q}_6, R_{26}) &= \begin{vmatrix} R_{26} & 0 & 0 \\ 0 & 0 & \rho_2 R_{26} \\ 0 & \rho_2^* R_{26} & 0 \end{vmatrix} & T(\underline{q}_6, R_{27}) &= \begin{vmatrix} R_{27} & 0 & 0 \\ 0 & 0 & \rho_2 R_{27} \\ 0 & \rho_2^* R_{27} & 0 \end{vmatrix} \\
 T(\underline{q}_6, R_{37}) &= \begin{vmatrix} R_{37} & 0 & 0 \\ 0 & R_{37} & 0 \\ 0 & 0 & R_{37} \end{vmatrix} & T(\underline{q}_6, R_{40}) &= \begin{vmatrix} R_{40} & 0 & 0 \\ 0 & R_{40} & 0 \\ 0 & 0 & R_{40} \end{vmatrix}
 \end{aligned} \tag{6.7}$$

Here  $\rho_2 = \rho(24; \underline{q}_6)$ , defined by (2.14).

The characters of this representation are given in the last line of Table 6.1. Inserting these characters and with the character table for the irreducible representations,  $T(\underline{q}_6)$  can be decomposed by means of (2.34):

$T(\underline{q}_6) = 2\tau_1 \oplus \tau_4 \oplus 3\tau_5$ . From this decomposition it may be concluded that for wave vector  $\underline{q}_6$  there are three  $\tau_5$  branches each with a two-fold degeneracy and one  $\tau_4$  and two  $\tau_1$  branches; the  $\tau_1$  and  $\tau_4$  branches are non-degenerate.

By means of (2.36) the projection operator matrices for these irreducible representations are found to be

$$P(\underline{q}_6, \tau_1) = \begin{vmatrix} 0 & 0 & 0 \\ 0 & 0 & 0 & 0 & 0 \\ 0 & 0 & 8 & & \\ & 0 & 0 & 0 & 0 & 0 & 0 \\ 0 & 0 & 0 & 0 & 0 & 0 & 0 \\ & 0 & 0 & 4 & 0 & 0 & 4\rho_2 \\ & 0 & 0 & 0 & 0 & 0 & 0 \\ 0 & 0 & 0 & 0 & 0 & 0 & 0 \\ & 0 & 0 & 4\rho_2^* & 0 & 0 & 4 \end{vmatrix}; \quad P(\underline{q}_6, \tau_4) = \begin{vmatrix} 0 & 0 & 0 \\ & 0 & 0 & 0 & 0 & 0 \\ & 0 & 0 & 0 & 0 & 0 \\ & 0 & 0 & 4 & 0 & 0 & -4\rho_2 \\ & 0 & 0 & 0 & 0 & 0 & 0 \\ 0 & 0 & 0 & 0 & 0 & 0 & 0 \\ & 0 & 0 & -4\rho_2^* & 0 & 0 & 4 \end{vmatrix}$$

$$P_{11}(\underline{q}_6, \tau_5) = \begin{vmatrix} 2 & 2 & 0 \\ 2 & 2 & 0 & 0 & 0 \\ 0 & 0 & 0 & & \\ & 2 & 2 & 0 \\ 0 & 2 & 2 & 0 & 0 \\ & 0 & 0 & 0 & \\ & & 2 & 2 & 0 \\ 0 & 0 & 2 & 2 & 0 \\ & & 0 & 0 & 0 \end{vmatrix}; \quad P_{21}(\underline{q}_6, \tau_5) = \begin{vmatrix} -2 & -2 & 0 & & & \\ 2 & 2 & 0 & 0 & & 0 \\ 0 & 0 & 0 & & & \\ & 0 & 0 & & -2\rho_2 & -2\rho_2 & 0 \\ & & 0 & & 2\rho_2 & 2\rho_2 & 0 \\ & & & & 0 & 0 & 0 \\ & & & -2\rho_2^* & -2\rho_2^* & 0 \\ 0 & 2\rho_2^* & 2\rho_2^* & 0 & & 0 \\ & 0 & 0 & 0 & & 0 \end{vmatrix}$$

(6.8)

With these operators and (2.37) the following symmetry adapted eigenvectors have been obtained; they have been labelled according to the BSW notation

$$P(\underline{q}_6, \tau_1) \cdot \psi = \begin{vmatrix} 0 \\ 0 \\ 8\psi_z(1) \\ 0 \\ 0 \\ 4\{\psi_z(2) + \rho_2\psi_z(3)\} \\ 0 \\ 0 \\ 4\{\rho_2^*\psi_z(2) + \psi_z(3)\} \end{vmatrix} = \begin{vmatrix} 0 \\ 0 \\ a_1 \\ 0 \\ 0 \\ b_1 \\ 0 \\ 0 \\ \rho_2^*b_1 \end{vmatrix} = E(\Delta_1)$$

$$P(\underline{q}_6, \tau_4) \cdot \psi = \begin{vmatrix} 0 \\ 0 \\ 0 \\ 0 \\ 0 \\ 4\{\psi_z(2) - \rho_2\psi_z(3)\} \\ 0 \\ 0 \\ -4\{\rho_2^*\psi_z(2) - \psi_z(3)\} \end{vmatrix} = \begin{vmatrix} 0 \\ 0 \\ 0 \\ 0 \\ 0 \\ a_2 \\ 0 \\ 0 \\ -\rho_2^*a_2 \end{vmatrix} = E(\Delta_2')$$

Section 6.2.

$$P_{11}(\underline{q}_6, \tau_5) \cdot \psi = \begin{vmatrix} 2\{\psi_x(1)+\psi_y(1)\} \\ 2\{\psi_x(1)+\psi_y(1)\} \\ 0 \\ 2\{\psi_x(2)+\psi_y(2)\} \\ 2\{\psi_x(2)+\psi_y(2)\} \\ 0 \\ 2\{\psi_x(3)+\psi_y(3)\} \\ 2\{\psi_x(3)+\psi_y(3)\} \\ 0 \end{vmatrix} = \begin{vmatrix} a_5 \\ a_5 \\ 0 \\ b_5 \\ b_5 \\ 0 \\ c_5 \\ c_5 \\ 0 \end{vmatrix} = E(\Delta_5 \ 1)$$

$$P_{21}(\underline{q}_6, \tau_5) \cdot \psi = \begin{vmatrix} -2\{\psi_x(1)+\psi_y(1)\} \\ 2\{\psi_x(1)+\psi_y(1)\} \\ 0 \\ -2\rho_2\{\psi_x(3)+\psi_y(3)\} \\ 2\rho_2\{\psi_x(3)+\psi_y(3)\} \\ 0 \\ -2\rho_2^*\{\psi_x(2)+\psi_y(2)\} \\ 2\rho_2^*\{\psi_x(2)+\psi_y(2)\} \\ 0 \end{vmatrix} = \begin{vmatrix} -a_5 \\ a_5 \\ 0 \\ -\rho_2 c_5 \\ \rho_2 c_5 \\ 0 \\ -\rho_2^* b_5 \\ \rho_2^* b_5 \\ 0 \end{vmatrix} = E(\Delta_5 \ 2) \tag{6.9}$$

$E(\Delta_1)$  and  $E(\Delta_2')$  represent longitudinal vibrations and  $E(\Delta_5 \ 1)$  and  $E(\Delta_5 \ 2)$  are orthogonal transverse modes.

Using expressions (6.4) to (6.6) and the definitions (2.9), (2.14) and (3.12) for the dynamical matrix, and the eigenvectors expressed by (2.13), equation (2.38) can for each of the irreducible representations  $\Delta_1$ ,  $\Delta_2'$  and  $\Delta_5$  be expressed in terms of the dynamical matrix and the basis vectors for the corresponding subspaces as follows:

for  $\Delta_1$ :

$$\begin{vmatrix} D_{zz}(11) - \omega^2 & \sqrt{2}\rho_1 D_{zz}(12) \\ \sqrt{2}\rho_1^* D_{zz}(12) & D_{zz}(22) + D_{zz}(24) - \omega^2 \end{vmatrix} \times \begin{vmatrix} a_1 \\ b_1 \end{vmatrix} = 0 \tag{6.10}$$

for  $\Delta_2'$ :

$$\left| D_{zz}(22) - D_{zz}(24) - \omega^2 \right| \times \left| a_2 \right| = 0 \tag{6.11}$$

for  $\Delta_5$ :

$$\begin{vmatrix} D_{xx}(11) - \omega^2 & \rho_1 \{D_{xx}(12) + D_{xy}(12)\} & \rho_3 \{D_{xx}(12) - D_{xy}(12)\} \\ \rho_1^* \{D_{xx}(12) - D_{xy}(12)\} & D_{xx}(22) - \omega^2 & \rho_2 D_{xx}(24) \\ \rho_3^* \{D_{xx}(12) + D_{xy}(12)\} & \rho_2^* D_{xx}(24) & D_{xx}(22) - \omega^2 \end{vmatrix} \times \begin{vmatrix} a_5 \\ b_5 \\ c_5 \end{vmatrix} = 0$$

(6.12)

Here,  $\rho_1 = \rho(12; \underline{q}_6)$  and  $\rho_3 = \rho(14; \underline{q}_6)$ .

The solution of these three equations produces the eigenvalues and the eigenvectors. From the eigenvalues the frequencies can be obtained and the eigenvectors can be substituted into expressions (6.9) to give the eigenvectors of the full dynamical matrix.

In order to save space the group-theoretical treatments of the other point groups in this and the next chapter will be given in abbreviated form.

[111],  $\underline{q} = \underline{q}_5$

The point group of the wave vector is  $C_{3v}$  which has six symmetry elements divided into three classes. From the three irreducible representations two are one-dimensional and one is two-dimensional. These representations and their characters have been given in Table 6.2. The representation  $\tau_3$  given by Kovalev has been transformed by means of a similarity transformation<sup>14)</sup>. The following set of matrices comprise the reducible representation  $T(\underline{q}_5)$

$$T(\underline{q}_5, R_1) = \begin{vmatrix} R_1 & 0 & 0 \\ 0 & R_1 & 0 \\ 0 & 0 & R_1 \end{vmatrix}$$

$$T(\underline{q}_5, R_9) = \begin{vmatrix} R_9 & 0 & 0 \\ 0 & R_9 & 0 \\ 0 & 0 & R_9 \end{vmatrix}$$

$$T(\underline{q}_5, R_5) = \begin{vmatrix} R_5 & 0 & 0 \\ 0 & R_5 & 0 \\ 0 & 0 & R_5 \end{vmatrix}$$

$$T(\underline{q}_5, R_{37}) = \begin{vmatrix} R_{37} & 0 & 0 \\ 0 & R_{37} & 0 \\ 0 & 0 & R_{37} \end{vmatrix}$$

Section 6.2.

$$T(\underline{q}_5, R_{41}) = \begin{vmatrix} R_{41} & 0 & 0 \\ 0 & R_{41} & 0 \\ 0 & 0 & R_{41} \end{vmatrix} \quad T(\underline{q}_5, R_{45}) = \begin{vmatrix} R_{45} & 0 & 0 \\ 0 & R_{45} & 0 \\ 0 & 0 & R_{45} \end{vmatrix} \quad (6.13)$$

The characters of this representation have been given in Table 6.2.

Table 6.2. Irreducible representations and characters of the group  $C_{3v}(\underline{q}_5)$ . The characters of the reducible representation  $T(\underline{q}_5)$  have been given in the last line.

Kovalev	$R_1$	$R_9$	$R_5$	$R_{37}$	$R_{41}$	$R_{45}$	BSW
$\tau_1$	1	1	1	1	1	1	$\Lambda_1$
$\tau_2$	1	1	1	-1	-1	-1	$\Lambda_2$
$\tau_3$	$\begin{vmatrix} 1 & 0 \\ 0 & 1 \end{vmatrix}$	$\begin{vmatrix} -\frac{1}{2} & -\frac{1}{2}\sqrt{3} \\ \frac{1}{2}\sqrt{3} & -\frac{1}{2} \end{vmatrix}$	$\begin{vmatrix} -\frac{1}{2} & \frac{1}{2}\sqrt{3} \\ -\frac{1}{2}\sqrt{3} & -\frac{1}{2} \end{vmatrix}$	$\begin{vmatrix} 1 & 0 \\ 0 & -1 \end{vmatrix}$	$\begin{vmatrix} -\frac{1}{2} & -\frac{1}{2}\sqrt{3} \\ -\frac{1}{2}\sqrt{3} & \frac{1}{2} \end{vmatrix}$	$\begin{vmatrix} -\frac{1}{2} & \frac{1}{2}\sqrt{3} \\ \frac{1}{2}\sqrt{3} & \frac{1}{2} \end{vmatrix}$	$\Lambda_3$
$\chi^{\tau_3}$	2	-1	-1	0	0	0	
$\chi^T$	9	0	0	3	3	3	

With the decomposition formula (2.34) it has been found that this representation  $T$  can be decomposed in the following way:

$T(\underline{q}_5) = 3\tau_1 \oplus 3\tau_3$ . Obviously the dispersion relation consists of three non-degenerate  $\tau_1$  branches and three two-fold degenerate  $\tau_3$  branches.

By means of the projection operators (2.36) and equation (2.37) the following symmetry adapted eigenvectors have been obtained

$$E(\Lambda_1) = \begin{vmatrix} a_1 \\ a_1 \\ a_1 \\ b_1 \\ b_1 \\ b_1 \\ c_1 \\ c_1 \\ c_1 \end{vmatrix} \quad E(\Lambda_3 \ 1) = \begin{vmatrix} a_3 \\ a_3 \\ -2a_3 \\ b_3 \\ b_3 \\ -2b_3 \\ c_3 \\ c_3 \\ -2c_3 \end{vmatrix} \quad E(\Lambda_3 \ 2) = \begin{vmatrix} -\sqrt{3} a_3 \\ \sqrt{3} a_3 \\ 0 \\ -\sqrt{3} b_3 \\ \sqrt{3} b_3 \\ 0 \\ -\sqrt{3} c_3 \\ \sqrt{3} c_3 \\ 0 \end{vmatrix} \quad (6.14)$$

$E(\Lambda_1)$  represents longitudinal vibrations,  $E(\Lambda_3 \ 1)$  and  $E(\Lambda_3 \ 2)$  are orthogonal transverse modes.

The equations for the dynamical matrices and basis vectors of the subspaces associated with  $\Lambda_1$  and  $\Lambda_3$  are

for  $\Lambda_1$ :

$$\begin{vmatrix} D_{xx}(11)+2D_{xy}(11)-\omega^2 & \rho_1\{D_{xx}(12)+2D_{xy}(12)\} & \rho_3\{D_{xx}^*(12)+2D_{xy}^*(12)\} \\ \rho_1^*\{D_{xx}^*(12)+2D_{xy}^*(12)\} & D_{xx}(22)+2D_{xy}(22)-\omega^2 & \rho_2\{D_{xx}(24)+2D_{xy}(24)\} \\ \rho_3^*\{D_{xx}(12)+2D_{xy}(12)\} & \rho_2^*\{D_{xx}(24)+2D_{xy}(24)\} & D_{xx}(22)+2D_{xy}(22)-\omega^2 \end{vmatrix} \times \begin{vmatrix} a_1 \\ b_1 \\ c_1 \end{vmatrix} = 0$$

(6.15)

and for  $\Lambda_3$ :

$$\begin{vmatrix} D_{xx}(11)-D_{xy}(11)-\omega^2 & \rho_1\{D_{xx}(12)-D_{xy}(12)\} & \rho_3\{D_{xx}^*(12)-D_{xy}^*(12)\} \\ \rho_1^*\{D_{xx}^*(12)-D_{xy}^*(12)\} & D_{xx}(22)-D_{xy}(22)-\omega^2 & \rho_2\{D_{xx}(24)-D_{xy}(24)\} \\ \rho_3^*\{D_{xx}(12)-D_{xy}(12)\} & \rho_2^*\{D_{xx}(24)-D_{xy}(24)\} & D_{xx}(22)-D_{xy}(22)-\omega^2 \end{vmatrix} \times \begin{vmatrix} a_3 \\ b_3 \\ c_3 \end{vmatrix} = 0$$

(6.16)

[110],  $q = q_4$

The point group of the wave vector is  $C_{2v}$  which has four symmetry elements each forming a class in itself. The group has four one-dimensional irreducible representations given in Table 6.3. The reducible representations  $T(q_4)$  is given by

$$\begin{aligned} T(q_4, R_1) &= \begin{vmatrix} R_1 & 0 & 0 \\ 0 & R_1 & 0 \\ 0 & 0 & R_1 \end{vmatrix} & T(q_4, R_{16}) &= \begin{vmatrix} R_{16} & 0 & 0 \\ 0 & 0 & \rho_2 R_{16} \\ 0 & \rho_2^* R_{16} & 0 \end{vmatrix} \\ T(q_4, R_{28}) &= \begin{vmatrix} R_{28} & 0 & 0 \\ 0 & 0 & \rho_2 R_{28} \\ 0 & \rho_2^* R_{28} & 0 \end{vmatrix} & T(q_4, R_{37}) &= \begin{vmatrix} R_{37} & 0 & 0 \\ 0 & R_{37} & 0 \\ 0 & 0 & R_{37} \end{vmatrix} \end{aligned} \quad (6.17)$$

The characters of this representation have been given in Table 6.3.

Using (2.34) the decomposition is  $T(q_4) = 3\tau_1 \oplus \tau_2 \oplus 2\tau_3 \oplus 3\tau_4$ .

Section 6.2.

Table 6.3. Irreducible representations and characters of the group  $C_{2v}(q_4)$ . The characters of the reducible representation  $T(q_4)$  have been given in the last line.

Kovalev	$R_1$	$R_{16}$	$R_{28}$	$R_{37}$	BSW
$\tau_1$	1	1	1	1	$\Sigma_1$
$\tau_2$	1	1	-1	-1	$\Sigma_2$
$\tau_3$	1	-1	1	-1	$\Sigma_4$
$\tau_4$	1	-1	-1	1	$\Sigma_3$
$\chi^T$	9	-1	1	3	

The symmetry adapted eigenvectors for these irreducible representations have the form

$$\begin{aligned}
 E(\Sigma_1) &= \begin{pmatrix} a_1 \\ a_1 \\ 0 \\ b_1 \\ b_1 \\ c_1 \\ \rho_2^* b_1 \\ \rho_2^* b_1 \\ -\rho_2^* c_1 \end{pmatrix} & E(\Sigma_2) &= \begin{pmatrix} 0 \\ 0 \\ 0 \\ a_2 \\ -a_2 \\ 0 \\ -\rho_2^* a_2 \\ \rho_2^* a_2 \\ 0 \end{pmatrix} \\
 E(\Sigma_4) &= \begin{pmatrix} a_4 \\ -a_4 \\ 0 \\ b_4 \\ -b_4 \\ 0 \\ \rho_2^* b_4 \\ -\rho_2^* b_4 \\ 0 \end{pmatrix} & E(\Sigma_3) &= \begin{pmatrix} 0 \\ 0 \\ a_3 \\ b_3 \\ b_3 \\ c_3 \\ -\rho_2^* b_3 \\ -\rho_2^* b_3 \\ \rho_2^* c_3 \end{pmatrix}
 \end{aligned} \tag{6.18}$$

$E(\Sigma_2)$  and  $E(\Sigma_4)$  represent transverse modes with vibrational amplitudes along  $[1\bar{1}0]$ , whereas  $E(\Sigma_1)$  and  $E(\Sigma_3)$  have both longitudinal and transverse components, the latter along  $[001]$ .

The equations for the dynamical matrices and the basis vectors of the subspaces associated with  $\Sigma_1$ ,  $\Sigma_2$ ,  $\Sigma_4$  and  $\Sigma_3$  are as follows

for  $\Sigma_1$ :

$$\begin{vmatrix} D_{xx}(11)+D_{xy}(11)-\omega^2 & \sqrt{2}\rho_1\{D_{xx}(12)+D_{xy}(12)\} & \rho_1\{D_{xz}(12)-D_{xz}^*(12)\} \\ \sqrt{2}\rho_1^*\{D_{xx}(12)+D_{xy}(12)\} & \left\{ \begin{array}{l} D_{xx}(22)+D_{xy}(22) \\ +D_{xx}(24)+D_{xy}(24) \end{array} \right\} & -\omega^2 & 0 \\ -\rho_1^*\{D_{xz}(12)-D_{xz}^*(12)\} & 0 & D_{zz}(22)-D_{zz}(24)-\omega^2 \end{vmatrix} \times \begin{vmatrix} a_1 \\ b_1 \\ c_1 \end{vmatrix} = 0 \quad (6.19)$$

for  $\Sigma_2$ :

$$\left| D_{xx}(22)-D_{xy}(22)-D_{xx}(24)+D_{xy}(24)-\omega^2 \right| \times \left| a_2 \right| = 0 \quad (6.20)$$

for  $\Sigma_4$ :

$$\begin{vmatrix} D_{xx}(11)-D_{xy}(11)-\omega^2 & \sqrt{2}\rho_1\{D_{xx}(12)-D_{xy}(12)\} \\ \sqrt{2}\rho_1^*\{D_{xx}(12)-D_{xy}(12)\} & D_{xx}(22)-D_{xy}(22)+D_{xx}(24)-D_{xy}(24)-\omega^2 \end{vmatrix} \times \begin{vmatrix} a_4 \\ b_4 \end{vmatrix} = 0 \quad (6.21)$$

for  $\Sigma_3$ :

$$\begin{vmatrix} D_{zz}(11)-\omega^2 & \rho_1\{D_{xz}(12)-D_{xz}^*(12)\} & \sqrt{2}\rho_1 D_{zz}(12) \\ -\rho_1^*\{D_{xz}(12)-D_{xz}^*(12)\} & \left\{ \begin{array}{l} D_{xx}(22)+D_{xy}(22) \\ -D_{xx}(24)-D_{xy}(24) \end{array} \right\} & -\omega^2 & 0 \\ \sqrt{2}\rho_1^* D_{zz}(12) & 0 & D_{zz}(22)+D_{zz}(24)-\omega^2 \end{vmatrix} \times \begin{vmatrix} a_3 \\ b_3 \\ c_3 \end{vmatrix} = 0 \quad (6.22)$$

### 6.2.3. Elastic constants and optic frequencies

If a rigid ion model is assumed the elastic constants, the optic frequencies at  $q = 0$  and a number of zone boundary frequencies can be expressed in terms of interatomic force constants and an effective ion charge which may also serve as a model parameter. Expressions for the

Section 6.2.

elastic constants have been derived by means of the method of long waves described in section 2.2. For the Coulomb contributions to the elastic constants the numerical values given by Rajagopal<sup>17)</sup> have been used. The following expressions have been obtained.

$$c_{11} = \frac{2}{a} \left\{ \alpha_1 + 2\alpha_2 + \alpha_3 + 3.276Z_2^2 \cdot \frac{e^2}{v_a} \right\} \quad (6.23)$$

$$c_{12} = \frac{2}{a} \left\{ -\alpha_1 + 2\beta_1 - \alpha_2 - \beta_2 + 2\gamma_2 - \beta_3 - 5.395Z_2^2 \cdot \frac{e^2}{v_a} \right\} \quad (6.24)$$

$$c_{44} = \frac{2}{a} \left\{ \alpha_1 + \alpha_2 + \beta_2 + \beta_3 - 1.527Z_2^2 \cdot \frac{e^2}{v_a} - \frac{(-\beta_1 + 5.038Z_2^2 \cdot \frac{e^2}{v_a})^2}{\alpha_1 + \alpha_3 + 2\beta_3} \right\} \quad (6.25)$$

Here  $Z_2$  is the positive charge of the magnesium ions in units of  $e$ . These expressions are very similar to those given by Davis *et al.*<sup>9)</sup>; differences are only due to different definitions of the force constants. The derivation by means of the method of long waves was necessary in order to obtain expressions which are consistent with these definitions.

It can be proved that at the centre of the Brillouin zone denoted by  $\Gamma$  (see Fig. 6.1) the decomposition of the representation  $T$  is  $T(\Gamma) = 2\Gamma_{15} \oplus \Gamma'_{25}$ . Both these irreducible representations are three-dimensional and hence there are three different frequencies at  $\Gamma$  each three-fold degenerate. One of the  $\Gamma_{15}$ 's is compatible with the acoustic branches and the other with  $\Delta_5 O_2$  and  $\Delta_1 O$ . It can be found that at the point  $\Gamma$  the branches  $\Delta'_2$  and  $\Delta_5 O_1$  have the same frequencies and that these representations are compatible with  $\Gamma'_{25}$ . In these vibrations only magnesium atoms take part moving in antiphase and so they do not affect the charge density in the crystal. In the optic  $\Gamma_{15}$  modes the magnesium atoms move collectively against the tin atom and if the atoms carry an electric charge a dipole field is thus created.

It has been pointed out by Kittel<sup>18)</sup> and Warren<sup>19)</sup> that a macroscopic depolarization field is associated with the long-wavelength longitudinal modes in an ionic crystal. This field does not have the symmetry of the point  $\Gamma$  and, therefore, immediately outside that point

it causes a splitting of the three-fold degenerate  $\nu(\Gamma_{15}^0)$  into a two-fold degenerate  $\nu_{TO}$  and a non-degenerate  $\nu_{LO}$ . At the point  $\Gamma$  itself there is a discontinuity because there the wavelengths of the normal modes are of the same order of magnitude as the dimensions of the crystal<sup>19)</sup>.

In the limit of long wavelengths the dynamical matrices for the irreducible representations in special directions can be used to obtain explicit expressions for the optic frequencies at the zone centre. This provides the following relations between the optic frequencies at  $q = 0$  and the interatomic force constants and the ion charge.

From (6.10)

$$\omega^2(\Gamma \Delta_1^0) = (2\pi\nu_{LO})^2 = \left(\frac{2}{m_1} + \frac{1}{m_2}\right) (4\alpha_1 + \frac{16\pi}{3} Z_2^2 \cdot \frac{e^2}{v_a}) \quad (6.26)$$

from (6.11)

$$\omega^2(\Gamma \Delta_2') = \frac{1}{m_2} (4\alpha_1 + 4\alpha_3 + 8\beta_3) \quad (6.27)$$

and from (6.21)

$$\omega^2(\Gamma \Delta_5^0) = (2\pi\nu_{TO})^2 = \left(\frac{2}{m_1} + \frac{1}{m_2}\right) (4\alpha_1 - \frac{8\pi}{3} Z_2^2 \cdot \frac{e^2}{v_a}) \quad (6.28)$$

Since  $D_{zz}(12; \underline{q}) = 0$  at the point (001) the matrix in relation (6.10) has a diagonal form and gives directly explicit expressions for the frequencies at the zone boundary associated with the representation  $\Delta_1$ .

$$\omega^2(X \Delta_1^A) = \frac{1}{m_1} (8\alpha_1 + 16\alpha_2 + 17.3344Z_2^2 \cdot \frac{e^2}{v_a}) \quad (6.29)$$

$$\omega^2(X \Delta_1^0) = \frac{1}{m_2} (4\alpha_1 + 4\alpha_3 + 19.374Z_2^2 \cdot \frac{e^2}{v_a}) \quad (6.30)$$

From relation (6.11) it can be found that  $\omega(X \Delta_2')$  is given by

$$\omega^2(X \Delta_2') = \frac{1}{m_2} (4\alpha_1 + 8\beta_3 - 10.7074Z_2^2 \cdot \frac{e^2}{v_a}) \quad (6.31)$$

## Section 6.2.

The last three equations could only be applied after experimental data on the zone boundary frequencies became available.

From Kaplan's<sup>10)</sup> data for  $\nu_{TO}$  and the dielectric constants  $\epsilon_\infty$  and  $\epsilon_0$  Davis *et al.*<sup>9)</sup> calculated  $\nu_{LO} = \frac{1}{2\pi} \omega(\Gamma \Delta_1 0)$  by means of the Lyddane-Sachs-Teller relation  $\nu_{LO}/\nu_{TO} = (\epsilon_0/\epsilon_\infty)^{1/2}$ ; he found  $\nu_{LO} = 6.90 \times 10^{12} \text{ s}^{-1}$ . Using (6.26) and (6.28) it was found from these values that

$\alpha_1 = 1.034 \times 10^4 \text{ dyn.cm}^{-1}$  and  $Z_2 = 0.50$ . The assumption of general forces between nearest neighbours and central forces between next nearest neighbours imposes the conditions  $\beta_2 = 0$ ,  $\alpha_2 = \gamma_2$  and  $\beta_3 = 0$ . By means of (6.23), (6.24) and (6.25) the force constants  $\beta_1$ ,  $\alpha_2$  and  $\alpha_3$  could be calculated from the elastic constants. The values obtained in this way by Davis *et al.*<sup>9)</sup> have been given as model I in Table 6.5. Using these values for the parameters the inelastic structure factors for phonons in the symmetry directions have been evaluated by means of expression (4.18). The values for the scattering amplitudes are  $b_{Sn} = 0.61 \times 10^{-12} \text{ cm}$  and  $b_{Mg} = 0.52 \times 10^{-12} \text{ cm}$ <sup>20)</sup>. For simplicity it has been assumed that the Debye-Waller factors are equal to unity. The structure factors have been used as a first guide for the design of neutron scattering experiments.

6.3. Results and analysis

The magnesium stannide specimen was a cylindrical single crystal of about 3.5 cm length and 2 cm diameter. It had been grown according to the Bridgman method at the Metaal Instituut TNO, Delft. The orientation of the cylinder axis was within  $2^\circ$  from the  $[211]$ -direction which is in perfect agreement with the preference for orientation along  $[211]$  as has been observed by Lichter<sup>21)</sup>. The mosaic spread of the crystal was about  $28'$  full width at half maximum.

Nearly all experiments have been carried out with the plane  $(1\bar{1}0)$  horizontal; only phonons of the  $\Sigma_4 A$  and  $\Sigma_4 0$  branches were measured with the  $(001)$  plane horizontal. It has been impossible to determine the frequencies of phonons belonging to the branches  $\Lambda_1 0_2$  and  $\Sigma_4 0$ , because either the inelastic structure factors were unfavourable or the observations were obscured by peaks due to other branches. It will be shown that the structure factor does not allow the observation of

Table 6.4. Frequencies ( $10^{12} \text{ s}^{-1}$ ) of normal modes in magnesium stannide measured in the symmetry directions.

00z						
$\frac{a}{2\pi} \cdot q$	$\Delta_5 A$	$\Delta_1 A$	$\Delta_5 O_2$	$\Delta_2'$	$\Delta_5 O_1$	$\Delta_1 O$
0			5.70±0.20	6.40±0.15*	6.40±0.15*	7.00±0.20*
0.05			5.50±0.20			
0.10			5.50±0.20			
0.20		1.40±0.15	5.50±0.15	6.10±0.20	6.60±0.15	7.00±0.15
0.25	1.15±0.03	1.80±0.08				
0.30	1.28±0.03	2.10±0.10	5.30±0.15	6.00±0.20		
0.35	1.44±0.03	2.30±0.10				
0.40	1.60±0.03	2.70±0.10	5.20±0.15	6.00±0.20	6.50±0.20	7.00±0.15
0.45	1.72±0.03	2.93±0.07				
0.50	1.82±0.03	3.10±0.10	5.20±0.10	5.60±0.20		
0.55	1.92±0.03	3.25±0.06				
0.60	2.00±0.03	3.42±0.06	4.90±0.15	5.30±0.20	6.45±0.15	7.95±0.15
0.65	2.10±0.04	3.50±0.15				
0.70	2.12±0.04	3.65±0.10	4.70±0.15	5.00±0.15		
0.75	2.22±0.04	3.80±0.15				
0.80	2.23±0.05		4.50±0.10	4.70±0.15	6.55±0.15	8.60±0.20
0.85	2.30±0.07	3.80±0.08				
0.90	2.30±0.07	3.75±0.10	4.40±0.15	4.50±0.15		
0.95	2.40±0.10					
1.00	2.30±0.10*	3.85±0.10*	4.30±0.15*	4.60±0.12*	6.50±0.20	8.80±0.20*

z00							
$\frac{a}{2\pi} \cdot q$	$\Sigma_4 A$	$\Sigma_3 A$	$\Sigma_1 A$	$\Sigma_3 O_2$	$\Sigma_3 O_1$	$\Sigma_1 O_2$	$\Sigma_1 O_1$
0				5.70±0.20**	6.40±0.15*	6.40±0.15*	7.00±0.20*
0.10					6.65±0.20		
0.20	0.80±0.10		1.48±0.08	5.60±0.15	6.45±0.15	6.40±0.15	7.10±0.20
0.25	1.00±0.06	1.20±0.10	1.85±0.10				
0.30	1.20±0.05	1.37±0.05	2.05±0.05	5.60±0.15	6.60±0.15	6.40±0.15	
0.35	1.30±0.04	1.55±0.03	2.35±0.07				
0.40	1.50±0.03	1.70±0.03	2.50±0.07	5.48±0.15	6.40±0.15	6.50±0.15	7.50±0.15
0.45	1.60±0.03	1.90±0.03	2.85±0.10				
0.50	1.70±0.03	2.05±0.03	2.90±0.12		6.20±0.15	6.30±0.15	7.40±0.15
0.55	1.76±0.03	2.23±0.03	3.20±0.15				
0.60	1.98±0.05	2.35±0.03	3.23±0.15	5.25±0.15	6.10±0.15	6.45±0.20	7.60±0.20
0.65	2.00±0.05	2.50±0.04					
0.70	2.03±0.05	2.60±0.05	3.30±0.15	5.00±0.15	5.90±0.15		
0.75	2.12±0.07	2.70±0.05					
0.80	2.15±0.10	2.85±0.07	3.35±0.20	4.80±0.15	5.60±0.15		7.70±0.20
0.85		2.86±0.07					
0.90	2.20±0.10	2.95±0.07		4.75±0.12			
0.95		3.10±0.12					
1.00	2.24±0.10	3.10±0.15	3.27±0.10	4.70±0.15	5.40±0.15		8.20±0.20
1.10	2.24±0.10	3.25±0.10	2.85±0.10	4.80±0.15			
1.20	2.20±0.10	3.45±0.15	2.60±0.10	4.60±0.15	5.10±0.15		8.60±0.20
1.30	2.20±0.15	3.60±0.15	2.25±0.10	4.65±0.15			
1.414	2.30±0.10*	3.85±0.10*	2.30±0.10*	4.30±0.15*	4.60±0.12*	6.50±0.20**	8.80±0.20*

z0z					
$\frac{a}{2\pi} \cdot q$	$\Lambda_3 A$	$\Lambda_1 A$	$\Lambda_3 O_2$	$\Lambda_3 O_1$	$\Lambda_1 O_1$
0			5.70±0.20	6.40±0.15*	7.00±0.20*
0.20				6.50±0.20	7.40±0.25
0.25	1.04±0.03	1.85±0.06			
0.30	1.16±0.03	2.20±0.05	5.80±0.25	6.40±0.20	
0.35	1.32±0.03	2.52±0.06			
0.40	1.40±0.03	2.80±0.05	5.70±0.20	6.40±0.15	7.30±0.20
0.45	1.50±0.03	3.00±0.05			
0.50	1.60±0.03	3.20±0.08	5.60±0.20	6.30±0.15	
0.55		3.35±0.12			
0.60	1.67±0.04	3.60±0.10	5.65±0.20	6.40±0.15	7.25±0.25
0.65	1.68±0.04				
0.70	1.70±0.04	3.65±0.10	5.60±0.20	6.30±0.15	7.70±0.25
0.75	1.70±0.04				
0.80	1.70±0.07	3.70±0.15	5.70±0.20	6.25±0.15	7.45±0.20
0.866	1.70±0.07		5.80±0.20	6.20±0.15	7.50±0.20

\* average of observations from different branches

\*\* copied from another branch

Section 6.3.

phonons of the  $\Sigma_2$  branch in either of the two symmetry planes. Frequencies for all other branches in the three symmetry directions observed for selected wave vectors have been given in Table 6.4; they have been plotted versus the reduced wave vector in Fig. 6.2.

As soon as the first zone-boundary frequencies at (001) became available these data could be used to calculate a set of parameters.  $\alpha_2$  could be obtained from  $\nu(X \Delta_1 A)$  by means of (6.29) and  $\alpha_3$  and  $\beta_3$  from  $\nu(\Gamma \Delta'_2)$  and  $\nu(X \Delta'_2)$  by means of (6.30) and (6.31), respectively. With these values and assuming  $\alpha_2 = \gamma_2, \beta_1$  and  $\beta_2$  have been calculated from  $c_{12}$  and  $c_{44}$  by means of relations (6.24) and (6.25). The parameters calculated in this way have been tabulated as model II in Table 6.5. The parameters of rigid ion model III, also given in Table 6.5, have been obtained by fitting the model to the experimental frequencies by trial. The dispersion relation calculated from this last set of parameters has been given in Fig. 6.2. The velocities of sound in the three

Table 6.5. Model parameters for magnesium stannide. Models I, II and III are rigid ion models and IV is a shell model. The short-range force constants are in units of  $10^4 \text{ dyn.cm}^{-1}$ .

	Model I Davis <i>et al.</i> <sup>9)</sup>	Model II with zone boundary freq.	Model III fitted by trial	Model IV
$\alpha_1$	+1.034	+1.034	+1.034	+1.57
$\beta_1$	+0.84	+1.39	+1.05	+3.06
$\alpha_2$	+0.46	+0.15	+0.32	+0.43
$\beta_2$	0	+0.80	+0.30	+0.53
$\alpha_3$	+0.60	+0.63	+0.63	+0.08
$\beta_3$	0	-0.01	-0.01	0
$Z_{\text{Mg}} (e)$	+0.50	+0.50	+0.50	+0.93
$\Pi_{\text{Sn}} (v_a)$				+0.036
$d_{\text{Sn}} (e)$				+0.723

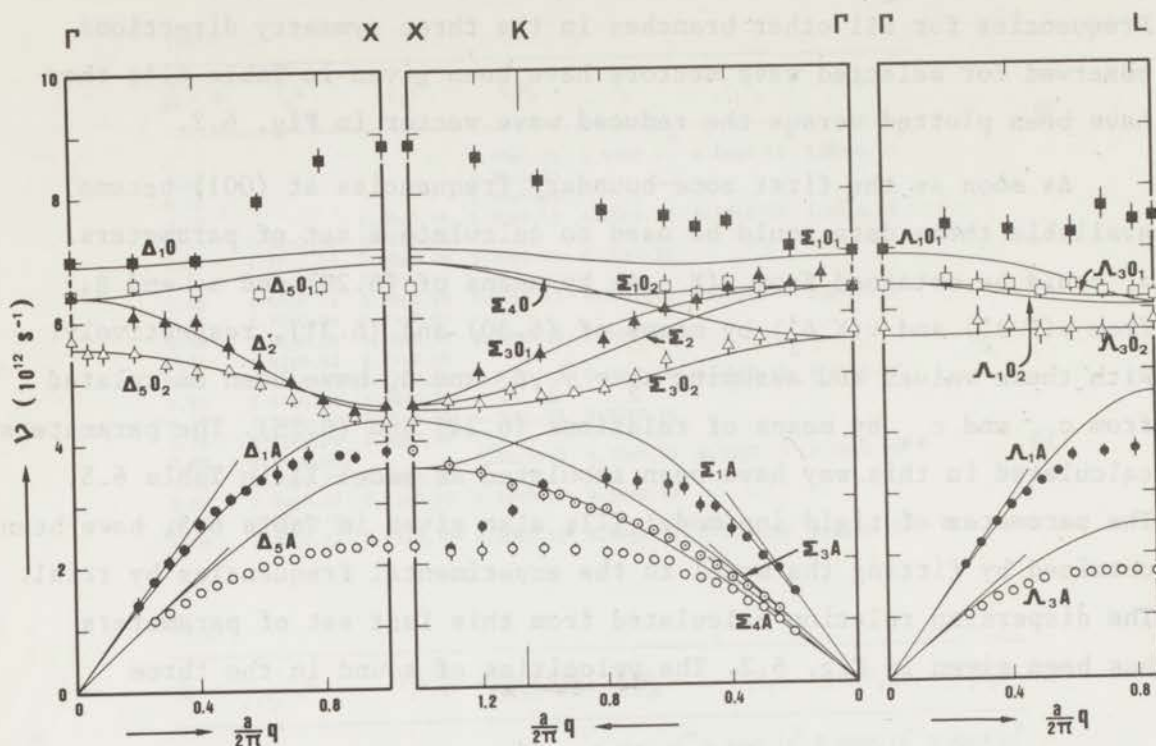
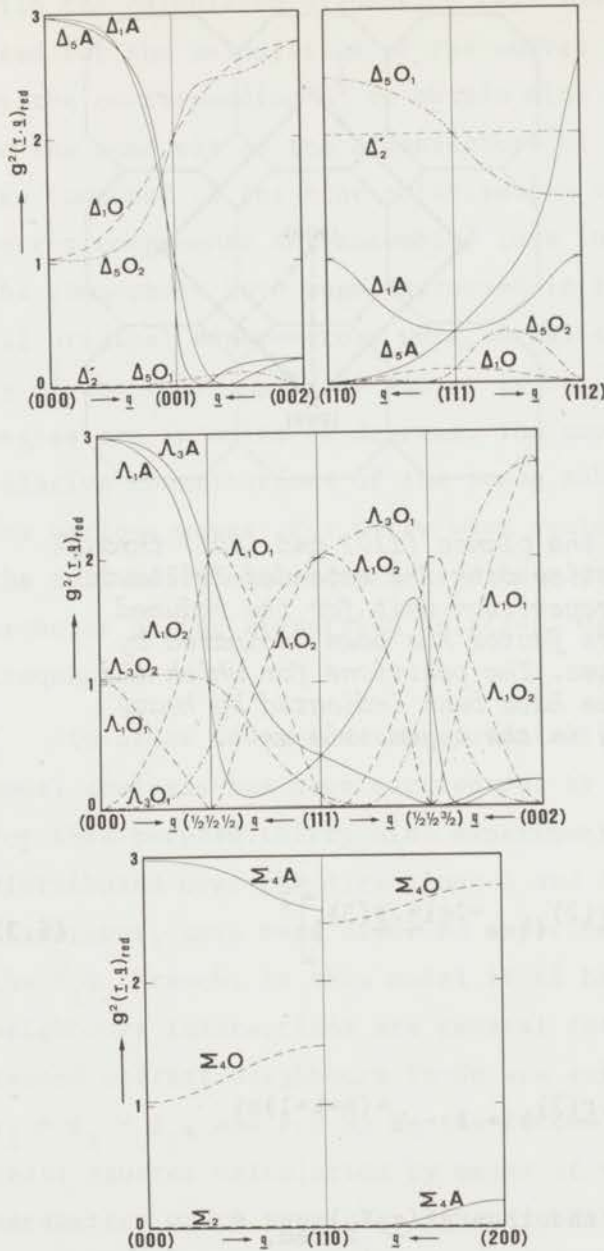


Fig. 6.2. Dispersion relation for magnesium stannide. The solid lines have been calculated according to rigid ion model III. The straight lines drawn from the origin represent the velocities of sound. The representation labels refer to the text. For  $\Delta$  and  $\Lambda$  the open points represent transverse modes and the closed points are longitudinal modes.

directions are represented by straight lines drawn from the origin. Although in general the inelastic structure factors as formulated in section 4.2. are not very sensitive to the parameter values they were calculated anew now using this last set of values. The reduced structure factors have been plotted versus wave vector in Fig. 6.3. for all branches in the three symmetry directions which satisfy the condition for reduction of the inelastic structure factor. They have been given for wave vectors within the repetition unit for the reduced structure factor only. The intersections of this repetition unit with the planes  $(1\bar{1}0)$  and  $(001)$  have been sketched in Fig. 6.4.

The  $\Sigma_2$ -branch cannot be observed in either  $(001)$  or  $(1\bar{1}0)$ . From the shape of  $E(\Sigma_2)$  in (6.18) it is seen that it is perpendicular to

Section 6.3.



(110) and, therefore, the structure factor is equal to zero for  $Q$  in that plane. At the end of chapter IV it has been mentioned that the inelastic structure factor will be constant within a repetition unit if the eigenvector of the branch is composed of only contributions from atoms connected by a centre of symmetry. These constant values calculated by means of (4.17) turn out to be equal to zero for  $Q$  in the (001) plane:

Fig. 6.3.

Reduced inelastic structure factors for magnesium stannide calculated according to rigid ion model III.

$$\begin{aligned}
 g^2(\underline{r}, \Sigma_2) &= \frac{b^2}{m_2} \left[ Q \cdot \begin{vmatrix} a_2 \\ a_2 \\ 0 \end{vmatrix} e^{-i(2\pi \underline{r} + \underline{q}) \cdot \underline{r}(2)} + Q \cdot -\rho_2^* \begin{vmatrix} a_2 \\ a_2 \\ 0 \end{vmatrix} e^{-i(2\pi \underline{r} + \underline{q}) \cdot \underline{r}(4)} \right]^2 \\
 &= \frac{b^2}{m_2} \left[ Q \cdot \begin{vmatrix} a_2 \\ a_2 \\ 0 \end{vmatrix} \rho_1 \left\{ e^{-2\pi i \underline{r} \cdot \underline{r}(2)} - \rho_2^* e^{-2\pi i \underline{r} \cdot \underline{r}(4)} \rho_2 \right\} \right]^2 \quad (6.32)
 \end{aligned}$$

$\rho_2$  and  $\rho_1$  have been defined in connection with expressions (6.7) and (6.12), respectively.

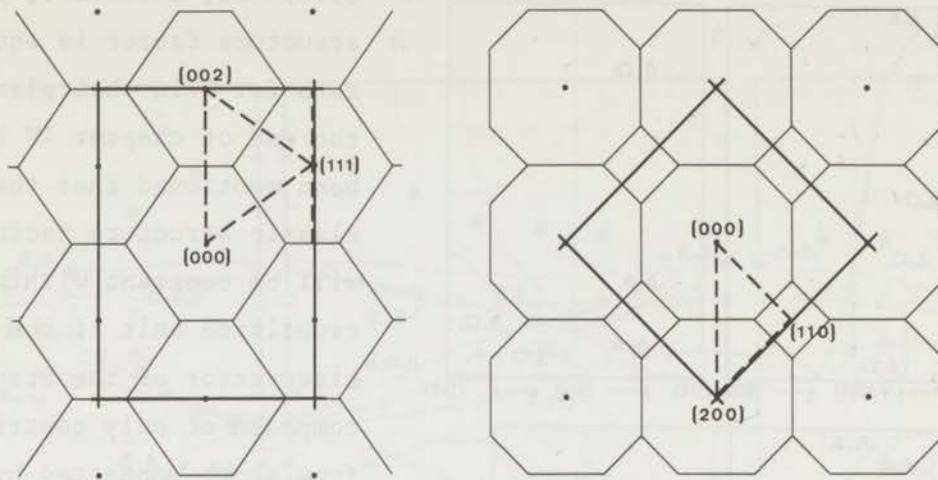


Fig. 6.4. Intersections of the planes  $(\bar{1}\bar{1}0)$  and  $(001)$  through the reciprocal lattice with the extended Brillouin zone scheme. The repetition unit for the reduced inelastic structure factor has been indicated by means of heavy lines. The positions for which the periodicity applies have been indicated by heavy broken lines in the asymmetric unit.

Hence

$$g^2(\underline{\tau}, \underline{\Sigma}_2)_{\text{red.}} = \frac{1}{2} \left[ \rho_1 e^{-2\pi i \underline{\tau} \cdot \underline{r}(2)} (1 - e^{-2\pi i \underline{\tau} \cdot \underline{r}(3)}) \right]^2 \quad (6.33)$$

Since

$$\underline{\tau} = \frac{1}{a}(h, k, l) \text{ is } (1 - e^{-2\pi i \underline{\tau} \cdot \underline{r}(3)}) = 1 - e^{-(h+k+1)\pi i}$$

In the plane  $(001)$   $h+k+1$  is even and thus  $g^2(\underline{\tau}, \underline{\Sigma}_2)_{\text{red.}} = 0$ .

Consequently, this branch can only be measured in zones out of the symmetry planes.

It has been pointed out in section 2.1. that the eigenvectors of a dynamical matrix are composed of a number of polarization vectors  $\underline{\xi}(\kappa, \underline{q}j)$  defined by (2.7). If these polarization vectors are divided by  $\frac{1}{\kappa} m$  the corresponding amplitude vectors  $\underline{\eta}(\kappa, \underline{q}j)$  are obtained each of which consists of three components according to the Cartesian coordinates. The nine components of each of the eigenvectors which are associated

## Section 6.3.

with the calculated dispersion relation of Fig. 6.2 and which have been used for the calculation of the curves in Fig. 6.3, have been divided by the corresponding  $m_{\kappa}^{\frac{1}{2}}$  to obtain nine amplitude vector components. In the same way as the eigenvectors of the dynamical matrix are composed of the nine polarization vector components, these amplitude vector components are assembled to a full amplitude vector. In Table 6.6 the components have been expressed in terms of argument and phase angle. All original eigenvectors were normalized to 100 but due to the correction by  $m_{\kappa}^{\frac{1}{2}}$  the full amplitude vector is not normalized any longer. The phase angles are in units of degrees. The amplitude vectors demonstrate the relative contributions of the three sublattices to the amplitudes of the various waves. For a few wave vectors in the symmetry directions the full amplitude vectors have been presented in Table 6.6 for all branches of the dispersion relation together with the corresponding frequencies.

In order to include the polarizability of the tin atoms a shell model analysis has been carried out by means of a least squares calculation<sup>22)</sup>. For this purpose thirty nine experimental frequencies homogeneously distributed over the directions  $\Delta$  and  $\Lambda$  and over the branches in these directions, have been used. No experimental results were available for the  $\Lambda_1 0_2$  branch. In this model IV it has been assumed that the nearest neighbours interactions are general forces, the interactions between second nearest neighbours Sn-Sn are axially symmetric so that  $\gamma_2 = \alpha_2 - \beta_2$ , and for Mg-Mg the forces are central and thus  $\beta_3 = 0$ . The least squares calculation by means of this model provided a set of parameters which have been given in Table 6.5 and which have been used to calculate the dispersion relation in the three symmetry directions. Together with the experimental data these dispersion curves have been plotted in Fig. 6.5. By means of the relations (3.20) it can be found that the polarizability values for tin correspond to a shell charge of  $-2.09e$  and a force constant between the core and the shell of  $23.8 \times 10^4 \text{ dyn.cm}^{-1}$ .

Table 6.6. Full amplitude vectors in magnesium stannide for normal modes of all branches in the symmetry directions and calculated for rigid ion model III. Each vector has been given by two columns of which the first gives its arguments of the nine components and the second their phase angles (degrees). At the head of each pair of columns the corresponding frequency has been given.

[00c]	j	$\Delta_1^0$	$\Delta_1^A$	$\Delta_2^*$	$\Delta_{3,1}^0$	$\Delta_{3,2}^0$	$\Delta_3^A$	$\Delta_{3,1}^0$	$\Delta_{3,2}^0$	$\Delta_3^A$	
$\frac{\omega}{2\pi} \cdot q=0$	v(gj)	6.90	0	6.41	6.41	5.57	0	6.41	5.57	0	
		0 0	0 0	0 0	0 0	27 0	42 0	0 0	27 180	42 180	
		0 0	0 0	0 0	0 0	0 0	0 0	0 0	27 0	42 0	
		38 0	60 0	0 0	0 0	0 0	0 0	0 0	0 0	0 0	
		0 0	0 0	0 0	79 180	66 180	42 0	79 180	66 0	42 180	
		0 0	0 0	0 0	79 180	66 180	42 0	79 0	66 180	42 0	
		0 0	0 0	0 0	0 0	0 0	0 0	0 0	0 0	0 0	
		94 180	60 0	111 0	79 0	66 180	42 0	79 0	66 0	42 180	
		0 0	0 0	0 0	79 0	66 180	42 0	79 180	66 180	42 0	
		94 180	60 0	111 180	0 0	0 0	0 0	0 0	0 0	0 0	
$\frac{\omega}{2\pi} \cdot q=0.5$		7.02	3.05	5.55	6.67	5.20	2.24	6.67	5.20	2.24	
		0 0	0 0	0 0	13 41	24 23	42 206	13 221	24 203	42 26	
		0 0	0 0	0 0	13 41	24 23	42 206	13 41	24 23	42 206	
		30 0	65 315	0 0	0 0	0 0	0 0	0 0	0 0	0 0	
		0 0	0 0	0 0	76 182	70 263	42 233	76 169	70 53	42 90	
		0 0	0 0	0 0	76 182	70 263	42 233	76 349	70 233	42 270	
		0 0	0 0	0 0	0 0	0 0	0 0	0 0	0 0	0 0	
		101 225	47 0	111 0	76 79	70 323	42 0	76 92	70 173	42 143	
		0 0	0 0	0 0	76 79	70 323	42 0	76 272	70 353	42 323	
		101 315	47 0	111 270	0 0	0 0	0 0	0 0	0 0	0 0	
$\frac{\omega}{2\pi} \cdot q=1.0$		7.12	4.34	4.51	6.88	4.60	3.56	6.88	4.60	3.56	
		0 0	0 0	0 0	16 0	0 0	48 0	16 180	0 0	48 180	
		0 0	0 0	0 0	16 0	0 0	48 0	16 0	0 0	48 0	
		0 0	71 0	0 0	0 0	0 0	0 0	0 0	0 0	0 0	
		0 0	0 0	0 0	75 180	79 0	25 0	75 180	79 180	25 0	
		0 0	0 0	0 0	75 180	79 0	25 0	75 0	79 0	25 180	
		0 0	0 0	0 0	0 0	0 0	0 0	0 0	0 0	0 0	
		111 0	0 0	111 0	75 180	79 180	25 0	75 180	79 0	25 0	
		0 0	0 0	0 0	75 180	79 180	25 0	75 0	79 180	25 180	
		111 180	0 0	111 0	0 0	0 0	0 0	0 0	0 0	0 0	
[c<0]	j	$\Gamma_1^0$	$\Gamma_1^A$	$\Gamma_2^*$	$\Gamma_{3,1}^0$	$\Gamma_{3,2}^0$	$\Gamma_3^A$	$\Gamma_{3,1}^0$	$\Gamma_{3,2}^0$	$\Gamma_3^A$	
	$\frac{\omega}{2\pi} \cdot q=0$	v(gj)	6.90	6.41	0	6.41	6.41	5.57	0	5.57	0
			27 0	0 0	42 0	0 0	0 0	0 0	0 0	27 180	42 180
			0 0	0 0	0 0	0 0	0 0	0 0	0 0	0 0	0 0
			66 180	0 0	42 0	79 0	79 0	0 0	0 0	66 180	42 0
			66 180	0 0	42 0	79 180	79 0	0 0	94 180	60 0	0 0
			0 0	111 0	0 0	0 0	0 0	0 0	0 0	66 180	42 0
			66 180	0 0	42 0	79 180	79 180	0 0	0 0	66 0	42 180
			66 180	0 0	42 0	79 0	79 0	0 0	94 180	60 0	0 0
			0 0	111 180	0 0	0 0	0 0	0 0	0 0	0 0	0 0
		0 0	0 0	0 0	0 0	0 0	0 0	0 0	0 0	0 0	
$\frac{\omega}{2\pi} \cdot q=0.70$		6.83	6.33	3.98	5.58	5.96	4.94	2.94	6.20	2.53	
		14 0	8 91	48 1	0 0	0 0	0 0	0 0	22 0	45 271	
		14 0	8 91	48 1	0 0	0 0	0 0	0 0	22 180	45 91	
		0 0	0 0	0 0	0 0	27 0	28 1	60 271	0 0	0 0	
		16 269	75 0	18 90	79 0	71 179	27 0	20 270	71 269	34 0	
		16 269	75 0	18 90	79 180	71 179	27 0	20 270	71 89	34 180	
		104 179	29 90	26 0	0 0	21 269	95 270	54 0	0 0	0 0	
		16 87	75 178	18 268	79 358	71 177	27 358	20 268	71 87	34 178	
		16 87	75 178	18 268	79 178	71 177	27 358	20 268	71 267	34 358	
		104 177	29 88	26 358	0 0	21 87	95 88	54 178	0 0	0 0	
$\frac{\omega}{2\pi} \cdot q=1.414$		7.12	6.88	3.56	4.60	4.60	4.51	4.34	6.88	3.56	
		0 0	16 0	48 0	0 0	0 0	0 0	0 0	16 0	48 180	
		0 0	16 0	48 0	0 0	0 0	0 0	0 0	16 180	48 0	
		0 00	0 0	0 0	0 0	0 0	0 0	71 0	0 0	0 0	
		0 0	75 180	25 0	79 0	79 0	0 0	0 0	75 0	25 0	
		0 0	75 180	25 0	79 180	79 0	0 0	0 0	75 180	25 180	
		0 0	75 180	25 0	0 0	0 0	111 0	0 0	0 0	0 0	
		111 0	0 0	0 0	79 180	79 180	0 0	0 0	75 0	25 0	
		0 0	75 180	25 0	79 0	79 180	0 0	0 0	75 180	25 180	
		111 180	0 0	0 0	0 0	0 0	111 0	0 0	0 0	0 0	
[c<c]	j	$\Lambda_1^0$	$\Lambda_1^A$	$\Lambda_2^*$	$\Lambda_{3,1}^0$	$\Lambda_{3,2}^0$	$\Lambda_3^A$	$\Lambda_{3,1}^0$	$\Lambda_{3,2}^0$	$\Lambda_3^A$	
	$\frac{\omega}{2\pi} \cdot q=0$	v(gj)	6.90	6.41	0	6.41	5.57	0	6.41	5.57	0
			22 0	0 0	35 0	0 0	16 0	24 0	0 180	27 180	42 180
			22 0	0 0	35 0	0 0	16 0	24 0	0 0	27 0	42 0
			22 0	0 0	35 0	0 180	31 180	49 180	0 0	0 0	0 0
			54 180	64 0	35 0	45 180	38 180	24 0	79 0	66 0	42 180
			54 180	64 0	35 0	45 180	38 180	24 0	79 180	66 180	42 0
			54 180	64 0	35 0	91 0	77 0	49 180	0 0	0 0	0 0
			54 180	64 180	35 0	45 0	38 180	24 0	79 180	66 0	42 180
			54 180	64 180	35 0	45 0	38 180	24 0	79 0	66 180	42 0
		54 180	64 180	35 0	91 180	77 0	49 180	0 0	0 0	0 0	
$\frac{\omega}{2\pi} \cdot q=0.4$		6.71	6.23	2.78	6.30	5.62	1.61	6.30	5.62	1.61	
		20 13	6 33	35 155	6 303	14 253	25 184	11 123	23 73	43 4	
		20 13	6 33	35 155	6 303	14 253	25 184	11 303	23 253	43 184	
		20 13	6 33	35 155	12 123	27 73	50 0	4 0	0 0	0 0	
		56 217	63 332	33 200	44 265	40 119	23 257	77 85	70 299	40 77	
		56 217	63 332	33 200	44 265	40 119	23 257	77 265	70 119	40 257	
		56 217	63 332	33 200	89 85	80 299	46 77	0 0	0 0	0 0	
		56 58	63 343	33 0	44 231	40 278	23 0	77 51	70 98	40 180	
		56 58	63 343	33 0	44 231	40 278	23 0	77 231	70 278	40 0	
		56 58	63 343	33 0	89 51	80 98	46 180	0 0	0 0	0 0	
$\frac{\omega}{2\pi} \cdot q=0.866$		6.07	6.07	4.64	6.16	5.64	2.50	6.16	5.64	2.50	
		0 0	0 0	41 180	13 0	0 180	26 0	22 180	0 0	43 180	
		0 0	0 0	41 180	13 0	0 180	26 0	22 0	0 180	43 0	
		0 0	0 0	41 180	26 180	0 0	52 180	0 0	0 0	0 0	
		91 180	0 0	1 180	41 0	45 0	20 180	71 0	79 180	35 0	
		91 180	0 0	1 180	41 0	45 0	20 180	71 0	79 0	35 180	
		91 180	0 0	1 180	82 180	91 180	40 0	0 0	0 0	0 0	
		0 0	91 0	1 0	41 180	45 0	20 0	71 0	79 180	35 180	
		0 0	91 0	1 0	41 180	45 0	20 0	71 180	79 0	35 0	
		0 0	91 0	1 0	82 0	91 180	40 180	0 0	0 0	0 0	

## Section 6.4.

## 6.4. Discussion

The magnesium stannide results show some resemblance to those of the isostructural uranium dioxide<sup>13)</sup>. Comparing the two dispersion relations it is seen that there are a few differences as regards the applicability of the rigid ion model. Firstly, it seems characteristic for the rigid ion model with a limited number of short-range interactions that it cannot properly represent the shape of the transverse acoustic branches in the outer half of the Brillouin zone. They show a gradual rise from the origin corresponding to the velocities of sound and a rather sudden flattening in the second half of the branch. If calculations according to the rigid ion model for  $Mg_2Sn$  are fitted to the velocity-of-sound values they end up with far too high frequencies at the zone boundary as can be seen for  $\Delta_5A$ ,  $\Sigma_4A$  and  $\Lambda_3A$  in Fig. 6.2. In this respect the agreement for  $UO_2$  is much better. A second difference in the dispersion relations of the two compounds is the much stronger rise in  $Mg_2Sn$  of the  $\Delta_1O$ - and  $\Sigma_1O_1$ -frequencies for wave vectors approaching the point X. Taking these two differences into account it can be seen that the rigid ion model is much less satisfactory for  $Mg_2Sn$  than it is for  $UO_2$ .

The numerical values for the full amplitude vectors calculated according to rigid ion model III have been tabulated in Table 6.6. Obviously, for  $q = 0$  in the acoustic modes all three atoms vibrate in phase with the same amplitude. Apart from that, however, there are a few noteworthy properties of these waves. Firstly, the considerations in section 6.2.3. on the  $\Delta_1O$ - and  $\Delta_5O_2$ -modes at  $q = 0$  are seen to be confirmed here. The magnesium atoms move collectively against the tin atom with amplitudes having a ratio equal to  $m_{Sn}/2m_{Mg}$ . Secondly, all  $\Sigma_1$ - and  $\Sigma_3$ -modes are found to be purely longitudinal or transverse with the amplitude in the  $(1\bar{1}0)$  plane at the centre and at the boundary of the zone, but of a mixed type in between. Finally, the accidental degeneracy of  $\Lambda_1O_1$  and  $\Lambda_1O_2$  at the zone boundary causes an unrealistic shape of the amplitudes. The real amplitude vector will be a linear combination of these two.

Comparison of Fig. 6.2 and Fig. 6.5 shows that a simple eight-parameter shell model including polarization of the tin atoms provides a significant improvement of the fit with the experimental data upon the rigid ion model. The shapes of  $\Delta_1 0$  and  $\Sigma_1 0_1$  are in much better agreement with the data while also the overall fit of the acoustic branches has been strongly improved. This might be an indication that the axially asymmetric or noncentral components of the short-range interactions between second nearest neighbours are of less importance compared to the long-range interactions associated with a dipole moment at the tin atoms.

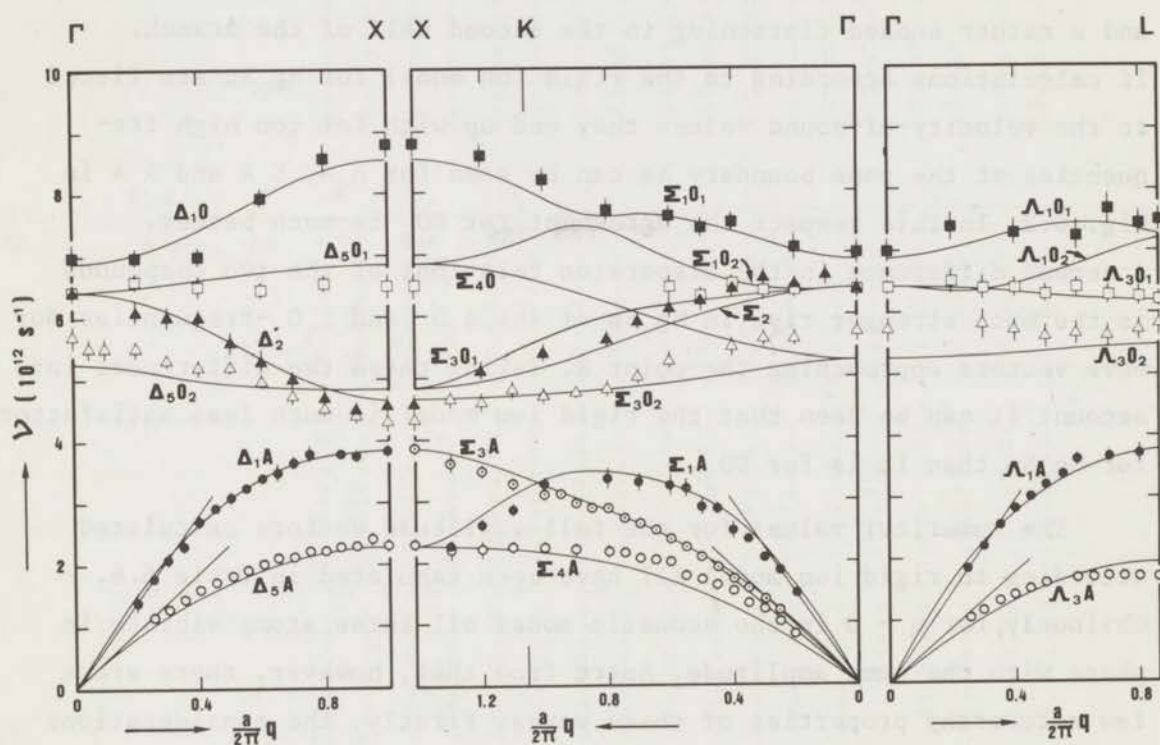


Fig. 6.5. Dispersion relation for magnesium stannide. The solid lines have been calculated according to the shell model IV. See also Fig. 6.2.

In Table 6.7 the elastic constants and the frequency ratio for the infra-red active modes have been presented as they have been obtained from experiments and from the calculations according to the models III and IV. Apart from a 10% difference for  $c_{11}$  in each of the models and a serious disagreement of  $c_{12}$  in the shell model, the comparison is good.

## Section 6.4.

Table 6.7. Elastic constants (in units of  $10^{11}$  dyn.cm<sup>-2</sup>) and infra-red-frequency ratio from experiments and calculations according to the models III and IV.

	Experimental	Rigid ion model III	Shell model IV	
$c_{11}$	8.24 <sup>9)</sup>	7.4	9.0	
$c_{12}$	2.08 <sup>9)</sup>	2.1	5.5	
$c_{44}$	3.66 <sup>9)</sup>	3.7	3.4	
$\nu_{LO}/\nu_{TO}$	1.23	1.24	1.30	1.24 from LST relation

The infra-red-frequency ratio calculated from the high- and low-frequency dielectric constants by means of the LST relation, has also been given and compares nicely with the experimental value.

Using the Clausius Mosotti relation

$$\frac{4\pi}{3} \Pi = \frac{\epsilon_{\infty} - 1}{\epsilon_{\infty} + 2}$$

the electronic polarizability of the tin atoms has been calculated from Kahan's <sup>10)</sup> value of the high-frequency dielectric constant and was found to be  $\Pi_{Sn} = +0.198$  compared to  $+0.036$  according to the shell model; both values are in units of  $\nu_a$ . The shell model value is rather small for the negatively charged tin ion.

From the Figures 6.2 and 6.5 it can be seen that the shell model fits much better to the observed zone-boundary frequencies than does the rigid ion model. Thus, if second-order Raman scattering would have been measured, which is not the case, the frequencies would agree best with the shell model.

The charge of the magnesium ion has been found to be  $0.93e$  which is about a half of that in a fully ionic compound but it is approximately double the value obtained from the infra-red frequencies using the rigid

ion model. This is opposite to the conclusion by Davis et al. 9), but for some of the branches their calculations show appreciable discrepancies with the present results. The value for the ionic charge seems to indicate that the forces in  $Mg_2Sn$  are at least for an appreciable fraction of ionic nature.

The comparison of the experimental results to the calculated curves in Fig. 6.5 demonstrates that also the eight-parameter shell model does not represent the dispersion relation in great detail. However, it seems that at least some of the physical significance has been retained in the relatively small number of parameters of this model. Furthermore, the model may be useful for a reasonable phenomenological representation.

Note added in proof:

In the course of the investigation the author learned from dr R.J. Kearney of the University of Idaho that inelastic neutron scattering measurements have been performed on magnesium stannide at the National Reactor Testing Site, Idaho Falls. The results of this work have quite recently appeared in print as

R.J. Kearney, T.G. Worlton, R.E. Schmunk, J.Phys.Chem.Solids 31 (1970), 913.

R.J. Kearney, T.G. Worlton, R.E. Schmunk, J.Phys.Chem.Solids 31 (1970), 1085.

In this work essentially the same models were used as in the present investigation but with more parameters. The author intends to compare the results of both investigations in a subsequent paper.

References

- 1) R.F. Blunt, H.P.R. Frederikse, W.R. Hosler, Phys. Rev. 100 (1955), 663.
- 2) H.G. Lipson, A. Kahan, Phys. Rev. A133 (1964), 800.
- 3) M.Y. Au-Yang, M.L. Cohen, Phys. Rev. 178 (1969), 1358.
- 4) A. Stella, D.W. Lynch, J. Phys. Chem. Solids, 25 (1964), 1253.
- 5) L.A. Lott, D.W. Lynch, Phys. Rev. 141 (1966), 681.
- 6) P.M. Lee, Phys. Rev. A135 (1964), 1110.
- 7) N.O. Folland, Phys. Rev. 158 (1967), 764.
- 8) W.J. Scouler, Phys. Rev. 178 (1969), 1353.
- 9) L.C. Davis, W.B. Whitten, G.C. Danielson, J. Phys. Chem. Solids 28 (1967), 439.
- 10) A. Kahan, H.G. Lipson, E.V. Loewenstein, 7<sup>th</sup> Int. Conf. Physics of Semiconductors, Proc. Conf. Paris (1964), 1067.
- 11) R. Srinivasan, Proc. Phys. Soc. 72 (1958), 566.
- 12) S. Ganesan, R. Srinivasan, Can. J. Phys. 40 (1962), 74.
- 13) G. Dolling, R.A. Cowley, A.D.B. Woods, Can. J. Phys. 43 (1965), 1397.
- 14) A.A. Maradudin, S.H. Vosko, Rev. Mod. Phys. 40 (1968), 1.
- 15) O.V. Kovalev, Irreducible Representations of the Space Groups Academy of Sciences USSR Press, Kiev 1961; English translation: Gordon and Breach Science Publishers, New York, 1965.
- 16) L.P. Bouckaert, R. Smoluchowski, E. Wigner, Phys. Rev. 50 (1936), 58.
- 17) A.K. Rajagopal, J. Phys. Chem. Solids, 23 (1962), 317.
- 18) J.L. Warren, Rev. Mod. Phys. 40 (1968), 38.
- 19) C. Kittel, Introduction to Solid State Physics, third edition New York (1967), 393.
- 20) G.E. Bacon, Acta Cryst. A25 (1969), 391.
- 21) B.D. Lichter, J. Electrochem. Soc. 109 (1962), 819.
- 22) H.M. Rietveld, Reactor Centrum Nederland Research Report RCN-67 (1967).

## Chapter VII

### ZINC BLENDE

#### 7.1. Introduction

Zinc blende is the simplest non-centrosymmetric crystal and a large number of semiconducting and insulating materials have the same crystal structure. Zinc blende itself is a II-VI compound and an insulator. The lattice dynamics of the zinc blende structure has been studied by many authors. The first calculations, made by Merten<sup>1)</sup> and by Rajagopal and Srinivasan<sup>2)</sup>, applied a force constant model or a rigid ion model and used the elastic constants for numerical calculations. From the Raman spectrum Couture-Mathieu and Mathieu<sup>3,4)</sup> found the frequencies of the LO and TO modes at the zone centre to be 10.47 and  $8.22 \times 10^{12} \text{ s}^{-1}$ , respectively. Infra-red absorption was investigated by Deutsch<sup>5)</sup> but the results could not be interpreted unambiguously. More recently Brafman and Mitra<sup>6)</sup> found from the Raman spectra for the LO and TO frequencies the values 10.53 and  $8.29 \times 10^{12} \text{ s}^{-1}$  in good agreement with the earlier measurements. Nilsen<sup>7)</sup> interpreted the second-order Raman spectrum in terms of the following zone boundary frequencies for the modes TA, LA, TO and LO: 2.64, 3.30, 9.18 and  $10.0 \times 10^{12} \text{ s}^{-1}$ , respectively, and 10.56 and  $8.13 \times 10^{12} \text{ s}^{-1}$ , for the LO and TO frequencies at the centre of the zone. Shell model calculations on zinc blende were carried out by Kaplan and Sullivan<sup>8)</sup> who concluded that the number of available frequencies was insufficient for a unique determination of the parameters of a shell model. Complete neutron scattering data on the dispersion relation of crystals with the zinc blende structure exist only for gallium arsenide<sup>9)</sup> and gallium phosphide<sup>10)</sup>. For both compounds the data have been analysed by means of a shell model. For a good fit to the experimental results fourteen adjustable parameters were required in both cases.

Recently - at about the time when the experimental work of this investigation had been completed- the first neutron data on the acoustic branches of zinc blende were published by Feldkamp, Venkataraman and King<sup>11)</sup> later followed by an analysis by means of a rigid ion model by Vetelino, Mitra, Brafman and Damen<sup>12)</sup>. In the present investigation an

Section 7.1.

almost complete set of acoustic and optic branches in the symmetry directions has been determined.

7.2. Lattice dynamics

7.2.1. Short-range force constants and coupling coefficients

The zinc blende lattice consists of two interpenetrating face-centred cubic lattices, displaced relative to each other by a quarter of the cube diagonal. This structure is similar to that of diamond, but there the two sublattices are occupied by equal atoms. The primitive unit cell is the same as for the fluorite structure and is defined by the three translation vectors  $\underline{a}_1$ ,  $\underline{a}_2$  and  $\underline{a}_3$  given in 6.2.1 with  $a = 5.4060 \text{ \AA}$ . The positions of the two atoms in the primitive cell are again defined by  $\underline{r}(\kappa) = \frac{1}{4}a(\kappa-1)(1,1,1)$  with  $\kappa = 1$  for Zn and  $\kappa = 2$  for S.

The short-range force constants and the expressions for the coupling coefficients are very similar to those for diamond, which have been defined by Smith<sup>13)</sup>. The force constant matrices for the short-range interactions, defined by (2.3) take the form

Zn - S:  $(\kappa\kappa') = (12)$

$\underline{r}(1'_t\kappa') - \underline{r}(0\kappa) = \frac{1}{4}a(1,1,1)$  and equivalent vectors

$$\phi(0\kappa; 1'_t\kappa') = \begin{vmatrix} \alpha_1 & \beta_1 & \beta_1 \\ \beta_1 & \alpha_1 & \beta_1 \\ \beta_1 & \beta_1 & \alpha_1 \end{vmatrix} \quad (7.1)$$

Zn - Zn:  $(\kappa\kappa') = (11)$

$\underline{r}(1'_t\kappa') - \underline{r}(0\kappa) = \frac{1}{2}a(1,1,0)$  and equivalent vectors

$$\phi(0\kappa; 1'_t\kappa') = \begin{vmatrix} \alpha_2 & \gamma_2 & \delta_2 \\ \gamma_2 & \alpha_2 & \delta_2 \\ \delta_2 & -\delta_2 & \beta_2 \end{vmatrix} \quad (7.2)$$

S - S:  $(\kappa\kappa') = (22)$

$\underline{r}(1'_t\kappa') - \underline{r}(0\kappa) = \frac{1}{2}a(1,1,0)$  and equivalent vectors

$$\phi(0\kappa; 1'_t\kappa') = \begin{vmatrix} \alpha_3 & \gamma_3 & -\delta_3 \\ \gamma_3 & \alpha_3 & -\delta_3 \\ \delta_3 & \delta_3 & \beta_3 \end{vmatrix} \quad (7.3)$$

With these force constant matrices the short-range coupling coefficients defined by (3.2) and (3.12) can be expressed as follows

Zinc - Zinc:

$$R_{\alpha\alpha}(11;\underline{q}) = 4\alpha_1 + 8\alpha_2 + 4\beta_2 - 4\alpha_2 C_{2\alpha} (C_{2\beta} + C_{2\gamma}) - 4\beta_2 C_{2\beta} \cdot C_{2\gamma} \quad (7.4)$$

$$R_{\alpha\beta}(11;\underline{q}) = 4\gamma_2 S_{2\alpha} \cdot S_{2\beta} - 4i\delta_2 S_{2\gamma} (C_{2\alpha} - C_{2\beta})$$

Zinc - Sulphur:

$$R_{\alpha\alpha}(12;\underline{q}) = -4\alpha_1 (C_\alpha \cdot C_\beta \cdot C_\gamma - iS_\alpha \cdot S_\beta \cdot S_\gamma) \quad (7.5)$$

$$R_{\alpha\beta}(12;\underline{q}) = 4\beta_1 (S_\alpha \cdot S_\beta \cdot C_\gamma - iC_\alpha \cdot C_\beta \cdot S_\gamma)$$

Sulphur - Sulphur:

$$R_{\alpha\alpha}(22;\underline{q}) = 4\alpha_1 + 8\alpha_3 + 4\beta_3 - 4\alpha_3 C_{2\alpha} (C_{2\beta} + C_{2\gamma}) - 4\beta_3 C_{2\beta} \cdot C_{2\gamma} \quad (7.6)$$

$$R_{\alpha\beta}(22;\underline{q}) = 4\gamma_3 S_{2\alpha} \cdot S_{2\beta} + 4i\delta_3 S_{2\gamma} (C_{2\alpha} - C_{2\beta})$$

$C_\alpha$ ,  $C_{2\alpha}$ ,  $S_\alpha$ ,  $S_{2\alpha}$  have been defined in section 6.2.1.

### 7.2.2. Group theory

The symmetry properties of the zinc blende lattice have been discussed by Parmenter<sup>14)</sup> and by Dresselhaus<sup>15)</sup> in connection with the calculation of the electron energy bands. Yarnell and Warren<sup>10)</sup> summarized briefly the implications of the symmetry on the dynamical properties. Following the line of the previous chapter a brief outline of the group-theoretical treatment in the directions of symmetry will be given here.

The zinc blende structure has the space group  $T_d^2$  or  $\bar{F}43m$ ; it is symmorphic. The notation given in the previous chapter will be used here too.

Section 7.2.

[001],  $q = q_6$

The point group of the wave vector  $q_6$  is  $C_{2v}$ . It is Abelian and hence all irreducible representations are one-dimensional. The characters for these representations have been given in Table 7.1.

Table 7.1. Character table of the group  $C_{2v}(q_6)$ ; the irreducible representations have been denoted according to Kovalev's and the BSW notation. The characters of the reducible representation  $T(q_6)$  have been given in the last line.

Kovalev	$R_1$	$R_4$	$R_{37}$	$R_{40}$	BSW
$\tau_1$	1	1	1	1	$\Delta_1$
$\tau_2$	1	1	-1	-1	$\Delta_2$
$\tau_3$	1	-1	1	-1	$\Delta_3$
$\tau_4$	1	-1	-1	1	$\Delta_4$
$\chi^T$	6	-2	2	2	

The reducible representation  $T(q_6)$  defined by (2.30) takes the form

$$\begin{aligned}
 T(q_6, R_1) &= \begin{vmatrix} R_1 & 0 \\ 0 & R_1 \end{vmatrix} & T(q_6, R_4) &= \begin{vmatrix} R_4 & 0 \\ 0 & R_4 \end{vmatrix} \\
 T(q_6, R_{37}) &= \begin{vmatrix} R_{37} & 0 \\ 0 & R_{37} \end{vmatrix} & T(q_6, R_{40}) &= \begin{vmatrix} R_{40} & 0 \\ 0 & R_{40} \end{vmatrix}
 \end{aligned} \tag{7.7}$$

The characters of this representation have been given in the last line of Table 7.1. By means of the decomposition formula (2.34) this reducible representation  $T(q_6)$  has been decomposed into its irreducible components  $T(q_6) = 2\tau_1 \oplus 2\tau_3 \oplus 2\tau_4$ . The six branches in the dispersion relation are not all different due to time-reversal degeneracy which can be seen as follows.

With the anti-unitary symmetry operator  $A_0 = \begin{pmatrix} 0 & 1 & 0 \\ \bar{1} & 0 & 0 \\ 0 & 0 & \bar{1} \end{pmatrix}$  belonging to the group  $T_d$  the summation (2.41) can be carried out for the three representations:

		$\Delta_1$	$\Delta_3$	$\Delta_4$
$R_1: (A_0 R_1)^2 = R_4$	$\chi^\Delta(q_6, R_4)$	1	-1	-1
$R_4: (A_0 R_4)^2 = R_4$	$\chi^\Delta(q_6, R_4)$	1	-1	-1
$R_{37}: (A_0 R_{37})^2 = R_1$	$\chi^\Delta(q_6, R_1)$	1	1	1
$R_{40}: (A_0 R_{40})^2 = R_1$	$\chi^\Delta(q_6, R_1)$	1	1	1
	$w(\Delta)$	4	0	0

This shows that  $\Delta_1$  is non-degenerate, type 1, and that  $\Delta_3, \Delta_4$  are doubly degenerate, type 3.

By means of the projection operators (2.36) and equation (2.37) the following symmetry adapted eigenvectors have been obtained

$$E(\Delta_1) = \begin{pmatrix} 0 \\ 0 \\ a_1 \\ 0 \\ 0 \\ b_1 \end{pmatrix} \quad E(\Delta_3) = \begin{pmatrix} a_3 \\ a_3 \\ 0 \\ b_3 \\ b_3 \\ 0 \end{pmatrix} \quad E(\Delta_4) = \begin{pmatrix} a_4 \\ -a_4 \\ 0 \\ b_4 \\ -b_4 \\ 0 \end{pmatrix} \quad (7.8)$$

Here  $E(\Delta_1)$  represents longitudinal vibrations, whereas  $E(\Delta_3)$  and  $E(\Delta_4)$  are two orthogonal transverse modes. The equations for the dynamical matrices and basisvectors of the subspaces associated with these irreducible representations are

Section 7.2.

for  $\Delta_1$ :

$$\begin{vmatrix} D_{zz}(11) - \omega^2 & \rho_1 D_{zz}(12) \\ \rho_1^* D_{zz}(12) & D_{zz}(22) - \omega^2 \end{vmatrix} \times \begin{vmatrix} a_1 \\ b_1 \end{vmatrix} = 0 \quad (7.9)$$

for  $\Delta_3$ :

$$\begin{vmatrix} D_{xx}(11) - \omega^2 & \rho_1 \{D_{xx}(12) + D_{xy}(12)\} \\ \rho_1^* \{D_{xx}(12) - D_{xy}(12)\} & D_{xx}(22) - \omega^2 \end{vmatrix} \times \begin{vmatrix} a_3 \\ b_3 \end{vmatrix} = 0 \quad (7.10)$$

for  $\Delta_4$ :

$$\begin{vmatrix} D_{xx}(11) - \omega^2 & \rho_1 \{D_{xx}(12) - D_{xy}(12)\} \\ \rho_1^* \{D_{xx}(12) + D_{xy}(12)\} & D_{xx}(22) - \omega^2 \end{vmatrix} \times \begin{vmatrix} a_4 \\ b_4 \end{vmatrix} = 0 \quad (7.11)$$

[111],  $\underline{q} = \underline{q}_5$

The point group of the wave vector is  $C_{3v}$  which has six symmetry elements divided into three classes. Two of the three irreducible representations are one-dimensional and one is two-dimensional. These representations and their characters have been given in Table 6.2. The reducible representation  $T(\underline{q}_5)$  is here

$$\begin{aligned} T(\underline{q}_5, R_1) &= \begin{vmatrix} R_1 & 0 \\ 0 & R_1 \end{vmatrix} & T(\underline{q}_5, R_9) &= \begin{vmatrix} R_9 & 0 \\ 0 & R_9 \end{vmatrix} \\ T(\underline{q}_5, R_5) &= \begin{vmatrix} R_5 & 0 \\ 0 & R_5 \end{vmatrix} & T(\underline{q}_5, R_{37}) &= \begin{vmatrix} R_{37} & 0 \\ 0 & R_{37} \end{vmatrix} \\ T(\underline{q}_5, R_{41}) &= \begin{vmatrix} R_{41} & 0 \\ 0 & R_{41} \end{vmatrix} & T(\underline{q}_5, R_{45}) &= \begin{vmatrix} R_{45} & 0 \\ 0 & R_{45} \end{vmatrix} \end{aligned} \quad (7.12)$$

The characters of this representation are

	$R_1$	$R_9$	$R_5$	$R_{37}$	$R_{41}$	$R_{45}$
$\chi^T$	6	0	0	2	2	2

Using (2.34) the decomposition becomes  $T(\underline{q}_5) = 2\tau_1 \oplus 2\tau_3$ . The symmetry adapted eigenvectors for these irreducible representations are

$$E(\Lambda_1) = \begin{pmatrix} a_1 \\ a_1 \\ a_1 \\ b_1 \\ b_1 \\ b_1 \end{pmatrix} \quad E(\Lambda_3 \ 1) = \begin{pmatrix} a_3 \\ a_3 \\ -2a_3 \\ b_3 \\ b_3 \\ -2b_3 \end{pmatrix} \quad E(\Lambda_3 \ 2) = \begin{pmatrix} -\sqrt{3}a_3 \\ \sqrt{3}a_3 \\ 0 \\ -\sqrt{3}b_3 \\ \sqrt{3}b_3 \\ 0 \end{pmatrix} \quad (7.13)$$

$E(\Lambda_1)$  represents longitudinal vibrations,  $E(\Lambda_3 \ 1)$  and  $E(\Lambda_3 \ 2)$  are two orthogonal transverse modes.

The equations for the dynamical matrices and the basisvectors of the subspaces associated with these irreducible representations are

for  $\Lambda_1$ :

$$\begin{vmatrix} D_{xx}(11) + 2D_{xy}(11) - \omega^2 & \rho_1 \{D_{xx}(12) + 2D_{xy}(12)\} \\ \rho_1^* \{D_{xx}^*(12) + 2D_{xy}^*(12)\} & D_{xx}(22) + 2D_{xy}(22) - \omega^2 \end{vmatrix} \times \begin{pmatrix} a_1 \\ b_1 \end{pmatrix} = 0 \quad (7.14)$$

for  $\Lambda_3$ :

$$\begin{vmatrix} D_{xx}(11) - D_{xy}(11) - \omega^2 & \rho_1 \{D_{xx}(12) - D_{xy}(12)\} \\ \rho_1^* \{D_{xx}^*(12) - D_{xy}^*(12)\} & D_{xx}(22) - D_{xy}(22) - \omega^2 \end{vmatrix} \times \begin{pmatrix} a_3 \\ b_3 \end{pmatrix} = 0 \quad (7.15)$$

Section 7.2.

[110],  $\underline{q} = \underline{q}_4$

The point group of the wave vector is  $C_s$ , a group consisting of two elements. Apart from the identity element it has only a symmetry plane. The character table is given in Table 7.2.

Table 7.2. Character table of the group  $C_s(\underline{q}_4)$ . The characters of the representation  $T(\underline{q}_4)$  have been given in the last line.

Kovalev	$R_1$	$R_{37}$	BSW
$\tau_1$	1	1	$\Sigma_1$
$\tau_2$	1	-1	$\Sigma_2$
$\chi^T$	6	2	

The reducible representation  $T(\underline{q}_4)$  can be written as

$$T(\underline{q}_4, R_1) = \begin{vmatrix} R_1 & 0 \\ 0 & R_1 \end{vmatrix} \quad T(\underline{q}_4, R_{37}) = \begin{vmatrix} R_{37} & 0 \\ 0 & R_{37} \end{vmatrix} \quad (7.16)$$

The decomposition into its irreducible representations results in  $T(\underline{q}_4) = 4\tau_1 \oplus 2\tau_2$ . Both irreducible representations are one-dimensional and consequently the dispersion relation must consist of six non-degenerate branches.

The symmetry adapted eigenvectors for  $\Sigma_1$  and  $\Sigma_2$  are

$$E(\Sigma_1) = \begin{vmatrix} a_1 \\ a_1 \\ b_1 \\ c_1 \\ c_1 \\ d_1 \end{vmatrix} \quad \text{and} \quad E(\Sigma_2) = \begin{vmatrix} a_2 \\ -a_2 \\ 0 \\ b_2 \\ -b_2 \\ 0 \end{vmatrix} \quad (7.17)$$

The first represents vibrations parallel to the symmetry plane and the second vibrations perpendicular upon it. Therefore, the first is a combination of longitudinal and transverse components, whereas the second is purely transverse. The equations for the dynamical matrices and the basisvectors for the subspaces associated with  $\Sigma_1$  and  $\Sigma_2$  are

for  $\Sigma_1$ :

$$\begin{vmatrix} D_{xx}(11)+D_{xy}(11)-\omega^2 & \sqrt{2}D_{xz}(11) & \rho_1\{D_{xx}(12)+D_{xy}(12)\} & \sqrt{2}\rho_1D_{xz}(12) \\ -\sqrt{2}D_{xz}(11) & D_{zz}(11)-\omega^2 & \sqrt{2}\rho_1D_{xz}(12) & \rho_1D_{zz}(12) \\ \rho_1^*\{D_{xx}(12)+D_{xy}(12)\} & -\sqrt{2}\rho_1^*D_{xz}(12) & D_{xx}(22)+D_{xy}(22)-\omega^2 & \sqrt{2}D_{xz}(22) \\ -\sqrt{2}\rho_1^*D_{xz}(12) & \rho_1^*D_{zz}(12) & -\sqrt{2}D_{xz}(22) & D_{zz}(22)-\omega^2 \end{vmatrix} \times \begin{vmatrix} a_1 \\ b_1 \\ c_1 \\ d_1 \end{vmatrix} = 0$$

and for  $\Sigma_2$ : (7.18)

$$\begin{vmatrix} D_{xx}(11)-D_{xy}(11)-\omega^2 & \rho_1\{D_{xx}(12)-D_{xy}(12)\} \\ \rho_1^*\{D_{xx}(12)-D_{xy}(12)\} & D_{xx}(22)-D_{xy}(22)-\omega^2 \end{vmatrix} \times \begin{vmatrix} a_2 \\ b_2 \end{vmatrix} = 0 \quad (7.19)$$

### 7.2.3. Elastic constants and optic frequencies

With the assumption of the rigid ion model it has been possible to establish a number of expressions for frequencies at the zone centre and zone boundary in terms of the short-range force constants and the effective ion charge. Applying the method of long waves described in section 2.2. expressions for the elastic constants have been derived. In the same way as for the fluorite structure in 6.2.3 Rajagopal's<sup>16)</sup> numerical results were used for the Coulomb contributions. The following expressions have been obtained

$$c_{11} = \frac{1}{a}\{\alpha_1+4\alpha_2+4\alpha_3+0.2510Z^2 \cdot \frac{e^2}{v_a}\} \quad (7.20)$$

$$c_{12} = \frac{1}{a}\{-\alpha_1+2\beta_1-2(\alpha_2+\alpha_3)-2(\beta_2+\beta_3)+4(\gamma_2+\gamma_3)-2.648Z^2 \cdot \frac{e^2}{v_a}\} \quad (7.21)$$

Section 7.2.

$$c_{44} = \frac{1}{a} \left\{ \alpha_1 + 2(\alpha_2 + \alpha_3) + 2(\beta_2 + \beta_3) - 0.126Z^2 \cdot \frac{e^2}{v_a} - \frac{(\beta_1 - 2.519Z^2 \cdot \frac{e^2}{v_a})^2}{\alpha_1 \cdot \frac{1}{3}\pi Z^2 \cdot \frac{e^2}{v_a}} \right\} \quad (7.22)$$

In the limit of long wavelengths the dynamical matrices for the irreducible representations in special directions can again be used to obtain explicit expressions for the optic frequencies at the zone centre. With  $q = 0$  the following expressions can be derived.

From (7.9):

$$\omega^2(\Gamma \Delta_1 0) = (2\pi v_{LO})^2 = \left(\frac{1}{m_1} + \frac{1}{m_2}\right) \left(4\alpha_1 + \frac{8}{3}\pi Z^2 \cdot \frac{e^2}{v_a}\right) \quad (7.23)$$

from (7.10):

$$\omega^2(\Gamma \Delta_3 0) = (2\pi v_{TO})^2 = \left(\frac{1}{m_1} + \frac{1}{m_2}\right) \left(4\alpha_1 + \frac{4}{3}\pi Z^2 \cdot \frac{e^2}{v_a}\right) \quad (7.24)$$

Since  $D_{ZZ}(12; q) = 0$  at the point (001) the matrix of (7.9) provides also explicit expressions for the zone boundary frequencies associated with  $\Delta_1$ .

$$\omega^2(X \Delta_1 A) = m_1^{-1} (4\alpha_1 + 16\alpha_2 + 4.3336Z^2 \cdot \frac{e^2}{v_a}) \quad (7.25)$$

$$\omega^2(X \Delta_1 0) = m_2^{-1} (4\alpha_1 + 16\alpha_3 + 4.3336Z^2 \cdot \frac{e^2}{v_a}) \quad (7.26)$$

Here the fact has been used that  $m_1 > m_2$ . These last two equations could only be applied after experimental results on the zone boundary frequencies became available.

From Couture-Mathieu and Mathieu's<sup>3,4)</sup> data it has been found that  $v_{LO} = 10.47$  and  $v_{TO} = 8.22 \times 10^{12} \text{ s}^{-1}$  and by means of (7.23) and (7.24)  $\alpha_1$  and  $Z$  have been calculated from these values. It was then assumed that the second-nearest-neighbour forces are central and that they are equal for zinc and sulphur, so that  $\alpha_2 = \gamma_2 = \alpha_3 = \gamma_3$  and that  $\beta_2 = \beta_3 = \delta_2 = \delta_3 = 0$ . From the elastic constants given by Berlincourt *et al.*<sup>17)</sup>  $c_{11} = 10.46$ ,  $c_{12} = 6.53$  and  $c_{44} = 4.613 \times 10^{11} \text{ dyn.cm}^{-2}$  - and by means of (7.21) and (7.22)  $\alpha_2$  and  $\beta_1$  could be calculated. These are the parameters for rigid ion model I in Table 7.3. This set of parameters is

Table 7.3. Model parameters for zinc blende; I, II and III are rigid ion models and IV is a shell model. The short-range force constants are in units of  $10^4 \text{ dyn.cm}^{-1}$  and the ion charge is in units of  $e$ .

	Model I from el. const. and zone centre freq.	Model II with zone boundary freq.	Model III fitted by trial	Model IV
$\alpha_1$	+2.897	+2.884	+2.963	+4.78
$\beta_1$	+3.183	+3.57	+3.40	+4.23
$\alpha_2$	+0.33	+0.16	+0.18	-0.163
$\beta_2$	0	+0.08	+0.05	0
$\gamma_2$	+0.33	+0.16	+0.18	-0.163
$\alpha_3$	+0.33	+0.463	+0.36	+0.537
$\beta_3$	0	+0.25	+0.10	0
$\gamma_3$	+0.33	+0.463	+0.36	+0.537
Z	+0.902	+0.937	+0.865	+0.171
$\Pi_S(v_a)$				+0.1128
$d_S(e)$				+1.063

approximately the same as was calculated by Vetelino *et al.*<sup>12)</sup> by means of a least squares computation from almost the same numerical values as have been used here. The parameters of model I have been used for the first calculation of the inelastic structure factors. The values for the scattering amplitudes are  $b_{\text{Zn}} = 0.57 \times 10^{-12}$  cm and  $b_{\text{S}} = 0.28 \times 10^{-12}$  cm and the Debye-Waller factors have been assumed to be equal to unity.

### 7.3. Results and analysis

The zinc blende specimen was a natural single crystal of about  $15 \text{ cm}^3$  from the Houillères du Bassin du Dauphiné at Le Villaret de Susville (Isère) in France. It had one very pronounced (110) face and showed a light yellow to brown colour. Impurities found by chemical

## Section 7.3.

analysis were 0.15% Cd, 0.05% Fe and minor amounts of Si and Cu. The mosaic spread of the crystal was about 14' full width at half maximum. Phonons of the  $\Sigma_2A$  branch have been measured with the (001) plane horizontal and all other experiments have been carried out with the ( $\bar{1}\bar{1}0$ ) plane horizontal. Using standard procedures for operating the triple-axis spectrometer all acoustic branches could be determined, but from the optic branches only some phonons of  $\Delta_30$  have been observed though with some difficulties. For the successful measurements of the optic branches the application of the inverse-beryllium-filter method, described in section 5.5, has been necessary. All optic branches in the symmetry directions except  $\Sigma_20$  have been determined by means of experiments according to this technique. The data for  $\Delta_30$  obtained by means of the two methods are in good agreement. Phonons of the branch  $\Sigma_20$  could not be measured in this way because this would have required scattering angles for the neutrons which were larger than accessible for the spectrometer or because the conservation laws could not be satisfied. The frequencies of phonons in the symmetry directions observed for selected wave vectors have been presented in Table 7.4 and plotted versus reduced wave vector in Fig. 7.1.

From the neutron data and the elastic constants the rigid ion model parameters were calculated anew with the assumptions  $\alpha_2 = \gamma_2$ ,  $\alpha_3 = \gamma_3$  and  $\beta_2/\beta_3 = \alpha_2/\alpha_3$ . The values calculated for this model II have been tabulated in Table 7.3. Final adjustments to the parameters were then made by trial and error fitting of the calculated curves to the experimental results. This provided the parameter values of model III. The dispersion relation calculated for this model has been plotted in Fig. 7.1. In this figure the straight lines drawn from the origin represent the velocities of sound as derived from the elastic constants. For rigid ion model III the inelastic structure factors have been presented in Fig. 7.2. The repetition unit for this inelastic structure factor is equal to that of the fluorite structure and, therefore, the curves of Fig. 7.2 also correspond to the directions and positions indicated in Fig. 6.4. Comparison of these curves with those for germanium calculated by Brockhouse and Iyengar<sup>18)</sup> shows a close relationship for these crystals.

Table 7.4. Frequencies ( $10^{12} \text{ s}^{-1}$ ) of normal modes in zinc blende measured in the symmetry directions.

[00 $\zeta$ ]					
$\frac{a}{2\pi} \cdot q$	$\Delta_3 A$	$\Delta_1 A$	$\Delta_3 O$	$\Delta_3 O_{\text{Be}}$	$\Delta_1 O_{\text{Be}}$
0				8.36±0.10*	10.30±0.15**
0.20	1.10±0.03	1.85±0.15	8.60±0.15	8.60±0.07	10.35±0.10
0.30	1.64±0.03	2.60±0.15			
0.40	2.03±0.03	3.50±0.10	8.70±0.15	8.85±0.10	10.27±0.07
0.50	2.32±0.05	4.30±0.10			
0.60	2.47±0.07	4.90±0.10	9.00±0.15	9.10±0.07	10.10±0.07
0.70	2.54±0.07	5.50±0.10			
0.80	2.58±0.07	6.00±0.10	9.20±0.15	9.30±0.10	10.0 ±0.10
0.90	2.64±0.10	6.20±0.20			
1.00	2.65±0.10*	6.15±0.15*	9.10±0.15	9.40±0.15	9.65±0.10**
[ $\zeta\zeta 0$ ]					
$\frac{a}{2\pi} \cdot q$	$\Sigma_2 A$	$\Sigma_1 A_2$	$\Sigma_1 A_1$	$\Sigma_1 O_2_{\text{Be}}$	$\Sigma_1 O_1_{\text{Be}}$
0				8.36±0.10*	10.30±0.15
0.20	0.80±0.05	1.24±0.03	2.05±0.05	8.55±0.07	10.55±0.15
0.30	1.20±0.03	1.75±0.03	2.95±0.05		
0.40	1.50±0.03	2.24±0.03	3.65±0.03	8.90±0.07	10.48±0.10
0.50	1.87±0.03	2.66±0.03	4.33±0.07		
0.60	2.12±0.03	3.03±0.03	4.80±0.07	9.15±0.10	10.30±0.10
0.70	2.35±0.03	3.37±0.05	5.20±0.10		
0.80	2.50±0.05	3.55±0.05	5.65±0.10	9.20±0.10	9.80±0.10
0.90	2.63±0.05	3.67±0.07	5.80±0.07		
1.00	2.65±0.10	3.65±0.07	5.80±0.10	9.10±0.10	9.70±0.10
1.10	2.70±0.07	3.35±0.05	5.90±0.10		
1.20	2.70±0.15	3.05±0.05	6.10±0.10		9.65±0.10
1.30	2.70±0.10	2.75±0.07	6.00±0.10		
1.414	2.65±0.10*	2.65±0.10*	6.15±0.15*	9.40±0.15**	9.65±0.10
[ $\zeta\zeta\zeta$ ]					
$\frac{a}{2\pi} \cdot q$	$\Lambda_3 A$	$\Lambda_1 A$	$\Lambda_3 O_{\text{Be}}$	$\Lambda_1 O_{\text{Be}}$	
0			8.36±0.10*	10.30±0.15**	
0.20		1.85±0.15	8.55±0.07	10.30±0.10	
0.30	1.40±0.03	2.75±0.20			
0.40	1.74±0.03	3.80±0.15	8.72±0.10	10.23±0.10	
0.50	1.93±0.05	4.50±0.10			
0.60	2.02±0.05	5.10±0.10	8.78±0.10	10.25±0.10	
0.70	2.10±0.05	5.50±0.15			
0.80	2.09±0.10	5.72±0.12	8.95±0.10	10.10±0.10	
0.866	2.10±0.10	5.60±0.20	8.83±0.10		

\* average of observations from different branches

\*\* copied from other branches

Section 7.3.

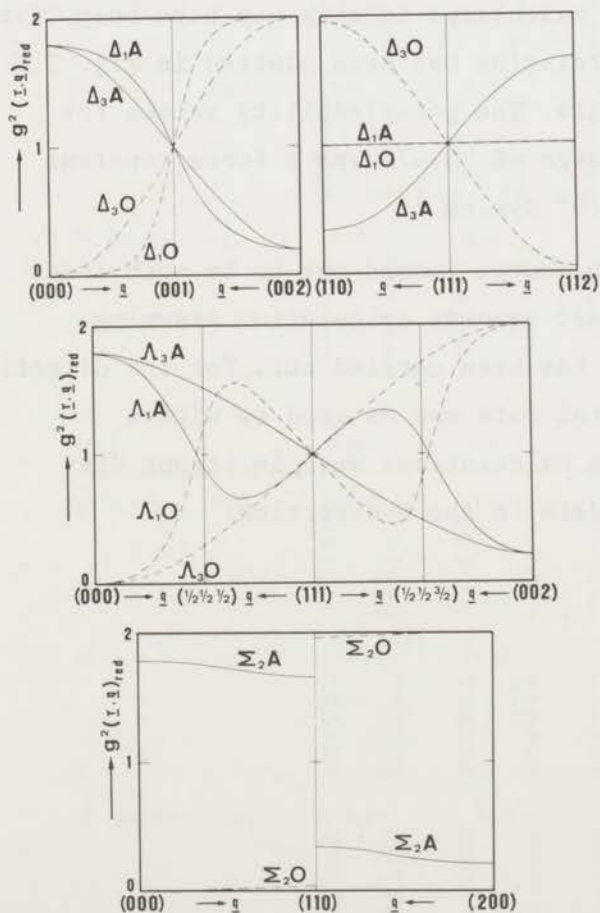
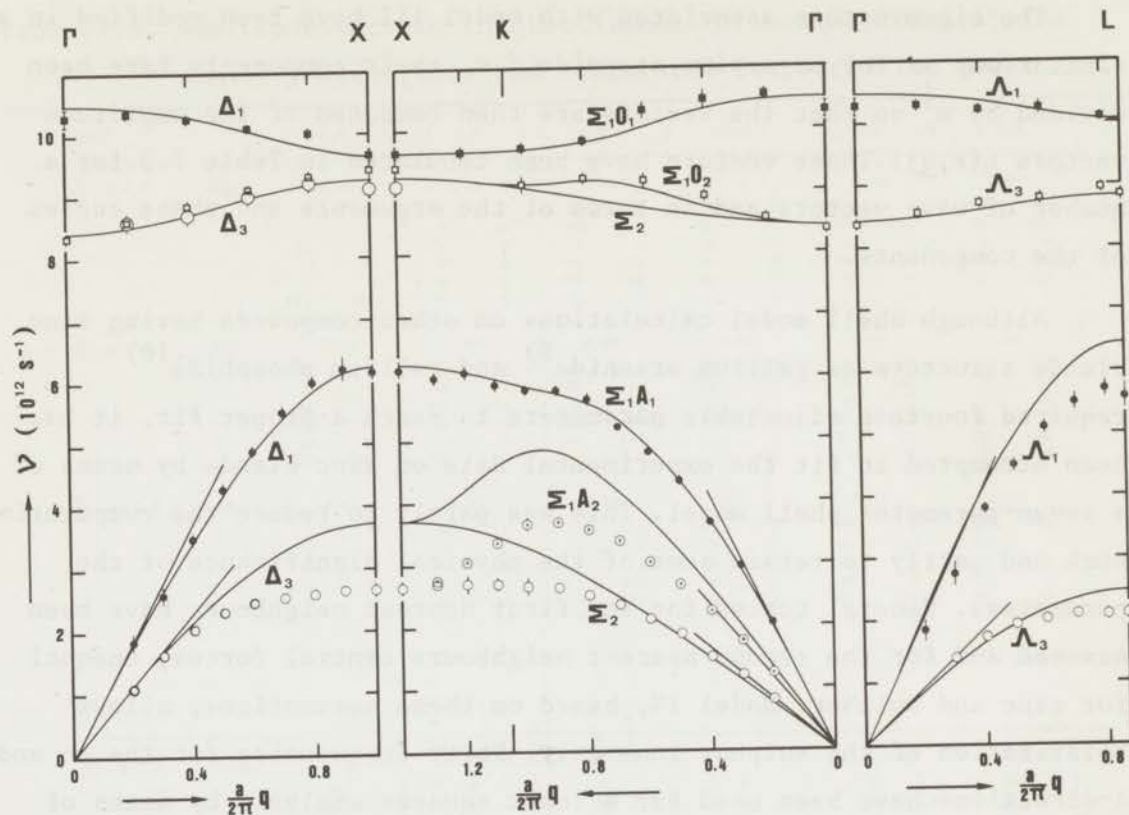


Fig. 7.1.

Dispersion relation for zinc blende. The solid lines have been calculated according to rigid ion model III. The straight lines drawn from the origin represent the velocities of sound. For  $\Delta$  and  $\Lambda$  the open points represent transverse modes and the closed points are longitudinal modes.

Fig. 7.2.

Reduced inelastic structure factors for zinc blende calculated according to rigid ion model III.

The eigenvectors associated with model III have been modified in a similar way as for magnesium stannide *i.e.* their components have been divided by  $m_K^{\frac{1}{2}}$  so that the vectors are then composed of the amplitude vectors  $\underline{n}(\kappa, \underline{qj})$ . These vectors have been tabulated in Table 7.5 for a number of wave vectors and in terms of the arguments and phase angles of the components.

Although shell model calculations on other compounds having zinc blende structure as gallium arsenide<sup>9)</sup> and gallium phosphide<sup>10)</sup> required fourteen adjustable parameters to reach a proper fit, it has been attempted to fit the experimental data on zinc blende by means of a seven-parameter shell model. This was partly to reduce the computational work and partly to retain some of the physical significance of the parameters. General forces for the first nearest neighbours have been assumed and for the second nearest neighbours central forces, unequal for zinc and sulphur. Model IV, based on these assumptions, allows polarization of the sulphur ions only. Forty frequencies for the  $\Delta$ - and  $\Lambda$ -directions have been used for a least squares analysis by means of this shell model. The parameters calculated in this way have been listed in Table 7.3 and the dispersion relation has been plotted in Fig. 7.3 together with the experimental data. The polarizability values for sulphur correspond to a shell charge of  $-3.47e$  and a force constant between core and shell of  $43.3 \times 10^4 \text{ dyn.cm}^{-1}$ .

Since the value of the ionic charge turned out to be much lower than in the rigid ion model a least squares calculation assuming polarizability for the zinc atom has been carried out. For the directions  $\Delta$  and  $\Lambda$  the fit to the experimental data was as good as with a polarizable sulphur atom, but the calculations were in strong disagreement with the experimental data in the  $\Sigma$ -direction.

Chapter 7.3.

Table 7.5. Amplitude vectors in zinc blende for normal modes in the symmetry directions and calculated for rigid ion model III.

[00z]	$\Delta_1 O$	$\Delta_1 A$	$\Delta_3 O$	$\Delta_3 A$	$\Delta_4 O$	$\Delta_4 A$	
$\frac{a}{2\pi} \cdot q = 0$	$v(gj)$	10.49	0	8.43	0	8.43	0
		0 0	0 0	39 0	56 0	39 0	56 0
		0 0	0 0	39 0	56 0	39 180	56 180
		55 0	79 0	0 0	0 0	0 0	0 0
		0 0	0 0	79 180	56 0	79 180	56 0
	0 0	0 0	79 180	56 0	79 0	56 180	
	112 180	79 0	0 0	0 0	0 0	0 0	
$\frac{a}{2\pi} \cdot q = 0.5$	$v(gj)$	10.18	4.17	8.84	2.61	8.84	2.61
		0 0	0 0	36 0	58 357	36 0	58 273
		0 0	0 0	36 0	58 357	36 180	58 93
		46 0	84 315	0 0	0 0	0 0	0 0
		0 0	0 0	82 183	51 0	82 267	51 0
	0 0	0 0	82 183	51 0	82 87	51 180	
	120 225	66 0	0 0	0 0	0 0	0 0	
$\frac{a}{2\pi} \cdot q = 1.0$	$v(gj)$	9.63	6.23	9.24	3.71	9.24	3.71
		0 0	0 0	32 0	60 0	32 0	60 180
		0 0	0 0	32 0	60 0	32 180	60 0
		0 0	96 0	0 0	0 0	0 0	0 0
		0 0	0 0	85 180	46 0	85 0	46 0
	0 0	0 0	85 180	46 0	85 180	46 180	
	137 0	0 0	0 0	0 0	0 0	0 0	
[zr0]	j	$\Gamma_{1,1} O$	$\Gamma_{1,2} O$	$\Gamma_{1,1} A$	$\Gamma_{1,2} A$	$\Gamma_2 O$	$\Gamma_2 A$
$\frac{a}{2\pi} \cdot q = 0$	$v(gj)$	10.49	8.43	0	0	8.43	0
		39 0	0 0	56 0	0 0	39 0	56 0
		39 0	0 0	56 0	0 0	39 180	56 180
		0 0	55 0	0 0	79 0	0 0	0 0
		79 180	0 0	56 0	0 0	79 180	56 0
	79 180	0 0	56 0	0 0	79 0	56 180	
	0 0	112 180	0 0	79 0	0 0	0 0	
$\frac{a}{2\pi} \cdot q = 0.7$	$v(gj)$	9.87	9.13	5.29	4.18	8.80	2.47
		10 0	28 90	58 271	19 1	36 0	58 271
		10 0	28 90	58 271	19 1	36 180	58 91
		29 90	24 0	33 1	82 271	0 0	0 0
		91 269	8 359	26 0	19 270	82 269	51 0
	91 269	8 359	26 0	19 270	82 89	51 180	
	10 359	120 269	39 270	54 0	0 0	0 0	
$\frac{a}{2\pi} \cdot q = 1.414$	$v(gj)$	9.63	9.24	6.23	3.71	9.24	3.71
		0 0	32 0	0 0	60 0	32 0	60 180
		0 0	32 0	0 0	60 0	32 180	60 0
		0 0	0 0	96 0	0 0	0 0	0 0
		0 0	85 180	0 0	46 0	85 0	46 0
	0 0	85 180	0 0	46 0	85 180	46 180	
	137 0	0 0	0 0	0 0	0 0	0 0	
[zrz]	j	$\Lambda_1 O$	$\Lambda_1 A$	$\Lambda_3 O$	$\Lambda_3 A$	$\Lambda_3 O$	$\Lambda_3 A$
$\frac{a}{2\pi} \cdot q = 0$	$v(gj)$	10.49	0	8.43	0	8.43	0
		32 0	45 0	22 0	32 0	39 180	56 180
		32 0	45 0	22 0	32 0	39 0	56 0
		32 0	45 0	45 180	64 180	0 0	0 0
		65 180	45 0	46 180	32 0	79 0	56 180
	65 180	45 0	46 180	32 0	79 180	56 0	
	65 180	45 0	92 0	64 180	0 0	0 0	
$\frac{a}{2\pi} \cdot q = 0.4$	$v(gj)$	10.37	4.13	8.60	1.64	8.60	1.64
		27 0	48 323	22 0	33 278	38 180	56 98
		27 0	48 323	22 0	33 278	38 0	56 278
		27 0	48 323	43 180	65 98	0 0	0 0
		69 217	39 0	47 262	31 0	81 82	54 180
	69 217	39 0	47 262	31 0	81 262	54 0	
	69 217	39 0	93 82	62 180	0 0	0 0	
$\frac{a}{2\pi} \cdot q = 0.866$	$v(gj)$	10.06	6.46	8.82	2.45	8.82	2.45
		5 0	55 0	21 0	33 180	36 180	58 0
		5 0	55 0	21 0	33 180	36 0	58 180
		5 0	55 0	41 180	66 0	0 0	0 0
		79 180	7 0	47 0	30 0	82 180	51 180
	79 180	7 0	47 0	30 0	82 0	51 0	
	79 180	7 0	95 180	59 180	0 0	0 0	

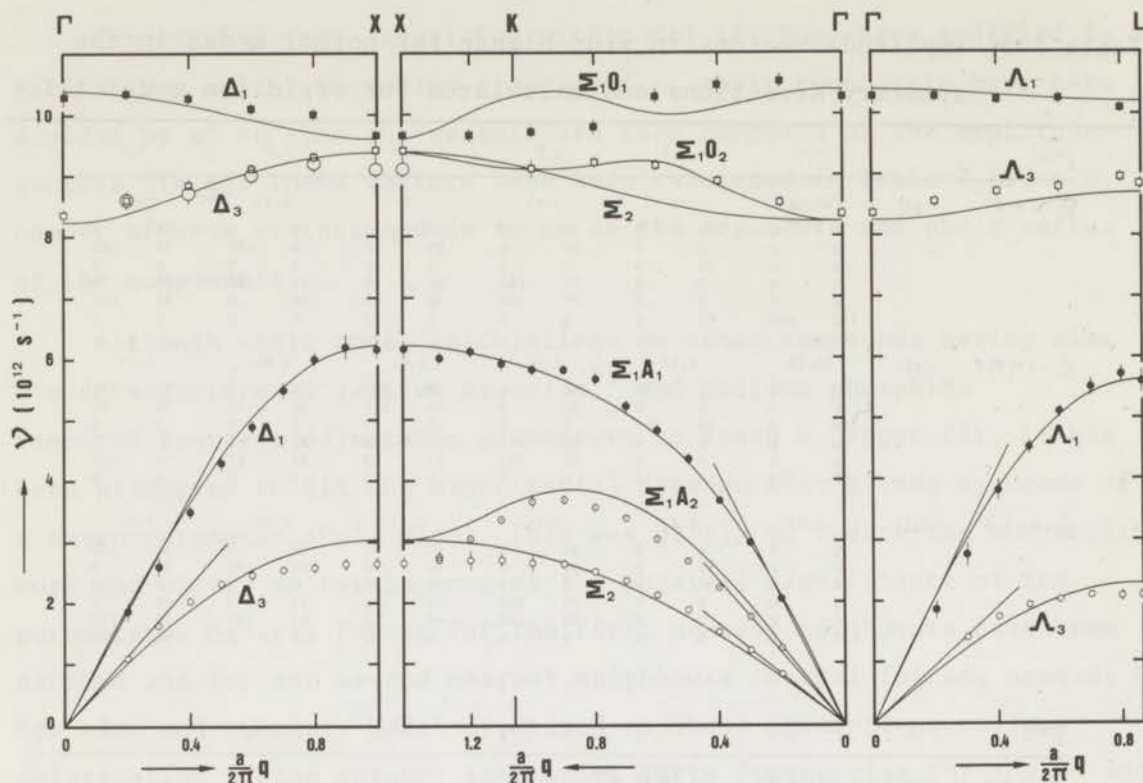


Fig. 7.3. Dispersion relation for zinc blende. The solid lines have been calculated according to the shell model IV. See also Fig. 7.2.

#### 7.4. Discussion

The results on zinc blende show a strong resemblance to the gallium phosphide data <sup>10)</sup>. The ratio's of the zone-boundary frequencies  $\nu(X \Delta_1 O) / \nu(X \Delta_1 A)$  are equal to 1.50 and 1.47, respectively. For both crystals these ratio's are close to the square roots of the mass ratio's which are equal to 1.43 and 1.50. From the relations (7.25) and (7.26) it can be seen that within the rigid ion model discrepancies between the values for these ratio's are an indication for inequality of the two interactions between second nearest neighbours.

Another indication concerning the second-neighbour interactions can be obtained from the Brout sum rule <sup>19,20)</sup> which states that the sum of the squares of the frequencies of all six branches is independent of the wave vector  $q$ . For the rigid ion model this rule is valid if

## Section 7.4.

there are short-range interactions between the first neighbours only. In zinc blende the Brout sum increases by about 25% from the centre to the boundary of the zone compared to 10% in GaP thus indicating that second-neighbour interactions are more important in ZnS.

As in GaP the longitudinal and transverse optic branches in zinc blende do not cross as they do in GaAs<sup>9)</sup>. This is in qualitative agreement with the Keyes-Mitra correlation<sup>21,22)</sup> between the ratio of zone-boundary frequencies  $\nu(X \Delta_1 0)/\nu(X \Delta_3 0)$  and the effective ionic charge, since the rigid ion model led to a relatively high ionicity.

Rigid ion model III provides a very satisfactory fit with all optic branches and part of the acoustic branches. However, serious disagreement exists for  $\Delta_3 A$ ,  $\Sigma_1 A_2$  and  $\Sigma_2 A$  while the fit for  $\Lambda_1 A$  and  $\Lambda_3 A$  is only moderate. The same flattening of the transverse acoustic branches in the outer part of the Brillouin zone as has been observed for magnesium stannide is seen here too.

The amplitude vectors calculated for model III and presented in Table 7.5 show the typical acoustic and optic way of vibration of the atoms for  $q = 0$ . In the acoustic modes the atoms vibrate in phase with the same amplitude whereas in the optic modes the zinc and sulphur atoms vibrate in antiphase with an amplitude ratio equal to  $m_S/m_{Zn}$ .

A significant improvement over the rigid ion model has been obtained by means of the shell model with an equal number of parameters; this is seen by comparing Fig. 7.1 and Fig. 7.3. Therefore it may be concluded that also in zinc blende it is more important to include the polarization of one of the ions than the noncentral components of the interactions between nearest neighbours. The comparison of the experimental results and the calculated curves in Fig. 7.3 demonstrates that a reasonably good overall fit could be obtained by means of a shell model with half as many parameters as were required for a good fit in the analogous compounds GaP and GaAs. The experimental data for the  $\Sigma_1 O_1$  branch are fitted much less well by the shell model than by the rigid ion model. This discrepancy can probably be removed if data in the  $\Sigma$ -direction are included in the least squares calculation. Its shape is very much in agreement with that of the same branch for GaAs and GaP calculated by

means of the fourteen-parameter shell model. Unfortunately, for GaP there are no experimental data on this branch. The experimental results for  $\Sigma_1 O_1$  in GaAs show an almost identical pattern as has been obtained in the present investigation for zinc blende. Since the shape of the calculated curve for GaAs is very similar to  $\Sigma_1 O_1$  in Fig. 7.3, the differences are seen to be qualitatively equal in both cases; for ZnS they are slightly larger than for GaAs.

In Table 7.6 experimental values of the elastic constants and of the infra-red-frequency ratio are compared to the values calculated by means of the models III and IV. Apart from a discrepancy for  $c_{12}$  in the shell model the agreement is very good. The ratio of the infra-red-frequencies has also been derived from the dielectric constants <sup>7)</sup> by means of the LST relation and this value has been given in the table too.

Table 7.6. Elastic constants (in units of  $10^{11}$  dyn.cm<sup>-2</sup>) and the ratio of infra-red frequencies of zinc blende from experiments and calculations according to the models III and IV.

	Experimental	Rigid ion model III	Shell model IV	
$c_{11}$	10.47 <sup>17)</sup>	9.7	11.0	
$c_{12}$	6.53 <sup>17)</sup>	6.4	7.5	
$c_{44}$	4.613 <sup>17)</sup>	4.0	4.4	
$\nu_{LO}/\nu_{TO}$	1.23	1.24	1.26	from LST relation 1.20

Already our first experimental results on the acoustic branches showed that in the recently published data assignments by Nilsen <sup>7)</sup> of  $\nu(X \Delta_1 A)$  to a frequency of  $3.30 \times 10^{12}$  s<sup>-1</sup> and of  $\nu(L \Delta_1 A)$  to a frequency of  $3.60 \times 10^{12}$  s<sup>-1</sup> could not be correct. Feldkamp et al. <sup>11)</sup> presented other assignments for the available infra-red and Raman frequencies consistent with the shell model calculations fitted to their neutron data on the acoustic branches. However, this fit does

## Section 7.4.

not justify their interpretation of the calculated optic branches. These longitudinal and transverse optic branches intersect so that  $\nu(X \Delta_1 0) < \nu(X \Delta_3 0)$  and  $\nu(L \Lambda_1 0) < \nu(L \Lambda_3 0)$ . The results from the present investigation, however, show that these two relations should be reversed and, therefore, most of the branch assignments given by these authors are incorrect. Nilsen <sup>7)</sup> interpreted the second-order Raman spectrum of zinc blende on the basis of four of the observed frequencies: 176, 219, 612 and 665  $\text{cm}^{-1}$  which he considered as the overtones of the four zone-boundary frequencies at the positions X and L. These values correspond to the single frequencies given in section 7.1 for the TA, LA, TO and LO modes at the zone boundary. Comparing them to the present neutron data it can be seen that strong disagreement exists for the LA frequencies. It seems more likely that the second frequency must be assigned to a combination line  $\text{TO}(X) - \text{LA}(X)$ . It is obvious that due to the incorrect assignment the further interpretation of the second-order Raman spectrum must fail as soon as LA modes are involved. From the curves in Fig. 7.3 it follows that apart from  $\nu(X \Delta_3 A)$  the shell model can predict these second-order Raman frequencies reasonably well.

By means of the Clausius Mosotti relation given in the previous chapter and using the high-frequency dielectric constant  $\epsilon_\infty = 8.3$  <sup>23)</sup> the electronic polarizability of sulphur in zinc blende has been calculated; it is  $\Pi_S = 0.169$  (in units of  $\nu_a$ ) compared to 0.113 from the shell model. Both values are smaller than 0.258 as given by Pauling <sup>24)</sup> for  $\text{S}^{2-}$ ; this must be due to the smaller ionic charge of the sulphur ions in ZnS.

In the comparison of the rigid ion model and the shell model it is remarkable that the introduction of only a modest polarizability of the sulphur atoms is coupled with a decrease of the negative charge from 0.865 to 0.171. This latter value would indicate that the bonding in ZnS is mainly covalent in agreement with results on GaAs and GaP. Pauling <sup>24)</sup> defined the amount of ionic character in terms of atomic electronegativities  $x$

$$f_i = 1 - e^{-\frac{1}{4}(x_{\text{Zn}} - x_{\text{S}})^2}$$

With the values from his scale of electronegativities the ionic character for ZnS has been found to be equal to 0.18 which is very close to the shell model value.

A new concept of ionicity has been formulated by Phillips <sup>25,26)</sup> in terms of spectroscopically obtained transition energies between bonding and antibonding states. The fractional ionicity has been defined as

$$f_i = \frac{C^2}{E_h^2 + C^2}$$

where C and  $E_h$  are the energy gaps between the bonding and antibonding states associated with the ionic and covalent parts, respectively, of the potential between the atoms. For zinc blende Phillips and Van Vechten <sup>27)</sup> obtained a fractional ionicity equal to 0.62 compared to 0.31 for GaAs and 0.33 for GaP. The last value is very close to that obtained by Yarnell et al. <sup>10)</sup> from the shell model analysis of neutron data; for GaAs there is no agreement. Such a high ionicity for ZnS is not consistent with the present shell model but fits better to the rigid ion model.

In summary, the seven-parameter shell model accounts in a satisfactory way for the observed elastic constants, the infra-red and Raman frequencies and the polarizability. The mainly covalent bonding character agrees better with the prediction based on Pauling's scale of electronegativity than with the more recent theory of Phillips. Although the seven-parameter shell model cannot be considered to be perfect it seems that its parameters still contain some physical significance.

References

- 1) L. Merten, Z. Naturforsch. 13a (1958), 662, 1067.
- 2) A.K. Rajagopal, R. Srinivasan, Z. Physik, 158 (1960), 471.
- 3) L. Couture-Mathieu, J.P. Mathieu, Compt. Rend. 236 (1953), 371.
- 4) J.P. Mathieu, L. Couture-Mathieu, Compt. Rend. 233 (1951), 32.
- 5) T. Deutsch, Proc Int. Conf. on the Physics of Semiconductors, Exeter, (1962), 505.
- 6) O. Brafman, S.S. Mitra, Phys. Rev. 171 (1968), 931.
- 7) W.G. Nilsen, Phys. Rev. 182 (1969), 838.
- 8) H. Kaplan, J.J. Sullivan, Phys. Rev. 130 (1963), 120.
- 9) J.C.T. Waugh, G. Dolling, Phys. Rev. 132 (1963), 2410.
- 10) J.L. Yarnell, J.L. Warren, R.G. Wenzel, P.J. Dean, Neutron Inelastic Scattering, Proc. Symp. Copenhagen, 1968, Vienna IAEA (1968), 301.
- 11) L.A. Feldkamp, G. Venkataraman, J.S. King, Sol. State Comm. 7 (1969), 1571.
- 12) J.F. Vetelino, S.S. Mitra, O. Brafman, T.C. Damen, Sol. State Comm. 7 (1969), 1809.
- 13) Helen M.J. Smith, Phil. Trans. Roy. Soc. London, A241 (1948), 105.
- 14) R.H. Parmenter, Phys. Rev. 100 (1955), 573.
- 15) G. Dresselhaus, Phys. Rev. 100 (1955), 580.
- 16) A.K. Rajagopal, J. Phys. Chem. Solids, 23 (1962), 317.
- 17) D. Berlincourt, H. Jaffe, L.R. Shiozawa, Phys. Rev. 129 (1963), 1009.
- 18) B.N. Brockhouse, P.K. Iyengar, Phys. Rev. 111 (1958), 747.
- 19) R. Brout, Phys. Rev. 113 (1959), 43.
- 20) H.B. Rosenstock, Phys. Rev. 129 (1963), 1959.
- 21) R.W. Keyes, J. Chem. Phys. 37 (1962), 72.
- 22) S.S. Mitra, Phys. Rev. 132 (1963), 986.
- 23) N.F. Mott, R.W. Gurney, Electronic Processes in Ionic Crystals, 2<sup>nd</sup> ed., Dover Publications Inc., New York (1964).
- 24) L. Pauling, The Nature of the Chemical Bond, Cornell Univ. Press, Ithaca (1960).
- 25) J.C. Phillips, Phys. Rev. Lett. 20 (1968), 550.
- 26) J.C. Phillips, Physics Today, 23 (1970), 23.
- 27) J.C. Phillips, J.A. van Vechten, Phys. Rev. Lett. 22 (1969), 705.

## Chapter VIII

### CONCLUDING REMARKS

The investigations described in the foregoing chapters have proved again that inelastic neutron scattering studied by means of a triple-axis crystal spectrometer is a convenient tool for determining the dispersion relation in a crystal lattice. For lattices with more than one atom per primitive unit cell it is of crucial importance to have available estimates of inelastic structure factors in order to distinguish between the several branches.

The difficulties encountered in the measurement of optic branches of zinc blende according to the standard experimental procedures demonstrated the limitations imposed by neutron flux and crystal size. It has turned out that in such cases the inverse beryllium-filter method is a very valuable auxiliary technique which can have a wide application in investigations on single crystals. However, the method has rather strong limitations because the accessible range in  $\nu$ - $Q$  space is narrow, due to the low energy of the observed scattered neutrons. The method can be improved by cooling of the beryllium filter. The line shape of the intensity of the scattered neutrons as a function of the incident neutron energy will be affected by variations of the inelastic structure factors along the line of the scattered neutron wave vector. Therefore, the considerations in section 5.5 on the correlation between the line shape and the dispersion relation along the scattered wave vector could be refined if data on the inelastic structure factors were included.

Dispersion relations determined by means of inelastic neutron scattering provide data needed for an unambiguous assignment of optically observed vibrational frequencies. From the results obtained on zinc blende it may be concluded that particularly zone-boundary frequencies derived from second-order Raman scattering should be considered critically. In cases where the assignments cannot uniquely be given, even an incomplete set of neutron data may be helpful in distinguishing between overtones of primary frequencies and combination lines.

The results from thermal neutron spectrometry have strongly stim-

*Section 8.*

ulated solid-state theoreticians in their development of dynamical models for metals, alloys, ionic and covalent crystals and for molecular systems and liquids in order to represent and account for the new and more detailed experimental data.

For the ionic and covalent crystals the rigid ion model was extended to a shell model. This was very successful for the highly ionic alkali halides and to a smaller extent for homopolar crystals as e.g. germanium and silicon. For both magnesium stannide and zinc blende the simple shell model calculations carried out in these investigations had a rather preliminary character and were primarily meant to demonstrate and include the effect of polarization in these crystals. Keeping the number of adjustable parameters small it was tried to retain some physical significance in these parameters. The polarizability of the atoms affects the shape of the dispersion curves markedly. The simple shell models provide reasonably satisfactory descriptions of the dispersion relations of the two crystals and some related physical quantities can be predicted without too serious discrepancies.

From these calculations the interesting conclusion may be drawn that it is of much greater importance to take into account the polarizability of one of the atoms than to include noncentral or axially asymmetric components in the second nearest neighbour interactions.

Of course, more detailed representations could be reached by applying more sophisticated versions of the shell model. Generally, however, the physical significance of shell model parameters is considered doubtful if the number of these parameters is large. To some extent this applies already to the simple shell models employed in these investigations. This situation is similar to the description of the dynamics of some metal lattices according to a Born-Von Karman calculation including interactions of a great many neighbours. These far-neighbour interactions which can hardly be realistic, are an indication for the imperfectness of the model which should account for e.g. the role of the electrons in the dynamics of the lattice. It seems that for ionic and covalent crystals, particularly those having zinc blende or related lattices, the shell model requires structural improvement. Cochran <sup>1)</sup> suggested that the unphysical nature of the parameters might be due to

the possibility that the limits of validity of the dipole approximation have been passed. Dick <sup>2)</sup> considered the shell model too flexible for being useful for zinc blende and related structures. Both of these comments as well as the results from the present investigations are probably in good agreement with a suggestion by Nusimovici and Birman <sup>3)</sup> that the central problem in such lattice dynamics studies is the correct inclusion of a proper mixture of long- and short-range forces. A combination of valence forces and long-range fields might produce a model with a more general validity for crystal lattices with a mixed bonding.

References

- 1) W. Cochran, Lattice Dynamics, Proc. Symp. Copenhagen, 1963, Ed. R.F. Wallis, Pergamon Press, London (1965), 75.
- 2) B.G. Dick, Lattice Dynamics, Proc. Symp. Copenhagen, 1963, Ed. R.F. Wallis, Pergamon Press, London (1965), 159.
- 3) M.A. Nusimovici, J.L. Birman, Phys. Rev. 156 (1967), 925.

APPENDIX

In this appendix are given the rotational elements R in matrix notation for the point groups of wave vectors in the symmetry directions of the fluorite and zinc blende lattices.

$R_1 = \begin{vmatrix} 1 & 0 & 0 \\ 0 & 1 & 0 \\ 0 & 0 & 1 \end{vmatrix}$	identity transformation	$R_4 = \begin{vmatrix} \bar{1} & 0 & 0 \\ 0 & \bar{1} & 0 \\ 0 & 0 & 1 \end{vmatrix}$	180° rotation about [001]
$R_5 = \begin{vmatrix} 0 & 1 & 0 \\ 0 & 0 & 1 \\ 1 & 0 & 0 \end{vmatrix}$	240° rotation about [111]	$R_9 = \begin{vmatrix} 0 & 0 & 1 \\ 1 & 0 & 0 \\ 0 & 1 & 0 \end{vmatrix}$	120° rotation about [111]
$R_{14} = \begin{vmatrix} 0 & \bar{1} & 0 \\ 1 & 0 & 0 \\ 0 & 0 & 1 \end{vmatrix}$	90° rotation about [001]	$R_{15} = \begin{vmatrix} 0 & 1 & 0 \\ \bar{1} & 0 & 0 \\ 0 & 0 & 1 \end{vmatrix}$	270° rotation about [001]
$R_{16} = \begin{vmatrix} 0 & 1 & 0 \\ 1 & 0 & 0 \\ 0 & 0 & \bar{1} \end{vmatrix}$	180° rotation about [110]		
$R_{26} = \begin{vmatrix} \bar{1} & 0 & 0 \\ 0 & 1 & 0 \\ 0 & 0 & 1 \end{vmatrix}$	reflection in the plane (100)	$R_{27} = \begin{vmatrix} 1 & 0 & 0 \\ 0 & \bar{1} & 0 \\ 0 & 0 & 1 \end{vmatrix}$	reflection in the plane (010)
$R_{28} = \begin{vmatrix} 1 & 0 & 0 \\ 0 & 1 & 0 \\ 0 & 0 & \bar{1} \end{vmatrix}$	reflection in the plane (001)	$R_{37} = \begin{vmatrix} 0 & 1 & 0 \\ 1 & 0 & 0 \\ 0 & 0 & 1 \end{vmatrix}$	reflection in the plane ( $\bar{1}10$ )
$R_{40} = \begin{vmatrix} 0 & \bar{1} & 0 \\ \bar{1} & 0 & 0 \\ 0 & 0 & 1 \end{vmatrix}$	reflection in the plane (110)	$R_{41} = \begin{vmatrix} 1 & 0 & 0 \\ 0 & 0 & 1 \\ 0 & 1 & 0 \end{vmatrix}$	reflection in the plane (0 $\bar{1}1$ )
$R_{45} = \begin{vmatrix} 0 & 0 & 1 \\ 0 & 1 & 0 \\ 1 & 0 & 0 \end{vmatrix}$	reflection in the plane ( $\bar{1}01$ )		

SUMMARY

This study describes an experimental investigation of the dispersion relations of magnesium stannide and zinc blende employing the inelastic scattering of thermal neutrons. Both compounds have a mixed bonding with short-range covalent forces and long-range forces consisting of ionic and dipole components. Magnesium stannide is a semiconductor with indirect transitions between valence and conduction band in which phonons of wave vectors in the  $[001]$ -direction play a role.

The general theory of crystal dynamics is briefly outlined. Relations between elastic constants and interatomic force constants are established according to the method of long waves. The general formalism of lattice dynamics can be drastically simplified by the employment of the symmetry properties of the crystal lattice. The group-theoretical technique for block-diagonalization of the dynamical matrix according to the irreducible representations of the group of the wave vector and for determining the componental form of the eigenvectors of this matrix, is discussed.

The rigid ion model and the shell model are the most widely used models for dynamical calculations on ionic and covalent crystals. They are briefly described and since both models take into account the electrostatic field forces the Coulomb coupling coefficients have been evaluated for symmetry directions in the two crystal lattices.

The general features of neutron scattering are reviewed and the derivation of expressions for the scattering cross sections has been summarized. For the coherent single-phonon scattering the inelastic structure factor has been formulated and the conditions for reduction of this factor such as to make it periodic in reciprocal space. These inelastic structure factors are of great importance in the design of the phonon measurements because they allow the distinction between the various branches of the dispersion relation.

For the experiments a conventional triple-axis crystal spectrometer has been used; this equipment and the experimental methods are described. A graphical method of focusing was found to be particularly useful and is presented in detail. For the observation of some optic branches the inverse beryllium-filter method was an indispensable auxiliary technique. Its features in the application to single-crystal investiga-

tions are discussed.

For magnesium stannide and zinc blende the group-theoretical technique is applied for wave vectors in the three symmetry directions. In these directions the dispersion relations have been determined and the results are discussed and compared to calculations according to the rigid ion model and the shell model. For the shell model calculations a least squares analysis has been applied. Allowing polarization of the tin atoms in magnesium stannide and of the sulphur atoms in zinc blende a shell model with a small number of parameters could provide reasonably satisfactory descriptions of the experimental dispersion relations. Related physical quantities as e.g. elastic constants and infra-red and Raman frequencies could be predicted in proper agreement with available experimental data. For a correct branch assignment to second-order Raman frequencies the neutron data have been very helpful. For detailed descriptions of the dispersion relations more advanced shell models with a larger number of parameters are required.

According to the calculations the bonding in zinc blende would be mainly covalent with a relatively small polarizability of the sulphur atoms. For magnesium stannide an appreciable fraction of ionicity has been found with a small polarizability of the tin atoms. Finally, the physical significance of the parameters and the applicability of the shell model are discussed.

## SAMENVATTING

Dit proefschrift beschrijft een experimenteel onderzoek van de dispersierelaties in magnesiumstannide en zinkblende met behulp van inelastische strooiing van thermische neutronen. Beide verbindingen hebben een gemengd bindingstype met covalente korte-afstandskrachten en lange-afstandskrachten bestaande uit ionogene en dipool componenten. Magnesiumstannide is een halfgeleider met indirecte overgangen tussen de valentie- en de geleidingsband, waarbij fononen met golfvectors in de richting  $[001]$  een rol spelen.

De algemene theorie van de kristaldynamica wordt in het kort weergegeven. Relaties tussen de elasticiteitsconstanten en de interatomaire krachtconstanten worden afgeleid volgens de methode voor lange golven. De algemene formulering van de kristaldynamica kan aanzienlijk vereenvoudigd worden door gebruik te maken van de symmetrie van het kristalrooster. De groepentheorie wordt gebruikt als hulpmiddel om te komen tot blokdiagonalisatie van de dynamische matrix overeenkomstig de irreducibele voorstellingen van de groep van de golfvector en voor het bepalen van de componentele vormen van de eigenvectors van deze matrix.

Het starre-ionen model en het schillenmodel worden het meest gebruikt voor dynamicaberekeningen in ionogene en covalente kristallen. Zij worden in het kort beschreven en aangezien beide modellen de krachten van het elektrostatische veld in rekening brengen, zijn de koppelingscoëfficiënten voor de Coulomb-wisselwerking berekend voor de richtingen van symmetrie in de twee kristalroosters.

De algemene aspecten van de strooiing van neutronen worden besproken en de afleiding van uitdrukkingen voor de werkzame doorsneden voor strooiing summier weergegeven. Voor de coherente één-fononstrooiing is de inelastische structuurfactor geformuleerd alsmede de voorwaarden voor reductie van deze structuurfactor om deze periodiek in het reciproke rooster te maken. De inelastische structurfactoren zijn van groot belang bij het ontwerpen van de metingen, aangezien met behulp daarvan de verschillende takken van de dispersierelaties onderscheiden kunnen worden.

Voor de experimenten is een drie-kristalspektrometer van conventioneel ontwerp gebruikt; dit apparaat en de experimentele methoden worden

beschreven. Een grafische methode tot focuseren is zeer nuttig geweest en wordt vrij gedetailleerd geformuleerd. Voor de waarneming van sommige optische takken is de inverse beryllium-filter methode gebleken een onontbeerlijke aanvullende meettechniek te zijn. De toepassing van deze methode voor het onderzoek van éénkristallen wordt besproken.

Voor magnesiumstannide en zinkblende wordt de groepentheorie toegepast voor golfvectoren in de symmetrierichtingen. In deze richtingen zijn de dispersierelaties bepaald en deze experimentele resultaten worden vergeleken met berekeningen op basis van het starre-ionen model en het schillenmodel. Voor het schillenmodel werd een kleinste kwadraten analyse met een beperkt aantal parameters uitgevoerd. Door polarisatie toe te laten van het tinatoom in magnesiumstannide en van het zwavelatoom in zinkblende kon met behulp van het schillenmodel een redelijk bevredigende beschrijving van de experimentele dispersierelaties worden verkregen. Met dit model konden grootheden als elasticiteitsconstanten en infrarood en Raman frequenties ook in behoorlijke overeenstemming met beschikbare gegevens worden berekend. Voor een juiste interpretatie van tweede-orde Raman frequenties zijn de neutrongegevens van veel belang gebleken. Voor een gedetailleerde beschrijving van de dispersierelaties zal een meer geavanceerd schillenmodel met een groter aantal parameters gebruikt moeten worden.

Volgens de resultaten van de berekeningen is de binding in zinkblende voornamelijk covalent met een betrekkelijk geringe polariseerbaarheid van de zwavelatomen. Voor magnesiumstannide daarentegen werd een aanzienlijke fractie ionogeen karakter van de binding gevonden eveneens met een geringe polariseerbaarheid van de tinatomen. Tenslotte worden de fysische betekenis van de parameters en de toepasbaarheid van het schillenmodel besproken.



